Received: 12 October 2020 | Revised: 8 April 2021 | Accepted: 9 April 2021

DOI: 10.1002/nme.6699

RESEARCH ARTICLE

WILEY

Shape-free arbitrary polygonal hybrid stress/displacement-function flat shell element for linear and geometrically nonlinear analyses

Cheng-jin Wu[1] | **Song Cen**[1,2,3] | **Ru-xia Ma**[1] | **Chen-feng Li**[4,5]

[1]Department of Engineering Mechanics, School of Aerospace Engineering, Tsinghua University, Beijing, China

[2]School of Mechanics and Engineering, Liaoning Technical University, Fuxin, China

[3]AML, School of Aerospace Engineering, Tsinghua University, Beijing, China

[4]Energy Safety Research Institute, College of Engineering, Swansea University, Swansea, UK

[5]Zienkiewicz Centre for Computational Engineering, College of Engineering, Swansea University, Swansea, UK

Correspondence
Song Cen, Department of Engineering Mechanics, School of Aerospace Engineering, Tsinghua University, Beijing 100084, China.
Email: censong@tsinghua.edu.cn

Funding information
National Natural Science Foundation of China, Grant/Award Number: 11872229

Abstract

A high-performance shape-free arbitrary polygonal hybrid stress/displacement-function flat shell finite element method is proposed for linear and geometrically nonlinear analyses of shells. First, an arbitrary polygonal Mindlin–Reissner plate element and an arbitrary polygonal membrane element with drilling degrees of freedom are constructed based on hybrid displacement-function and hybrid stress-function methods, respectively. Both elements have only two corner nodes along each edge. Second, by assembling the plate and the membrane elements, an arbitrary polygonal flat shell element is constructed. Third, based on the corotational method, a proper best-fit corotated frame for geometrically nonlinear polygonal elements is designed. By updating the analytical trial functions of shell element in each increment step, the original linear flat shell element is generalized to a geometrically nonlinear model. Numerical examples show that the new element possesses excellent performance for both linear and geometrically nonlinear analyses, and possesses outstanding flexibility in dealing with complex loading distributions and mesh shapes.

KEYWORDS

arbitrary polygonal element, finite element method, flat shell element, geometrically nonlinear, hybrid stress-function/displacement-function method

1 | INTRODUCTION

The finite element method (FEM) is usually treated as an efficient tool for analyses of shell/plate structures. At present, most shell elements can be classified into the following categories: the flat shell elements constructed by combining plate and membrane elements; the degenerated shell elements derived from 3D solid theory by introducing shell assumptions; the solid shell elements based on 3D solid theory with appropriate simplification; the curve shell elements based on different shell theories; and so forth. Actually, it is difficult to identify which type is the best choice. But the flat shell element is commonly recognized as the simplest one due to its convenience on geometric modeling, element construction and boundary condition (BC) handling.[1,2] Meanwhile, their performances mainly depend on the plate and membrane elements that make up the flat shell elements.

During past decades, numerous flat shell elements with triangular and quadrilateral shapes have been developed and successfully applied in engineering analysis and design. However, in practical applications, the conventional triangular

or quadrilateral element shapes may not always be convenient and economic for all situations, especially for discretely or irregularly distributed loading or materials with complex geometry cases, as shown in Figure 1. When meshing structures in these special cases, polygonal elements will show more flexibility, and be more effective in mesh generation, transition, modification and refinement.[4]

The method of constructing polygonal plane elements appeared in 1971, when Wachspress proposed his famous polygonal element shape functions based on the perspective geometry method.[5] Around 2000, some improved methods for polygonal elements were also developed from Wachspress shape functions.[6-9] In recent 30 years, more attentions were paid to developing new polygonal element methods, such as the Voronoi cell finite element method,[10,11] the hybrid polygonal element method,[12] the conforming polygonal FEM,[13,14] the *n*-sided polygonal smoothed finite element method,[15,16] the scaled boundary finite element method,[17] the base force element method,[18] and so forth. But almost all above methods only focused on the two-dimensional (2D) plane problems. Since 2017, several polygonal shell/plate elements have been successfully developed. Nguyen-Xuan[4] proposed a polygonal FEM for analysis of Mindlin–Reissner plate, in which a kind of barycentric shape functions were employed. And the element method was developed for static and dynamic analyses of plates and shells by a new arbitrary polytope formulation named polytopal composite finite element.[19] Videla et al.[20] proposed another locking-free polygonal plate element based on Mindlin–Reissner plate theory and assumed shear strain fields. Katili et al.[21] also constructed a polygonal thin/thick plate element by smoothed finite element method. Ho-Nguyen-Tan and Kim[22] developed a polygonal degenerated shell elements by assuming covariant shear strain field and employing the mixed interpolation technique. Aurojyoti et al.[23] proposed an *n*-sided polygonal finite element for nonlocal nonlinear analysis of plates and laminates based on Reddy's third-order shear deformation theory. Similar to the conventional elements, in order to obtain satisfactory results, relatively refined meshes are still needed for these new polygonal models.

On the other hand, the hybrid-Trefftz element methods is also an effective way for developing various FEMs in many fields, such as the T-Trefftz Voronoi cell finite elements,[24,25] and the hybrid-Trefftz FEMs for poroelastic media,[26] plate bending,[27,28] elastoplassticity,[29] Helmholtz problem,[30,31] heat conduction,[32] and so forth. In the past 10 years, Cen et al. proposed two hybrid-Trefftz FEMs, a hybrid stress-function (HSF)[33-39] and a hybrid displacement-function (HDF)[33,40-45] element methods for developing 2D plane and Mindlin–Reissner plate elements, respectively. The constructions of these element are simply extended from the original hybrid stress element proposed by Pian.[46] Instead of directly assuming equilibrium stress or resultant fields, the trial functions of the element stress or resultant fields are derived from the analytical solutions of stress or displacement functions (analytical trial function method), respectively, which means the resulting stresses or resultants and other fields will satisfy all the homogeneous control equations. Then, by adopting proper element boundary displacement modes and applying the principle of minimum complementary energy, the

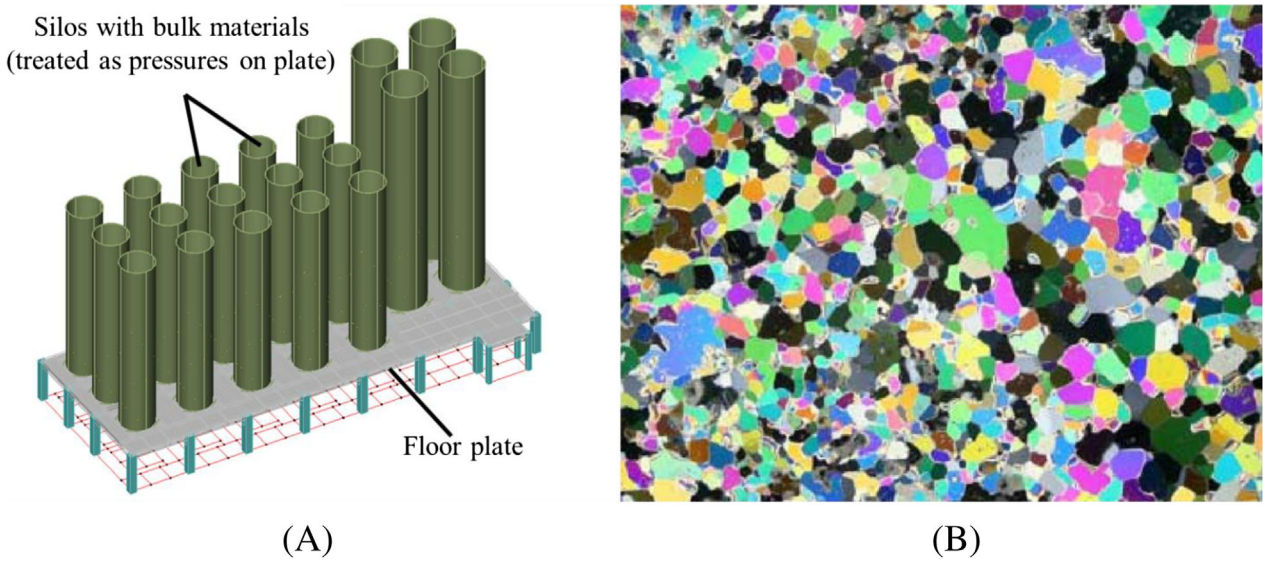

FIGURE 1 Examples for discretely distributed loading and materials: (A) Industrial silos on floor plate; (B) crystal materials[3]

element stiffness matrix related to the conventional nodal displacement degrees of freedoms (DOFs) can be obtained. Following above procedure, Cen et al. proposed several 8- and 12-node plane quadrilateral HSF elements,[34] a 4-node plane quadrilateral HSF element with drilling degree of freedom,[35] and a plane HSF element for anisotropic material analyses by employ the anisotropic analytical solutions[36]; Cen et al.,[40] Shang et al.,[41] Bao et al.,[42] and Huang et al.[43] developed several triangular and quadrilateral HDF elements for Mindlin–Reissner plate. Shang et al.[44] developed a 4-node quadrilateral flat shell element by combining 4-node HSF plane and HDF plate elements. These HSF and HDF elements can provide much better results using extremely coarse meshes, or even severely distorted meshes. Since the structures of the HSF and HDF element formulations are similar to the conventional hybrid stress element, the explicit shape functions for element displacement fields are not needed, which means the main obstacle for displacement-based polygonal element construction does not exist. Therefore, the HSF and the HDF element methods possesses an obvious advantage on developing polygonal elements. Zhou et al.[37] and Cen et al.[38] successfully developed two arbitrary polygonal crack tip HSF elements for plane fracture analyses. Zhou et al.[39] proposed an arbitrary polygonal plane HSF element with mid-side nodes. Wu et al.[45] proposed several arbitrary polygonal HDF Mindlin–Reissner plate elements with mid-side nodes. However, because the analytical solutions of linear elasticity are employed in HSF and HDF element formulations, and there are no assumed element displacement fields in the whole construction procedure, whether these methods can be generalized to geometrically nonlinear applications becomes a serious problem.

The total Lagrangian (TL) and the updated Lagrangian (UL) formulations are the two common schemes for finite element geometrically nonlinear analyses, in which necessary treatments on element displacement fields must be performed during their procedures. Obviously, for those elements without explicit assumed element displacement fields, such as the conventional hybrid stress element, the hybrid-Trefftz element, the HSF elements, the HDF elements, and so forth, both TL and UL formulations cannot properly work. An alternative scheme is the corotational (CR) formulation initially proposed by Wempner[47] and Belytschko et al.[48] in early time. Then, Rankin and Brogan[49] developed a concept of element independent corotational (EICR) formulation. Nouromid and Rankin[50,51] improved the EICR method by introducing a rotation projector matrix. Crisfield and Moita[52] presented a unified CR analysis procedure of various finite elements. Fellippa and Haugen[53] summarized the EICR formulations and developed a unified theoretical framework for CR formulation with small strain, named by the consistent symmetrizable equilibrated CR formulation. In the CR method, the element's large-rotation, small-strain problem is decomposed into element rigid body translation and local linear elastic deformation. By defining an appropriate local frame, the geometrically nonlinear problem can be linearized, so that any linear finite element can be generalized to the geometrically nonlinear applications. That is to say, the development of the CR method offers a new way for generalizing linear elements to geometrically nonlinear analyses. Based on the CR formulations, some geometrically nonlinear shell elements have been successfully developed.[54-60] Here, it should be noted that, according to the difference choices of reference configurations, initial or current, the CR method possesses its own TL and UL formulations. For most elements expressed in terms of local coordinates, these two formulations under the CR frame are equivalent. However, as described above, the trial functions of the HSF and HDF elements are based on the linear analytical solutions related to global coordinates. Therefore, for the HSF and the HDF elements, only UL formulation can be adopted under the CR frame.

The purpose of this article is to develop an arbitrary polygonal hybrid stress/displacement-function (HSDF) flat shell element for linear and geometrically nonlinear analyses. First, a polygonal HDF Mindlin–Reissner plate element and a polygonal HSF membrane element with drilling DOFs are constructed, both of which have only two corner nodes on each element edge. Through theoretical analysis and numerical examinations, a best-fit analytical trial function selection scheme is proposed for both elements. Second, an arbitrary polygonal flat shell element HSDF-PSH is developed by combining above new plate and membrane elements. The shape of new shell element are flexible, with arbitrary number of edges and convex or concave shapes. As a result, it is suitable for meshing many structures with complex geometry and discretely distributed loads. Third, by utilizing the CR method with a best-fit corotated frame selection scheme, and updating analytical trial functions in every incremental step, the linear polygonal flat shell element HSDF-PSH is generalized to a geometrically nonlinear model. For both linear and geometrically nonlinear numerical examples, the new element exhibits excellent convergence, accuracy, and flexibility. Good results can be obtained for extremely coarse and distorted meshes, complex geometries, or discretely distributed loads. This is the first HSF or HDF element model for the geometrically nonlinear analyses. It is also demonstrated that the proposed model are beneficial supplements for shell element library.

2 | PLATE BENDING AND MEMBRANE PARTS OF THE NEW ARBITRARY POLYGONAL FLAT SHELL ELEMENT

In order to construct a new arbitrary polygonal flat shell element HSDF-PSH, a corresponding plate element and a membrane element with drilling degree of freedom should be formulated firstly.

2.1 | The plate bending part of the new flat shell element HSDF-PSH

In this section, a new arbitrary polygonal Mindlin–Riessner plate element is developed by the HDF method.

The typical model of an arbitrary polygonal Mindlin–Reissner plate element is shown in Figure 2(A). The element has n edges and two corner nodes along each edge, that is, one element contains n nodes in total. Figure 2(B) shows the positive directions of the displacements (w, ψ_x, ψ_y) and the stress resultants (M_x, M_y, M_{xy}, T_x, T_y) for the Mindlin–Reissner plate model. Thus, the element nodal displacement vector can be written as:

$$\mathbf{q}_{\mathrm{b}}^{e} = [w_1 \ \ \psi_{x1} \ \ \psi_{y1} \ \ w_2 \ \ \psi_{x2} \ \ \psi_{y2} \ \ \cdots \ \ \cdots \ \ \cdots \ \ w_n \ \ \psi_{xn} \ \ \psi_{yn}]^{\mathrm{T}}. \tag{1}$$

For Mindlin–Reissner plates, the analytical solutions of deflection w, rotations ψ_x and ψ_y can be derived from two displacement functions F and f[61] determined by

$$D\nabla^2\nabla^2 F = q, \tag{2}$$

$$\frac{1}{2}(1-\mu)D\nabla^2 f - Cf = 0, \tag{3}$$

where F affects the whole field, while f represents the edge effects and only works within a small region near particular boundary; q is the uniformly distributed load; μ is Poisson's ratio; D and C are the bending and shear stiffness, respectively, and

$$D = \frac{Eh^3}{12(1-\mu^2)}, C = \frac{5}{6}Gh, \tag{4}$$

in which E is the Young's modulus; $G = E/[2(1+\mu)]$, the shear modulus; h, the plate thickness. In general situations without edge effects, the displacement function f can be ignored, thus, the displacement vector $\mathbf{u}_{\mathrm{b}}$ can be expressed by displacement function F as follows[61].

$$\mathbf{u}_{\mathrm{b}} = \begin{Bmatrix} w \\ \psi_x \\ \psi_y \end{Bmatrix} = \begin{Bmatrix} F - \frac{D}{C}\nabla^2 F \\ \frac{\partial F}{\partial x} \\ \frac{\partial F}{\partial y} \end{Bmatrix}. \tag{5}$$

Then, according to the geometry equation and the constitutive equation, the resultant vector $\mathbf{R}_{\mathrm{b}}$ can be written as

$$\mathbf{R}_{\mathrm{b}} = \begin{Bmatrix} M_x \\ M_y \\ M_{xy} \\ T_x \\ T_y \end{Bmatrix} = \begin{Bmatrix} -D\left(\frac{\partial^2 F}{\partial x^2} + \mu\frac{\partial^2 F}{\partial y^2}\right) \\ -D\left(\frac{\partial^2 F}{\partial y^2} + \mu\frac{\partial^2 F}{\partial x^2}\right) \\ -D(1-\mu)\frac{\partial^2 F}{\partial x \partial y} \\ -D\frac{\partial}{\partial x}(\nabla^2 F) \\ -D\frac{\partial}{\partial y}(\nabla^2 F) \end{Bmatrix}. \tag{6}$$

The displacement function F in Equation (2) can be expressed by the sum of a general solution F^0 and a particular solution F^*:

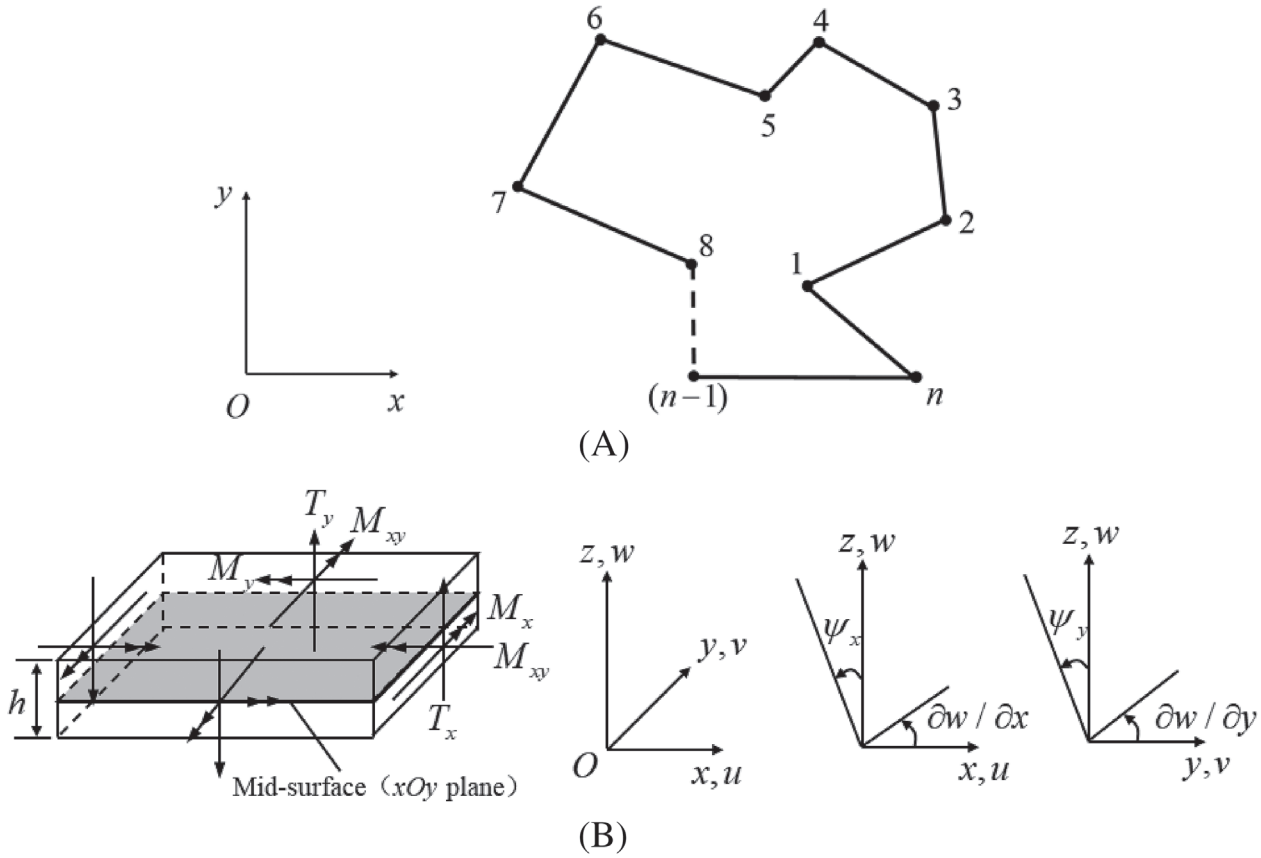

FIGURE 2 An arbitrary polygonal Mindlin–Reissner plate element and the positive directions of the displacements, bending moments, and shear forces

$$F = F^0 + F^*, \tag{7}$$

in which F^0 and F^* satisfy the following two equations:

$$D\nabla^2\nabla^2 F^0 = 0, \tag{8}$$

$$D\nabla^2\nabla^2 F^* = q, \tag{9}$$

respectively.

When formulating the HDF plate elements, the displacement function F is assumed as:

$$F = F^0 + F^* = \sum_{i=1}^{n_F} F_i^0 \beta_{\mathrm{b}i} + F^*, \tag{10}$$

in which $\beta_{\mathrm{b}i}$ $(i = 1, 2, \cdots, n_F)$ are n_F unknown coefficients; $F_i^0 (i = 1, 2, \cdots, n_F)$ are the first n_F fundamental analytical solutions of F^0 satisfying Equation (8), and their expressions in terms of Cartesian coordinates of the first 23 terms and resulting resultants are given in Table 1[40]; F^* is one particular solution satisfying Equation (9). Here,

$$F^* = \frac{q}{48D}(x^4 + y^4) \tag{11}$$

is selected. Thus, the resulting resultant vector $\mathbf{R}_{\mathrm{b}}^*$ related to F^* can be obtained:

TABLE 1 The first 23 fundamental analytical solutions for the general part of the displacement function and resulting resultant forces

	i	1	2	3	4	5	6	7
	$-DF_i^0$	x^2	xy	y^2	x^3	x^2y	xy^2	y^3
$\mathbf{R}_{bi}^0$	M_{xi}^0	2	0	2μ	$6x$	$2y$	$2\mu x$	$6\mu y$
	M_{yi}^0	2μ	0	2	$6\mu x$	$2\mu y$	$2x$	$6y$
	M_{xyi}^0	0	$1-\mu$	0	0	$2(1-\mu)x$	$2(1-\mu)y$	0
	T_{xi}^0	0	0	0	6	0	2	0
	T_{yi}^0	0	0	0	0	2	0	6

	i	8	9	10
	$-DF_i^0$	x^3y	xy^3	x^4-y^4
$\mathbf{R}_{bi}^0$	M_{xi}^0	$6xy$	$6\mu xy$	$12(x^2-\mu y^2)$
	M_{yi}^0	$6\mu xy$	$6xy$	$-12(y^2-\mu x^2)$
	M_{xyi}^0	$3(1-\mu)x^2$	$3(1-\mu)y^2$	0
	T_{xi}^0	$6y$	$6y$	$24x$
	T_{yi}^0	$6x$	$6x$	$-24y$

	i	11	12	13
	$-DF_i^0$	$6x^2y^2-x^4-y^4$	$x^3y^2-xy^4$	$5x^3y^2-x^5$
$\mathbf{R}_{bi}^0$	M_{xi}^0	$12(1-\mu)(y^2-x^2)$	$6xy^2+\mu(2x^3-12xy^2)$	$10\mu x^3-20x^3+30xy^2$
	M_{yi}^0	$12(1-\mu)(x^2-y^2)$	$6\mu xy^2+2x^3-12xy^2$	$10x^3+\mu(-20x^3+30xy^2)$
	M_{xyi}^0	$24(1-\mu)xy$	$(1-\mu)(6x^2y-4y^3)$	$30(1-\mu)x^2y$
	T_{xi}^0	0	$6(x^2-y^2)$	$-30x^2+30y^2$
	T_{yi}^0	0	$-12xy$	$60xy$

	i	14	15
	$-DF_i^0$	$x^2y^3-x^4y$	$5x^2y^3-y^5$
$\mathbf{R}_{bi}^0$	M_{xi}^0	$6\mu x^2y+2y^3-12x^2y$	$10y^3+\mu(-20y^3+30x^2y)$
	M_{yi}^0	$6x^2y+\mu(2y^3-12x^2y)$	$10\mu y^3-20y^3+30x^2y$
	M_{xyi}^0	$(1-\mu)(6xy^2-4x^3)$	$30(1-\mu)xy^2$
	T_{xi}^0	$-12xy$	$60xy$
	T_{yi}^0	$6(-x^2+y^2)$	$30x^2-30y^2$

	i	16	17
	$-DF_i^0$	x^5y-xy^5	$10x^3y^3-3x^5y-3xy^5$
$\mathbf{R}_{bi}^0$	M_{xi}^0	$-20\mu xy^3+20x^3y$	$60(1-\mu)(xy^3-x^3y)$
	M_{yi}^0	$-20xy^3+20\mu x^3y$	$60(1-\mu)(x^3y-xy^3)$
	M_{xyi}^0	$5(1-\mu)(x^4-y^4)$	$-15(1-\mu)(x^4-6x^2y^2+y^4)$
	T_{xi}^0	$60x^2y-20y^3$	0
	T_{yi}^0	$20x^3-60xy^2$	0

	i	18	19
	$-DF_i^0$	$x^6-10x^4y^2+5x^2y^4$	$y^6-10x^2y^4+5x^4y^2$
$\mathbf{R}_{bi}^0$	M_{xi}^0	$30x^4-120x^2y^2+10y^4+\mu(-20x^4+60x^2y^2)$	$-20y^4+60x^2y^2+\mu(30y^4-120x^2y^2+10x^4)$
	M_{yi}^0	$-20x^4+60x^2y^2+\mu(30x^4-120x^2y^2+10y^4)$	$30y^4-120x^2y^2+10x^4+\mu(-20y^4+60x^2y^2)$
	M_{xyi}^0	$40(1-\mu)(-2x^3y+xy^3)$	$40(1-\mu)(-2xy^3+x^3y)$
	T_{xi}^0	$40x^3-120xy^2$	$40x^3-120xy^2$
	T_{yi}^0	$40y^3-120x^2y$	$40y^3-120x^2y$

(Continues)

TABLE 1 (Continued)

	i	20	21
	$-DF_i^0$	$21x^5y^2-2x^7-7xy^6$	$35x^4y^3-y^7-14x^6y$
$\mathbf{R}_{\mathrm{b}i}^0$	M_{xi}^0	$42(-2x^5+10x^3y^2)+42\mu(x^5-5xy^4)$	$420(-x^4y+x^2y^3)+42\mu(5x^4y-y^5)$
	M_{yi}^0	$42(x^5-5xy^4)+42\mu(-2x^5+10x^3y^2)$	$42(5x^4y-y^5)+420\mu(-x^4y+x^2y^3)$
	M_{xyi}^0	$42(1-\mu)(5x^4y-y^5)$	$84(1-\mu)(5x^3y^2-x^5)$
	T_{xi}^0	$-210(x^4-6x^2y^2+y^4)$	$-840(x^3y-xy^3)$
	T_{yi}^0	$840(x^3y-xy^3)$	$-210(x^4-6x^2y^2+y^4)$
	i	22	23
	$-DF_i^0$	$35x^3y^4-x^7-14xy^6$	$21x^2y^5-2y^7-7x^6y$
$\mathbf{R}_{\mathrm{b}i}^0$	M_{xi}^0	$42(5xy^4-x^5)+420\mu(-xy^4+x^3y^2)$	$42(y^5-5x^4y)+42\mu(-2y^5+10x^2y^3)$
	M_{yi}^0	$420(-xy^4+x^3y^2)+42\mu(5xy^4-x^5)$	$42(-2y^5+10x^2y^3)+42\mu(y^5-5x^4y)$
	M_{xyi}^0	$84(1-\mu)(5x^2y^3-y^5)$	$42(1-\mu)(5xy^4-x^5)$
	T_{xi}^0	$-210(x^4-6x^2y^2+y^4)$	$-840(x^3y-xy^3)$
	T_{yi}^0	$840(x^3y-xy^3)$	$-210(x^4-6x^2y^2+y^4)$

$$\mathbf{R}_{\mathrm{b}}^*=\begin{Bmatrix}M_x^*\\M_y^*\\M_{xy}^*\\T_x^*\\T_y^*\end{Bmatrix}=\begin{Bmatrix}-\frac{q}{4}(x^2+\mu y^2)\\-\frac{q}{4}(\mu x^2+y^2)\\0\\-\frac{q}{2}x\\-\frac{q}{2}y\end{Bmatrix}. \tag{12}$$

Substitution of Equation (10) into Equation (6) yields the final resultant vector:

$$\mathbf{R}_{\mathrm{b}}=\begin{Bmatrix}M_x\\M_y\\M_{xy}\\T_x\\T_y\end{Bmatrix}=\sum_{i=1}^{n_F}\begin{Bmatrix}M_{xi}^0\\M_{yi}^0\\M_{xyi}^0\\T_{xi}^0\\T_{yi}^0\end{Bmatrix}\beta_i+\begin{Bmatrix}M_{xi}^*\\M_{yi}^*\\M_{xyi}^*\\T_{xi}^*\\T_{yi}^*\end{Bmatrix}=\sum_{i=1}^{n_F}\mathbf{R}_{\mathrm{b}i}^0\beta_{\mathrm{b}i}+\mathbf{R}_{\mathrm{b}}^*=\mathbf{S}_{\mathrm{b}}\boldsymbol{\beta}_{\mathrm{b}}+\mathbf{R}_{\mathrm{b}}^*, \tag{13}$$

in which $\mathbf{R}_{\mathrm{b}i}^0(i=1,2,\cdots,n_F)$ are given in Table 1, and

$$\mathbf{S}_{\mathrm{b}}=\begin{bmatrix}\mathbf{R}_{\mathrm{b}1}^0 & \mathbf{R}_{\mathrm{b}2}^0 & \cdots & \mathbf{R}_{\mathrm{b}n_F}^0\end{bmatrix}, \tag{14}$$

$$\boldsymbol{\beta}_{\mathrm{b}}=\begin{bmatrix}\beta_{\mathrm{b}1} & \beta_{\mathrm{b}2} & \cdots & \beta_{\mathrm{b}n_F}\end{bmatrix}. \tag{15}$$

For a Mindlin–Reissner plate element, the modified element complementary energy functional can be written as

$$\Pi_{\mathrm{C}}^e=\frac{1}{2}\iint_{A^e}\mathbf{R}_{\mathrm{b}}^{\mathrm{T}}\mathbf{C}_{\mathrm{b}}\mathbf{R}_{\mathrm{b}}\mathrm{d}A+\int_{S^e}\overline{\mathbf{R}}_{\mathrm{b}}^{\mathrm{T}}\overline{\mathbf{d}}_{\mathrm{b}}\mathrm{d}s, \tag{16}$$

where A^e and S^e represent element area and element boundary, respectively; $\mathbf{C}_{\mathrm{b}}$ is the elasticity matrix of compliance:

$$\mathbf{C}_{\mathrm{b}} = \begin{bmatrix} \frac{1}{D(1-\mu^2)} & \frac{-\mu}{D(1-\mu^2)} & 0 & 0 & 0 \\ \frac{-\mu}{D(1-\mu^2)} & \frac{1}{D(1-\mu^2)} & 0 & 0 & 0 \\ 0 & 0 & \frac{2}{D(1-\mu)} & 0 & 0 \\ 0 & 0 & 0 & \frac{1}{C} & 0 \\ 0 & 0 & 0 & 0 & \frac{1}{C} \end{bmatrix}; \tag{17}$$

$\overline{\mathbf{R}}_{\mathrm{b}}$ and $\overline{\mathbf{d}}_{\mathrm{b}}$ denote resultant and displacement vectors along the element boundary, respectively:

$$\overline{\mathbf{R}}_{\mathrm{b}} = \begin{Bmatrix} \overline{M}_n \\ \overline{M}_{ns} \\ -\overline{T}_n \end{Bmatrix} = \mathbf{L}_{\mathrm{b}}\mathbf{R}_{\mathrm{b}}, \overline{\mathbf{d}}_{\mathrm{b}} = \begin{Bmatrix} \overline{\psi}_n \\ \overline{\psi}_s \\ \overline{w} \end{Bmatrix} = \overline{\mathbf{N}}_{\mathrm{b}}\mathbf{q}_{\mathrm{b}}^e, \tag{18}$$

in which $\mathbf{L}_{\mathrm{b}}$ is the direction cosine matrix on the element boundary:

$$\mathbf{L}_{\mathrm{b}} = \begin{bmatrix} l^2 & m^2 & 2lm & 0 & 0 \\ -lm & lm & l^2 - m^2 & 0 & 0 \\ 0 & 0 & 0 & -l & -m \end{bmatrix}, \tag{19}$$

and l and m denote direction cosines of the element boundaries' outer normal; $\overline{\mathbf{N}}_{\mathrm{b}}$ is the interpolation matrix of element boundary displacement field, and it can be obtained by the locking-free formulae of Timoshenko's beam theory.

A typical 2-node Timoshenko's beam $i'j'$ is shown in Figure 3. The deflection $\overline{w}_{i'j'}$ and rotation $\overline{\psi}_{si'j'}$ is given by Hu[61]:

$$\begin{aligned} \overline{w}_{i'j'} &= I_{w1}w_{i'} + I_{w2}w_{j'} + I_{w3}\psi_{si'} + I_{w4}\psi_{sj'} \\ &= [1 - s + (1 - 2\delta_{i'j'})Z_3]w_{i'} + [s - (1 - 2\delta_{i'j'})Z_3]w_{j'} \\ &\quad + \frac{L_{i'j'}}{2}[Z_2 + (1 - 2\delta_{i'j'})Z_3]\psi_{si'} - \frac{L_{i'j'}}{2}[Z_2 - (1 - 2\delta_{i'j'})Z_3]\psi_{sj'}, \end{aligned} \tag{20}$$

$$\begin{aligned} \overline{\psi}_{si'j'} &= I_{s1}w_{i'} + I_{s2}w_{j'} + I_{s3}\psi_{si'} + I_{s4}\psi_{sj'} \\ &= -\frac{6}{L_{i'j'}}(1 - 2\delta_{i'j'})Z_2w_{i'} + \frac{6}{L_{i'j'}}(1 - 2\delta_{i'j'})Z_2w_{j'} \\ &\quad + [1 - s - 3(1 - 2\delta_{i'j'})Z_2]\psi_{si'} + [s - 3(1 - 2\delta_{i'j'})Z_2]\psi_{sj'}, \end{aligned} \tag{21}$$

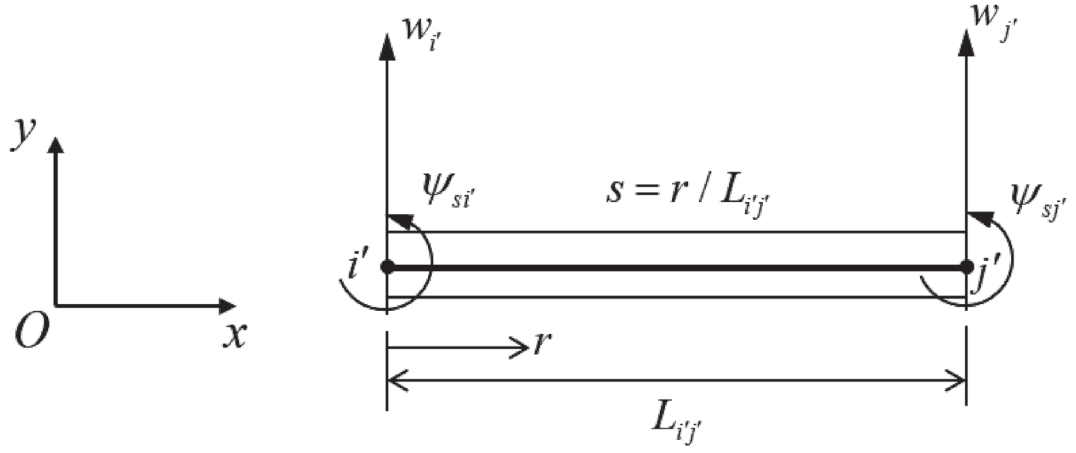

FIGURE 3 2-node locking-free Timoshenko's beam

in which

$$\delta_{i'j'} = \frac{6\lambda_{i'j'}}{1+12\lambda_{i'j'}}, \lambda_{i'j'} = \frac{D}{CL_{i'j'}^2}, Z_2 = s(1-s), Z_3 = s(1-s)(1-2s), \tag{22}$$

where $L_{i'j'}$ denotes the length of beam; s is the local coordinate along the beam; I_{wi} and $I_{si}(i = 1, 2, 3, 4)$ are interpolation functions; $w_{i'}, \psi_{si'}, w_{j'}, \psi_{sj'}$ denote deflections and tangential rotations of corresponding nodes. The normal rotation along the element edge is assumed to be linear:

$$\overline{\psi}_{ni'j'} = I_{n1}\psi_{ni'} + I_{n2}\psi_{nj'} = (1-s)\psi_{ni'} + s\psi_{nj'}, \tag{23}$$

in which $I_{ni}(i = 1, 2)$ are also interpolation functions, and $\psi_{ni'}, \psi_{nj'}$ represent normal rotations of corresponding nodes. For the ith boundary of the element, the end nodes can be denoted by $i' = i, j' = i+1$ (when $i = n$, $j = 1$). Then, the element boundary displacement fields can be obtained:

$$\overline{\mathbf{d}}_{\mathrm{b}}\Big|_{i\mathrm{th}} = \left\{\begin{matrix}\overline{\psi}_n \\ \overline{\psi}_s \\ \overline{w}\end{matrix}\right\}\Bigg|_{i\mathrm{th}} = \mathbf{L}_{\mathrm{b}i'j'}\mathbf{q}_{\mathrm{b}i'j'} = \overline{\mathbf{N}}_{\mathrm{b}}\Big|_{i\mathrm{th}}\mathbf{q}_{\mathrm{b}}^e, \tag{24}$$

where

$$\mathbf{L}_{\mathrm{b}i'j'} = \begin{bmatrix} 0 & -\frac{y_{i'j'}}{L_{i'j'}}I_{n1} & \frac{x_{i'j'}}{L_{i'j'}}I_{n1} & 0 & -\frac{y_{i'j'}}{L_{i'j'}}I_{n2} & \frac{x_{i'j'}}{L_{i'j'}}I_{n2} \\ I_{s1} & -\frac{x_{i'j'}}{L_{i'j'}}I_{s3} & -\frac{y_{i'j'}}{L_{i'j'}}I_{s3} & I_{s2} & -\frac{x_{i'j'}}{L_{i'j'}}I_{s4} & -\frac{y_{i'j'}}{L_{i'j'}}I_{s4} \\ I_{w1} & -\frac{x_{i'j'}}{L_{i'j'}}I_{w3} & -\frac{y_{i'j'}}{L_{i'j'}}I_{w3} & I_{w2} & -\frac{x_{i'j'}}{L_{i'j'}}I_{w4} & -\frac{y_{i'j'}}{L_{i'j'}}I_{w4} \end{bmatrix} = \left[(\widetilde{\mathbf{L}}_{\mathrm{b}i'})_{3\times3} \quad (\widetilde{\mathbf{L}}_{\mathrm{b}j'})_{3\times3}\right], \tag{25}$$

$$\overline{\mathbf{N}}_{\mathrm{b}}\Big|_{i\mathrm{th}} = \underset{\substack{\\ \\ i'}}{\left[\mathbf{0} \quad \cdots \quad \widetilde{\mathbf{L}}_{\mathrm{b}i'}\right.} \underset{\substack{\\ \\ j'}}{\left.\widetilde{\mathbf{L}}_{\mathrm{b}j'}\right.} \quad \cdots \quad \mathbf{0}\Big]_{3\times3n}, \tag{26}$$

$$\mathbf{q}_{\mathrm{b}i'j'} = \left[\mathbf{q}_{\mathrm{b}i'}^{\mathrm{T}} \quad \mathbf{q}_{\mathrm{b}j'}^{\mathrm{T}}\right]^{\mathrm{T}}, \tag{27}$$

$$\mathbf{q}_{\mathrm{b}k'} = \left[w_{k'} \quad \psi_{xk'} \quad \psi_{yk'}\right]^{\mathrm{T}} (k' = i', j'). \tag{28}$$

By substituting element resultant fields Equations (12)–(15) and boundary displacement fields Equations (24)–(26) into Equation (16), and applying the stationary conditions of the complementary energy,[40] the finite element equation can be obtained:

$$\mathbf{K}_{\mathrm{b}}^e\mathbf{q}_{\mathrm{b}}^e = \mathbf{P}_{\mathrm{b}}^e, \tag{29}$$

where $\mathbf{K}_{\mathrm{b}}^e$ is the element stiffness matrix; $\mathbf{P}_q^e$ is the equivalent nodal load vector;

$$\mathbf{K}_{\mathrm{b}}^e = \mathbf{H}_{\mathrm{b}}^{\mathrm{T}}\mathbf{M}_{\mathrm{b}}^{-1}\mathbf{H}_{\mathrm{b}}, \tag{30}$$

$$\mathbf{P}_{\mathrm{b}}^e = \mathbf{V}^{\mathrm{T}} - \mathbf{H}_{\mathrm{b}}^{\mathrm{T}}\mathbf{M}_{\mathrm{b}}^{-1}\mathbf{M}_{\mathrm{b}}^*, \tag{31}$$

in which

$$\mathbf{M}_{\mathrm{b}} = \iint_{A^e} \mathbf{S}_{\mathrm{b}}^{\mathrm{T}}\mathbf{C}_{\mathrm{b}}\mathbf{S}_{\mathrm{b}}\,\mathrm{d}A, \tag{32}$$

$$\mathbf{M}_{\mathrm{b}}^* = \iint_{A^e} \mathbf{S}_{\mathrm{b}}^{\mathrm{T}}\mathbf{C}_{\mathrm{b}}\mathbf{R}_{\mathrm{b}}^*\,\mathrm{d}A, \tag{33}$$

$$\mathbf{H}_{\mathrm{b}} = \int_{S^e} \mathbf{S}_{\mathrm{b}}^{\mathrm{T}}\mathbf{L}_{\mathrm{b}}^{\mathrm{T}}\overline{\mathbf{N}}_{\mathrm{b}}\,\mathrm{d}s, \tag{34}$$

$$\mathbf{V} = \int_{S^e} \mathbf{R}_{\mathrm{b}}^{*\mathrm{T}}\mathbf{L}_{\mathrm{b}}^{\mathrm{T}}\overline{\mathbf{N}}_{\mathrm{b}}\,\mathrm{d}s. \tag{35}$$

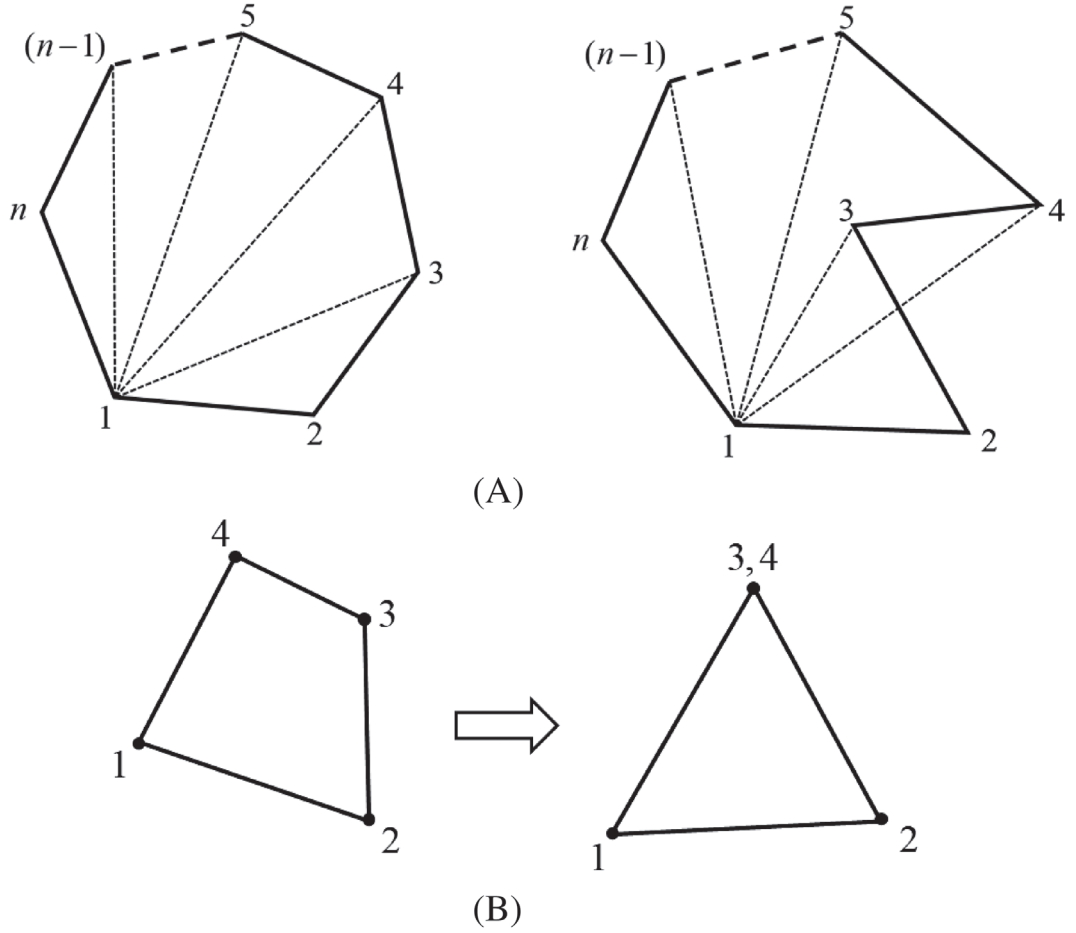

FIGURE 4 Integration scheme for polygonal elements

For the polygonal elements, a simple and effective integration scheme was proposed in Reference 45. As shown in Figure 4(A), a polygonal element (no matter convex or concave) can be divided into $(n-2)$ 3-node subtriangle domains. During the integration calculation, each subtriangle will be treated as a degenerated 4-node quadrilateral isoparametric element in which nodes 3 and 4 coincide with each other, see Figure 4(B). The shape functions of 4-node isoparametric quadrilateral element are given by:

$$N_1 = \frac{1}{4}(1-\xi)(1-\eta) \;\; N_2 = \frac{1}{4}(1+\xi)(1-\eta)$$
$$N_3 = \frac{1}{4}(1+\xi)(1+\eta) \;\; N_4 = \frac{1}{4}(1-\xi)(1+\eta) \tag{36}$$

.Therefore, the Cartesian coordinates (x, y) of an arbitrary point in the subtriangle domain can be expressed by:

$$x = \sum_{i=1}^{4} N_i x_i, \;\; y = \sum_{i=1}^{4} N_i y_i, \tag{37}$$

in which (x_i, y_i) denote the corresponding nodal coordinates. Other procedure are the same as that given in Reference 45.

Thus, an arbitrary polygonal HDF Mindlin–Reissner plate element without mid-node is constructed. And it is the plate bending part of the new flat shell element HSDF-PSH.

2.2 | The membrane part of the new flat shell element HSDF-PSH

A typical model of arbitrary polygonal membrane element with drilling DOF is shown in Figure 5. The element also has n edges and 2 corner nodes along each side, that is, one element contains n nodes in total. Each element node has three

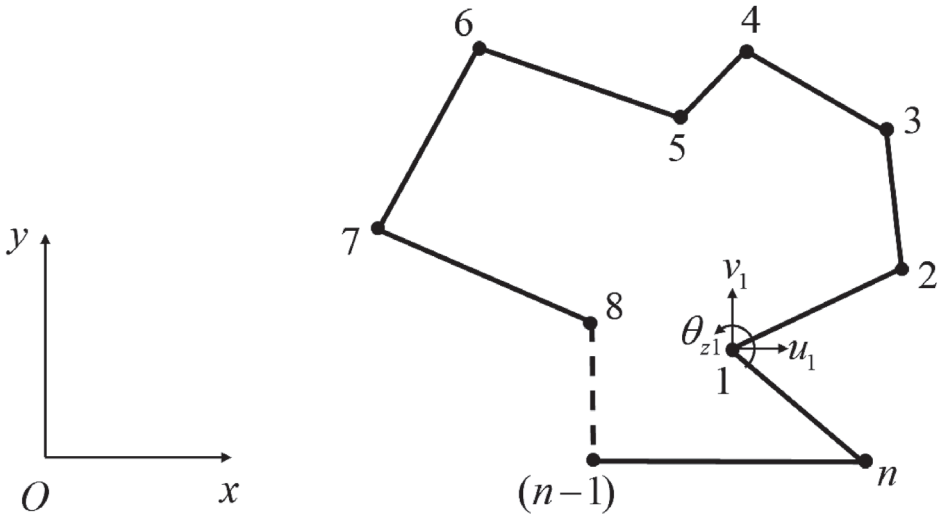

FIGURE 5 An arbitrary polygonal membrane element with drilling degrees of freedom

DOFs: in-plane lateral displacements u_i, v_i ($i = 1, 2, \cdots, n$), and in-plane rotation θ_{zi} ($i = 1, 2, \cdots, n$). It should be noted that the rotation θ_{zi} is the drilling DOFs defined by Allman,[62] rather than physical rotation. Thus, the element nodal displacement vector can be written as:

$$\mathbf{q}_{\mathrm{m}}^{e} = \begin{bmatrix} u_1 & v_1 & \theta_{z1} & u_2 & v_2 & \theta_{z2} & \cdots & \cdots & \cdots & u_n & v_n & \theta_{zn} \end{bmatrix}^{\mathrm{T}}. \tag{38}$$

According to the theory of elasticity, the stress vector $\boldsymbol{\sigma}$ can be derived from the Airy stress function ϕ, which satisfied

$$\nabla^2 \nabla^2 \phi = 0. \tag{39}$$

And the stress vector

$$\boldsymbol{\sigma} = \begin{Bmatrix} \sigma_x \\ \sigma_y \\ \tau_{xy} \end{Bmatrix} = \begin{Bmatrix} \frac{\partial^2 \phi}{\partial y^2} \\ \frac{\partial^2 \phi}{\partial x^2} \\ -\frac{\partial^2 \phi}{\partial x \partial y} \end{Bmatrix} = \mathbf{R}_{\mathrm{m}}(\phi). \tag{40}$$

The first 27 fundamental analytical solutions of the Airy stress function for isotropic problems and the resulting stress solutions are listed in Table 2.[34] By interpolation of these analytical solutions, the stress function and resulting stress vector can be expressed by:

$$\phi = \sum_{i=1}^{n_\phi} \phi_i \beta_i = \boldsymbol{\varphi} \boldsymbol{\beta}_{\mathrm{m}}, \tag{41}$$

$$\mathbf{R}_{\mathrm{m}} = \mathbf{S}_{\mathrm{m}} \boldsymbol{\beta}_{\mathrm{m}}, \tag{42}$$

with

$$\begin{aligned} \boldsymbol{\varphi} &= \begin{bmatrix} \phi_1 & \phi_2 & \phi_3 & \cdots & \cdots & \phi_{n_\phi} \end{bmatrix} \\ \boldsymbol{\beta}_{\mathrm{m}} &= \begin{bmatrix} \beta_{\mathrm{m}1} & \beta_{\mathrm{m}2} & \beta_{\mathrm{m}3} & \cdots & \cdots & \beta_{\mathrm{m}n_\phi} \end{bmatrix}^{\mathrm{T}}, \end{aligned} \tag{43}$$

$$\mathbf{S}_{\mathrm{m}} = \begin{bmatrix} \sigma_{x1} & \sigma_{x2} & \sigma_{x3} & \cdots & \sigma_{xn_\phi} \\ \sigma_{y1} & \sigma_{y2} & \sigma_{y3} & \cdots & \sigma_{yn_\phi} \\ \tau_{xy1} & \tau_{xy2} & \tau_{xy3} & \cdots & \tau_{xyn_\phi} \end{bmatrix}, \tag{44}$$

TABLE 2 The first 27 fundamental analytical solutions for Airy stress function and resulting stresses

i	1	2	3	4	5	6	7	8	9
ϕ_i	x^2	xy	y^2	x^3	x^2y	xy^2	y^3	x^3y	xy^3
σ_{xi}	0	0	2	0	0	$2x$	$6y$	0	$6xy$
σ_{yi}	2	0	0	$6x$	$2y$	0	0	$6xy$	0
τ_{xyi}	0	-1	0	0	$-2x$	$-2y$	0	$-3x^2$	$-3y^2$

i	10	11	12	13	14	15
ϕ_i	$x^4-3x^2y^2$	$y^4-3x^2y^2$	$10x^3y^2-2x^5$	$10x^2y^3-2y^5$	$5x^4y-y^5$	$5xy^4-x^5$
σ_{xi}	$-6x^2$	$12y^2-6x^2$	$20x^3$	$20y(3x^2-2y^2)$	$-20y^3$	$60xy^2$
σ_{yi}	$12x^2-6y^2$	$-6y^2$	$-20x(2x^2-3y^2)$	$20y^3$	$60x^2y$	$-20x^3$
τ_{xyi}	$12xy$	$12xy$	$-60x^2y$	$-60xy^2$	$-20x^3$	$-20y^3$

i	16	17	18	19
ϕ_i	$6x^5y-10x^3y^3$	$6xy^5-10x^3y^3$	$-4x^6+30x^4y^2-2y^6$	$-4y^6+30x^2y^4-2x^6$
σ_{xi}	$-60x^3y$	$120xy^3-60x^3y$	$60x^4-60y^4$	$-120y^4+360x^2y^2$
σ_{yi}	$120x^3y-60xy^3$	$-60xy^3$	$-120x^4+360x^2y^2$	$60y^4-60x^4$
τ_{xyi}	$90x^2y^2-30x^4$	$90x^2y^2-30y^4$	$-240x^3y$	$-240xy^3$

i	20	21	22	23
ϕ_i	$21x^5y^2-2x^7-7xy^6$	$35x^4y^3-y^7-14x^6y$	$35x^3y^4-x^7-14xy^6$	$21x^2y^5-2y^7-7x^6y$
σ_{xi}	$42x^5-210xy^4$	$210x^4y-42y^5$	$420x^3y^2-420xy^4$	$420x^2y^3-84y^5$
σ_{yi}	$420x^3y^2-84x^5$	$420x^2y^3-420x^4y$	$210xy^4-42x^5$	$42y^5-210x^4y$
τ_{xyi}	$-210x^4y+42y^5$	$-420x^3y^2+84x^5$	$-420x^2y^3+84y^5$	$-210xy^4+42x^5$

i	24	25	26	27
ϕ_i	$-3x^8-70x^4y^4+56x^6y^2+y^8$	$x^8-70x^4y^4+56x^2y^6-3y^8$	$-16x^7y+56x^5y^3-8xy^7$	$-8x^7y+56x^3y^5-16xy^7$
σ_{xi}	$-840x^4y^2+112x^6+56y^6$	$-840x^4y^2+1680x^2y^4-168y^6$	$336x^5y-336xy^5$	$1120x^3y^3-672xy^5$
σ_{yi}	$-168x^6-840x^2y^4+1680x^4y^2$	$56x^6-840x^2y^4+112y^6$	$-672x^5y+1120x^3y^3$	$-336x^5y+336xy^5$
τ_{xyi}	$1120x^3y^3-672x^5y$	$1120x^3y^3-672xy^5$	$112x^6-840x^4y^2+56y^6$	$56x^6-840x^2y^4+112y^6$

in which n_ϕ denotes the number of analytical solutions; ϕ_i, σ_{xi}, σ_{yi}, τ_{xyi} $(i = 1, 2, \cdots, n_\phi)$ are the analytical solutions of Airy stress function and resulting stress solutions, and can be found in Table 2; β_i $(i = 1, 2, \cdots, n_\phi)$ are unknown coefficients.

The modified element complementary energy functional can be written as

$$\Pi_C = \frac{1}{2}\iint_{A^e} \mathbf{R}_{\mathrm{m}}^{\mathrm{T}}\mathbf{C}_{\mathrm{m}}\mathbf{R}_{\mathrm{m}}t\mathrm{d}A - \int_{S^e} \mathbf{R}_{\mathrm{m}}^{\mathrm{T}}\mathbf{L}_{\mathrm{m}}^{\mathrm{T}}\overline{\mathbf{d}}_{\mathrm{m}}t\mathrm{d}S, \tag{45}$$

where

$$\mathbf{L}_{\mathrm{m}} = \begin{bmatrix} l & 0 & m \\ 0 & m & l \end{bmatrix}, \tag{46}$$

l and m are direction cosines of the element boundaries' outer normal; and $\mathbf{C}_{\mathrm{m}}$ is the elasticity matrix of compliance

$$\mathbf{C}_{\mathrm{m}} = \frac{1}{E'}\begin{bmatrix} 1 & -\mu' & 0 \\ -\mu' & 1 & 0 \\ 0 & 0 & 2(1+\mu') \end{bmatrix}, \tag{47}$$

let E be the Young's modulus, and μ be the Poisson's ratio. Then, $E' = E$ and $\mu' = \mu$ for plane stress problem, whereas $E' = E/(1-\mu^2)$ and $\mu' = \mu/(1-\mu)$ for plane strain problem; for the membrane part of the flat shell element, only plane stress state is considered; $\overline{\mathbf{d}}_{\mathrm{m}}$ represents the displacement fields along the element edges, and with the Allman's definitions, the displacement fields along the ith element boundary can be expressed as:

$$\overline{\mathbf{d}}_{\mathrm{m}}\Big|_{i\mathrm{th}} = \left\{\begin{matrix}\overline{u}\\ \overline{v}\end{matrix}\right\}\Bigg|_{i\mathrm{th}} = \mathbf{L}_{\mathrm{m}i'j'}\mathbf{q}_{\mathrm{m}i'j'} = \overline{\mathbf{N}}_{\mathrm{m}}\Big|_{i\mathrm{th}}\mathbf{q}^e_{\mathrm{m}}, \tag{48}$$

with

$$\mathbf{L}_{\mathrm{m}i'j'} = \begin{bmatrix}\overline{N}_1 & 0 & \overline{N}_{u\theta 1} & \overline{N}_2 & 0 & \overline{N}_{u\theta 2}\\ 0 & \overline{N}_1 & \overline{N}_{v\theta 1} & 0 & \overline{N}_2 & \overline{N}_{v\theta 2}\end{bmatrix} = \left[(\widetilde{\mathbf{L}}_{\mathrm{m}i'})_{2\times 3} \quad (\widetilde{\mathbf{L}}_{\mathrm{m}j'})_{2\times 3}\right], \tag{49}$$

$$\overline{N}_1 = \frac{1}{2}(1-\xi)\ \ \overline{N}_2 = \frac{1}{2}(1+\xi)$$

$$\overline{N}_{u\theta 1} = \frac{y_{i'} - y_{j'}}{8}(1-\xi^2)\ \ \overline{N}_{v\theta 1} = \frac{x_{j'} - x_{i'}}{8}(1-\xi^2)$$

$$\overline{N}_{u\theta 2} = -\overline{N}_{u\theta 1}\ \ \overline{N}_{v\theta 2} = -\overline{N}_{v\theta 1} \tag{50}$$

,

$$\overline{\mathbf{N}}_{\mathrm{m}}\Big|_{i\mathrm{th}} = \underset{\substack{\\ |\\ i'}}{\Big[\mathbf{0} \quad \cdots \quad \widetilde{\mathbf{L}}_{\mathrm{m}i'}}\quad \underset{\substack{\\ |\\ j'}}{\widetilde{\mathbf{L}}_{\mathrm{m}j'}} \quad \cdots \quad \mathbf{0}\Big]_{2\times 3n}, \tag{51}$$

$$\mathbf{q}_{\mathrm{m}i'j'} = \left[\mathbf{q}^{\mathrm{T}}_{\mathrm{m}i'} \quad \mathbf{q}^{\mathrm{T}}_{\mathrm{m}j'}\right]^{\mathrm{T}}, \tag{52}$$

$$\mathbf{q}_{\mathrm{m}k'} = \left[u_{k'} \quad v_{k'} \quad \theta_{zk'}\right]^{\mathrm{T}} (k' = i', j'), \tag{53}$$

in which i' and j' denote the nodal number along the ith boundary, that is, $i' = i$ and $j' = i+1$ ($j' = 1$, when $i = n$); $(x_{i'}, y_{i'}), (x_{j'}, y_{j'})$ are Cartesian coordinates of these two nodes; ξ is the local isoparametric coordinate along the edge.

By substituting element resultant fields Equations (42)–(44) and boundary displacement fields Equations (48)–(51) into Equation (45), and applying the stationary conditions of the complementary energy, the finite element equation can be obtained[34]:

$$\mathbf{K}^e_{\mathrm{m}}\mathbf{q}^e_{\mathrm{m}} = \mathbf{P}^e_{\mathrm{m}}, \tag{54}$$

where the element stiffness matrix

$$\mathbf{K}^e_{\mathrm{m}} = \mathbf{H}^{\mathrm{T}}_{\mathrm{m}}\mathbf{M}^{-1}_{\mathrm{m}}\mathbf{H}_{\mathrm{m}}, \tag{55}$$

with

$$\mathbf{M}_{\mathrm{m}} = \iint_{A^e} \mathbf{S}^{\mathrm{T}}_{\mathrm{m}}\mathbf{C}_{\mathrm{m}}\mathbf{S}_{\mathrm{m}} t \mathrm{d}A, \tag{56}$$

$$\mathbf{H}_{\mathrm{m}} = \int_{S^e} \mathbf{S}^{\mathrm{T}}_{\mathrm{m}}\mathbf{L}^{\mathrm{T}}_{\mathrm{m}}\overline{\mathbf{N}}_{\mathrm{m}} \mathrm{d}s, \tag{57}$$

and the expression of equivalent nodal load vector $\mathbf{P}^e_{\mathrm{m}}$ caused by concentrated load or boundary distributed load is same as conventional FEM method. For example, for element boundary with distributed load $\mathbf{p}^e = \left[p_x \quad p_y\right]^{\mathrm{T}}$, $\mathbf{P}^e_{\mathrm{m}} = \int_{S^e}\overline{\mathbf{N}}^{\mathrm{T}}_{\mathrm{m}}\mathbf{p}^e \mathrm{d}s$.

By utilizing the same integration scheme introduced in Section 2.1, the integration for arbitrary polygonal HSF element can be obtained. Thus, an arbitrary polygonal HSF membrane element with drilling DOFs is constructed. And it is the membrane part of the new flat shell element HSDF-PSH.

3 | NEW ARBITRARY POLYGONAL HSDF FLAT SHELL ELEMENT

3.1 | The selection scheme of the analytical trial functions for arbitrary polygonal plate and membrane elements

A common feature of HSF and HDF element methods is that both formulations take advantage of the analytical trial functions derived from the homogeneous analytical solutions of stress or displacement function. For various elements with different nodes or edges, different numbers of the analytical trial functions should be adopted to achieve the best performance in both precision and efficiency. Actually, through theoretical analysis and numerical test, it can be found that the best choice of analytical trial functions is definite for an element with corresponding edges.

Similar to the conventional finite elements, the HSF and HDF element stiffness matrices also have inherent zero energy modes. For the Mindlin–Reissner plate element, there are three zero energy modes, including one rigid body translation and two rigid rotations. For the membrane element with drilling DOFs, beside the three usual zero energy modes corresponding to two rigid body translations and one rigid rotation, an additional zero energy mode exists due to the Allman's definitions of drilling DOFs.[62] From Equations (48) to (53), it can be found, if all the element nodal rotations are equal, the magnitude of rotations cannot influence the boundary displacement fields. That is to say, in this situation, the nodal rotations will not affect the element deformation. During calculation, this additional zero energy modes can be simply avoided by appropriate constraint or mesh refinement. Except these acceptable modes, other spurious zero energy modes must be avoided.

For both HSF and HDF elements, the analytical trial functions (Tables 1 and 2) should be selected in turn from the lowest-order to higher-order, and the resulting assumed stress or resultant fields should possess completeness in Cartesian coordinates. The first three terms in Tables 1 and 2 are corresponding to the constant resultant or stress fields, while there are four terms for each other higher-order resultant or stress fields. Thus, the number of the analytical trial functions should be $3+4n_c$, in which n_c is the completeness order of the resultant or stress fields in Cartesian coordinates.

In order to inspect the number of element zero energy modes influenced by different numbers of the selected analytical trial functions, the following numerical examination procedure is implemented: (i) construct different HSF and HDF element stiffness matrices by selecting different numbers of analytical trial functions and element edges; (ii) find the number of zero eigenvalues of these element stiffness matrices that represents the total number of zero energy modes; (iii) compare the results with the element's inherent zero energy modes. All the results are listed in Tables 3 and 4.

For an n-edge element, the total number of element DOFs is $3n$. From the results listed in Tables 3 and 4, the proper relationship of the number DOFs $3n$, the number of analytical trial functions, n_{ATF}, and the number of element's inherent zero energy modes M, can be obtained. That is, when

$$n_{ATF} \geq 3n - M, \tag{58}$$

the element will not have spurious zero energy modes.

TABLE 3 Numbers of zero-energy modes with different numbers of element edges and analytical trial functions for polygonal plate elements

No. of analytical trial functions n_{ATF}		**7**	**11**	**15**	**19**	**23**	**27**
No. of element edges n	**No. of DOFs $3n$**	**Number of zero eigenvalues/nonzero eigenvalues**					
3	9	3/6	3/6	3/6			
4	12	5/7	3/9	3/9	3/9		
5	15	8/7	4/11	3/12	3/12	3/12	3/12
6	18	11/7	7/11	3/15	3/15	3/15	3/15
7	21		10/11	6/15	3/18	3/18	3/18
8	24		13/11	9/15	5/19	3/21	3/21
9	27			12/15	8/19	4/23	3/24
10	30				11/19	7/23	3/27

Abbreviation: DOF, degrees of freedom.

TABLE 4 Numbers of zero-energy modes with different numbers of element edges and analytical trial functions for polygonal membrane elements with drilling DOFs

No. of analytical trial functions n_{ATF}		7	11	15	19	23	27
No. of element edges n	**No. of DOFs $3n$**	**Number of zero eigenvalues/nonzero eigenvalues**					
3	9	4/5	4/5	4/5			
4	12	5/7	4/8	4/8	4/8		
5	15	8/7	4/11	4/11	4/11	4/11	4/11
6	18	11/7	7/11	4/14	4/14	4/14	4/11
7	21		10/11	6/15	4/17	4/17	4/17
8	24		13/11	9/15	5/19	4/20	4/20
9	27			12/15	8/19	4/23	4/23
10	30				11/19	7/23	4/26

Abbreviation: DOF, degrees of freedom.

TABLE 5 Reference selection scheme of the analytical trial functions for polygonal HDF plate and HSF membrane elements

Plate element		
Element edges n	**DOFs $3n$**	**Best-fit number of analytical solutions**
3	9	7
4	12	11
5	15	15
6	18	15
7	21	19
8	24	23
9	27	27
10	30	27
Membrane elements with drilling DOFs		
Element edges n	**DOFs $3n$**	**Best-fit number of analytical solutions**
3	9	7
4	12	11
5	15	11
6	18	15
7	21	19
8	24	23
9	27	23
10	30	27

Abbreviations: DOF, degrees of freedom; HDF, hybrid displacement-function; HSF, hybrid stress-function.

More analytical trial functions means the assumed stress fields possess higher-order completeness. But for a specified number of DOFs, over high-order interpolation functions will damage the numerical stability and computation efficiency. Therefore, the minimum number satisfying both Equation (58) and the completeness of analytical trial functions is the best-fit choice. For various HSF and HDF elements with different numbers of edges, the suggestions for the selected numbers of analytical trial functions are given in Table 5. Following these best-fit selection scheme of analytical trial functions, the corresponding arbitrary polygonal elements can be formulated.

3.2 | The formulations of polygonal flat shell element HSDF-PSH

The typical model of an arbitrary polygonal flat shell element is shown in Figure 6. The shell element has n sides and 2 nodes along each side, that is, the element has n nodes in total. First, suppose all the element nodes are coplanar. Thus, the element can be represented by its mid-face 123-n. For a flat shell, each element node has six DOFs. Thus, the element nodal displacement vector $\mathbf{q}^e$ can be defined as

$$\mathbf{q}^e = \begin{bmatrix} \mathbf{a}_1^{e\mathrm{T}} & \mathbf{a}_2^{e\mathrm{T}} & \cdots & \mathbf{a}_n^{e\mathrm{T}} \end{bmatrix}^{\mathrm{T}}, \tag{59}$$

$$\mathbf{a}_i^e = \begin{bmatrix} u_i & v_i & w_i & \theta_{xi} & \theta_{yi} & \theta_{zi} \end{bmatrix}^{\mathrm{T}}. \tag{60}$$

In order to construct a flat shell element, a local coordinate system is needed to divide the element into a plate bending part and a membrane part. The local coordinate system is also shown in Figure 6 and represented by (x', y', z'). As all the element nodes are supposed to be coplanar, the plane $12n$ is set to be the $x'O'y'$ plane. Then, the local coordinate system can be determined, and the transformation relationship between it and the global coordinate system can be expressed as

$$\begin{Bmatrix} x' \\ y' \\ z' \end{Bmatrix} = \begin{bmatrix} \lambda_{x'x} & \lambda_{x'y} & \lambda_{x'z} \\ \lambda_{y'x} & \lambda_{y'y} & \lambda_{y'z} \\ \lambda_{z'x} & \lambda_{z'y} & \lambda_{z'z} \end{bmatrix} \begin{Bmatrix} x \\ y \\ z \end{Bmatrix} = \boldsymbol{\lambda} \begin{Bmatrix} x \\ y \\ z \end{Bmatrix}, \tag{61}$$

in which

$$\begin{Bmatrix} \lambda_{x'x} \\ \lambda_{x'y} \\ \lambda_{x'z} \end{Bmatrix} = \frac{\mathbf{V}_1}{\|\mathbf{V}_1\|}, \begin{Bmatrix} \lambda_{z'x} \\ \lambda_{z'y} \\ \lambda_{z'z} \end{Bmatrix} = \frac{\mathbf{V}_3}{\|\mathbf{V}_3\|}, \begin{Bmatrix} \lambda_{y'x} \\ \lambda_{y'y} \\ \lambda_{y'z} \end{Bmatrix} = \frac{\mathbf{V}_3 \times \mathbf{V}_1}{\|\mathbf{V}_3 \times \mathbf{V}_1\|}, \tag{62}$$

$$\mathbf{V}_1 = \begin{Bmatrix} x_2 - x_1 \\ y_2 - y_1 \\ z_2 - z_1 \end{Bmatrix}, \mathbf{V}_2 = \begin{Bmatrix} x_n - x_1 \\ y_n - y_1 \\ z_n - z_1 \end{Bmatrix}, \mathbf{V}_3 = \mathbf{V}_1 \times \mathbf{V}_2, \tag{63}$$

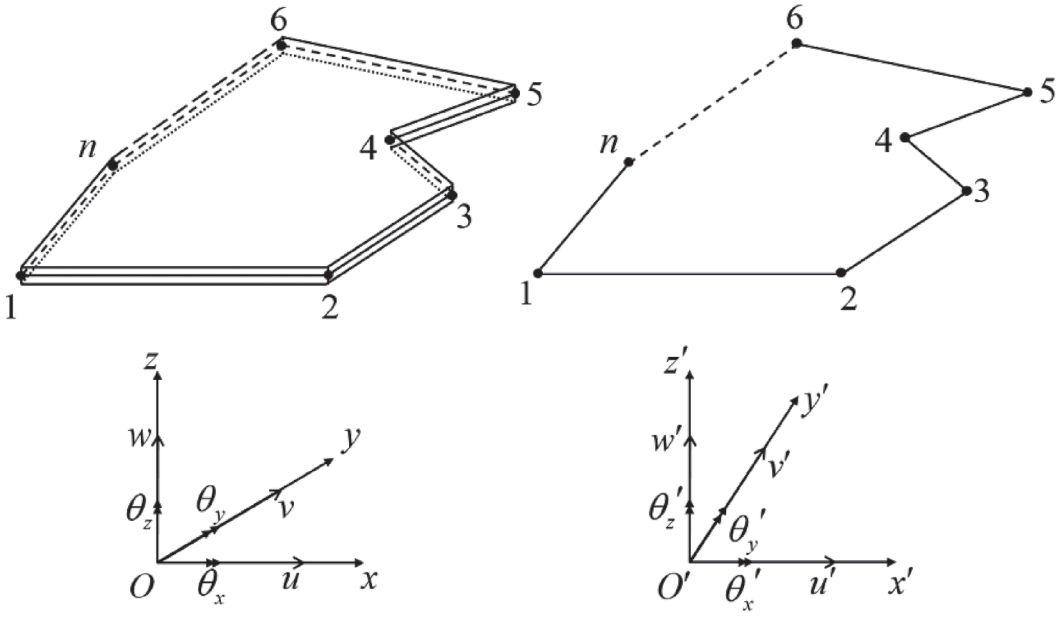

FIGURE 6 An arbitrary polygonal flat shell element and the corresponding local coordinate system

and $\|\cdot\|$ represents the modulus of vector. From above transformation, the element nodal displacement vector in local coordinate system can be obtained by

$$\mathbf{q}'^{e} = \mathbf{T}\mathbf{q}^{e}, \tag{64}$$

in which

$$\mathbf{q}'^{e} = \left\{ \mathbf{a}_1'^{e\mathrm{T}} \quad \mathbf{a}_2'^{e\mathrm{T}} \quad \cdots \quad \mathbf{a}_n'^{e\mathrm{T}} \right\}^{\mathrm{T}}, \tag{65}$$

$$\mathbf{a}_i'^{e} = \left[u_i' \quad v_i' \quad w_i' \quad \theta_{xi}' \quad \theta_{yi}' \quad \theta_{zi}' \right]^{\mathrm{T}}, \tag{66}$$

$$\mathbf{T} = \mathrm{diag}(\underbrace{\boldsymbol{\lambda}, \boldsymbol{\lambda}, \cdots, \boldsymbol{\lambda}}_{2n}). \tag{67}$$

It should be noted that the above choice for local frame may not always be optimal when the element is warped, which means not all element nodes are coplanar. Even so, the influence caused by element warping can be reduced by mesh refinement.

In the local coordinate system, the six DOFs in Equation (66) can be divided into two parts: the plate bending part $\mathbf{a}_{\mathrm{b}i}'^{e}$ and the membrane part $\mathbf{a}_{\mathrm{m}i}'^{e}$,

$$\mathbf{a}_{\mathrm{b}i}'^{e} = \left[w_i' \quad \theta_{xi}' \quad \theta_{yi}' \right]^{\mathrm{T}}, \tag{68}$$

$$\mathbf{a}_{\mathrm{m}i}'^{e} = \left[u_i' \quad v_i' \quad \theta_{zi}' \right]^{\mathrm{T}}. \tag{69}$$

The plate bending part can be obtained by the polygonal HDF Mindlin–Reissner plate element developed in Section 2.1, and the corresponding element stiffness matrix is denoted by $\mathbf{K}_p^e$. Note that the three DOFs of the plate bending part are not consistent with the DOFs of the plate element in Section 2.1. Therefore, a transformation is needed:

$$\mathbf{a}_{\mathrm{p}}'^{e} = \mathbf{t}_{\mathrm{b}}\mathbf{a}_{\mathrm{b}}'^{e}, \tag{70}$$

with

$$\mathbf{t}_{\mathrm{b}} = \begin{bmatrix} 1 & 0 & 0 \\ 0 & 0 & -1 \\ 0 & 1 & 0 \end{bmatrix}. \tag{71}$$

Thus, the element stiffness matrix of plate bending part can be obtained by

$$\mathbf{K}_{\mathrm{p}}^{e} = \mathbf{T}_{\mathrm{b}}^{\mathrm{T}}\mathbf{K}_{\mathrm{b}}^{e}\mathbf{T}_{\mathrm{b}}, \tag{72}$$

with

$$\mathbf{T}_{\mathrm{b}} = \mathrm{diag}(\underbrace{\mathbf{t}_{\mathrm{b}}, \mathbf{t}_{\mathrm{b}}, \cdots, \mathbf{t}_{\mathrm{b}}}_{n}). \tag{73}$$

The membrane part can be obtained by the polygonal HSF membrane element with drilling DOFs developed in Section 2.2, and the corresponding element stiffness matrix is denoted by $\mathbf{K}_{\mathrm{m}}^{e}$. Finally, assembling the two parts, the stiffness matrix of flat shell element in local coordinate system is obtained:

$$\mathbf{K}_{\mathrm{flat}}^{e} = \mathrm{assemble}(\mathbf{K}_{\mathrm{p}}^{e}, \mathbf{K}_{\mathrm{m}}^{e}). \tag{74}$$

The above construction procedures are based on that all element nodes are coplanar. However, in practical problems, the element may be warped. Therefore, it is necessary to modify the element stiffness matrix for better precision. In this article, the rigid link correction strategy proposed by Taylor[63] is employed.

While the element become warped, let d_i denotes the distance between node i and the plane $x'Oy'$, and the modified nodal DOFs can be expressed as

$$\begin{Bmatrix} u_i^{\bar{f}} \\ v_i^{\bar{f}} \\ w_i^{\bar{f}} \\ \theta_{xi}^{\bar{f}} \\ \theta_{yi}^{\bar{f}} \\ \theta_{zi}^{\bar{f}} \end{Bmatrix} = \begin{bmatrix} 1 & & & & & \\ 0 & 1 & & & & \\ 0 & 0 & 1 & & & \\ 0 & d_i & 0 & 1 & & \\ -d_i & 0 & 0 & 0 & 1 & \\ 0 & 0 & 0 & 0 & 0 & 1 \end{bmatrix} \begin{Bmatrix} u_i^r \\ v_i^r \\ w_i^r \\ \theta_{xi}^r \\ \theta_{yi}^r \\ \theta_{zi}^r \end{Bmatrix} = \mathbf{W}_i \begin{Bmatrix} u_i^r \\ v_i^r \\ w_i^r \\ \theta_{xi}^r \\ \theta_{yi}^r \\ \theta_{zi}^r \end{Bmatrix}, \tag{75}$$

in which the superscript $\bar{f}$ represents the DOF after modification, and the superscript r represent the DOF before modification. Thus, the element stiffness matrix can be modified as

$$\mathbf{K}_{\text{local}}^e = \mathbf{W}_K \mathbf{K}_{\text{flat}}^e \mathbf{W}_K^{\text{T}}, \tag{76}$$

with

$$\mathbf{W}_K = \text{diag}(\mathbf{W}_1, \mathbf{W}_2, \cdots, \mathbf{W}_n). \tag{77}$$

Finally, according to the transformation relationship, the stiffness matrix of flat shell element in the global coordinate system can be obtained:

$$\mathbf{K}_{\text{global}}^e = \mathbf{T}^{\text{T}} \mathbf{K}_{\text{local}}^e \mathbf{T}. \tag{78}$$

With the procedures introduced in this section, an arbitrary polygonal hybrid stress/displacement function (HSDF) flat shell element is constructed, which is uniformly denoted by HSDF-PSH. In order to distinguish the number of element edges, a polygonal element with n edges can also be denoted by HSDF-PSHn.

4 | GEOMETRICALLY NONLINEAR FORMULATIONS FOR ARBITRARY POLYGONAL FLAT SHELL ELEMENT HSDF-PSH

4.1 | Geometrically nonlinear formulations of arbitrary polygonal elements based on the CR method

As described in Introduction, Felippa and Haugen[53] proposed a relatively complete formulation of the CR method for conventional triangular and quadrilateral elements. According to their derivations, a unified formulation for arbitrary polygonal elements with the analytical trial functions is established in this section. Only the final element formulations with the essential expressions are given here, and more details can be found in Reference 53.

The main feature of the CR method is to decompose a large-rotation, small-strain geometric nonlinear problem into an element rigid body translation and an element local small deformation, so that any linear element stiffness matrix can be extended to geometrically nonlinear analyses. The related element configurations, coordinate systems, and kinematics of the CR method are shown in Figure 7. In order to implement the decomposition, three configurations should be defined: initial configuration $\mathfrak{R}^0$, CR configuration $\mathfrak{R}^{\text{R}}$, and deformed configuration $\mathfrak{R}^{\text{D}}$. The motion from $\mathfrak{R}^0$ to $\mathfrak{R}^{\text{R}}$ represents the rigid body translation, while the motion from $\mathfrak{R}^{\text{R}}$ to $\mathfrak{R}^{\text{D}}$ represents the local small deformation. The global coordinate system is denoted by $\mathbf{G}$; the local coordinate system based on initial configuration $\mathfrak{R}^0$ is denoted by $\mathbf{E}^0$, with the corresponding base vectors $(\mathbf{e}_1^0, \mathbf{e}_2^0, \mathbf{e}_3^0)$; the local coordinate system based on CR configuration $\mathfrak{R}^{\text{R}}$ is denoted by $\mathbf{E}^{\text{R}}$, with the corresponding base vectors $(\mathbf{e}_1, \mathbf{e}_2, \mathbf{e}_3)$; the local coordinate system based on deformed configuration $\mathfrak{R}^{\text{D}}$ is the same to $\mathfrak{R}^{\text{R}}$, that is, $\mathbf{E} = \mathbf{E}^{\text{R}}$. The two local coordinate systems are determined by the transformation matrices from global coordinate system:

$$\mathbf{T}_0^{\text{T}} = \begin{bmatrix} \mathbf{e}_1^0 & \mathbf{e}_2^0 & \mathbf{e}_3^0 \end{bmatrix}, \tag{79}$$

$$\mathbf{T}^{\text{T}} = \begin{bmatrix} \mathbf{e}_1 & \mathbf{e}_2 & \mathbf{e}_3 \end{bmatrix}. \tag{80}$$

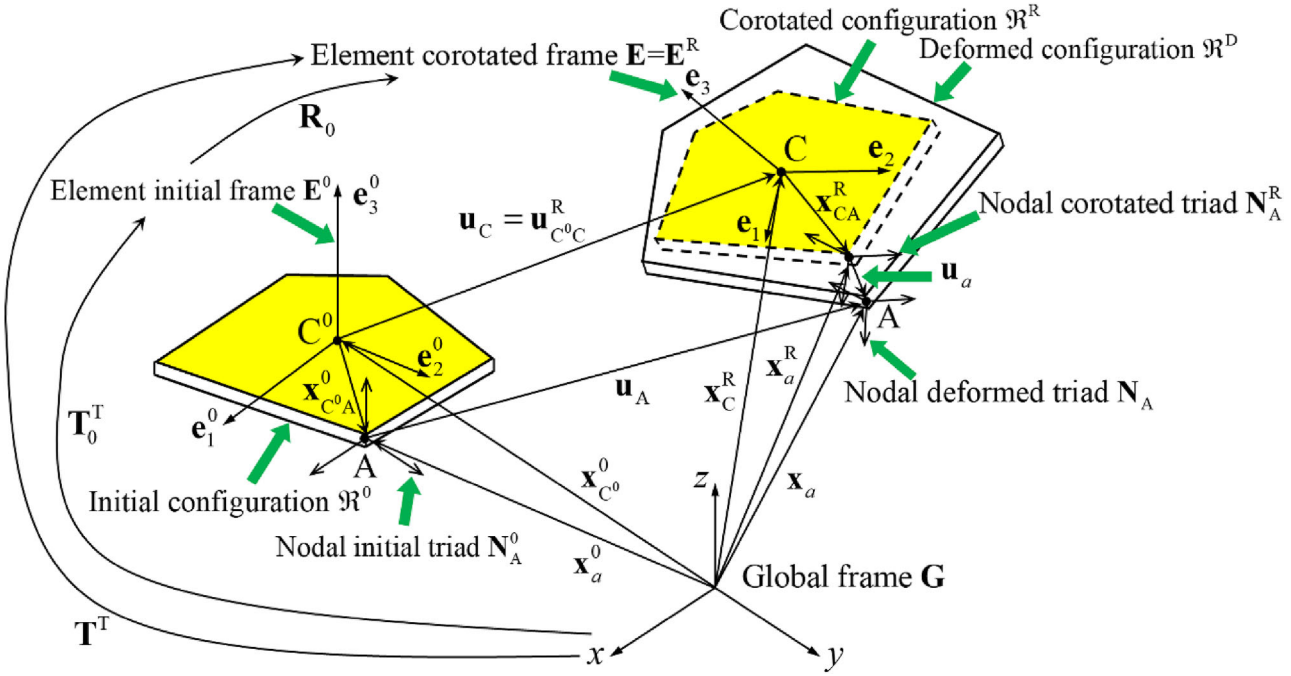

FIGURE 7 Element configurations, coordinate systems, and kinematics of corotational method

From the derivation in Reference 53, it can be seen that the selection of $\mathbf{E}^0$ does not affect the final expressions. Therefore, for an element with n edges, just three nodes, Nodes 1, 2, and n, are employed to set the initial configuration. The expressions are:

$$\mathbf{e}_1^0 = \frac{\mathbf{x}_{21}^0}{\|\mathbf{x}_{21}^0\|}, \mathbf{e}_3^0 = \frac{\mathbf{x}_{21}^0 \times \mathbf{x}_{n1}^0}{\|\mathbf{x}_{21}^0 \times \mathbf{x}_{n1}^0\|}, \mathbf{e}_2^0 = \mathbf{e}_3^0 \times \mathbf{e}_1^0, \tag{81}$$

with

$$\mathbf{x}_{ab}^0 = \mathbf{x}_a^0 - \mathbf{x}_b^0, (a, b = 1, 2, \cdots, n), \tag{82}$$

where $\mathbf{x}_a^0$ and $\mathbf{x}_b^0$ are the global coordinates of Nodes a and b.

The selection of CR configuration $\mathbf{E} = \mathbf{E}^R$ is required to satisfy that, the deformation is small enough so that the local deformation can be treated as a linear problem. Related selection scheme for arbitrary polygonal elements will be introduced in Section 4.2.

The geometrically nonlinear problems are usually solved by increment formulation. Therefore, in each increment step, the initial configuration $\mathfrak{R}^0$ is the configuration at the moment t, with t corresponding the initial time of the step. Thus, the global coordinates $\mathbf{x}_a^0 (a = 1, 2, \cdots, n)$ in Equation (82) are written as ${}^t\mathbf{x}_a (a = 1, 2, \cdots, n)$ in each increment step. Let $t + \Delta t$ denotes the end moment of the incremental step, so the total displacement vector can be written as

$${}^{t+\Delta t}\mathbf{q}_a^e = \left[{}^{t+\Delta t}u_{a1} \quad {}^{t+\Delta t}u_{a2} \quad {}^{t+\Delta t}u_{a3} \quad {}^{t+\Delta t}\theta_{a1} \quad {}^{t+\Delta t}\theta_{a2} \quad {}^{t+\Delta t}\theta_{a3} \right]^T, \tag{83}$$

where ${}^{t+\Delta t}u_{a1}, {}^{t+\Delta t}u_{a2}, {}^{t+\Delta t}u_{a3}$ denote the translations of Node A, and ${}^{t+\Delta t}\theta_{a1}, {}^{t+\Delta t}\theta_{a2}, {}^{t+\Delta t}\theta_{a3}$ denote the rotations. From the rotation vector ${}^{t+\Delta t}\boldsymbol{\theta}_a = \left[{}^{t+\Delta t}\theta_{a1} \quad {}^{t+\Delta t}\theta_{a2} \quad {}^{t+\Delta t}\theta_{a3} \right]^T$, the corresponding 3×3 rotation matrix ${}^{t+\Delta t}\mathbf{R}_a$ can be obtained (see Appendix A). Then, the coordinates ${}^{t+\Delta t}\overline{\mathbf{x}}_a (a = 1, 2, \cdots, n)$, the translations ${}^{t+\Delta t}\overline{\mathbf{u}}_{da} (a = 1, 2, \cdots, n)$, and rotations ${}^{t+\Delta t}\overline{\mathbf{R}}_{da} (a = 1, 2, \cdots, n)$ in the local coordinate system can be expressed by

$${}^{t+\Delta t}\overline{\mathbf{x}}_a = \mathbf{T}({}^t\mathbf{x}_a + {}^{t+\Delta t}\mathbf{u}_a - {}^t\mathbf{x}_{C0} - {}^{t+\Delta t}\mathbf{u}_C), \tag{84}$$

$$^{t+\Delta t}\overline{\mathbf{u}}_{\mathrm{d}a} = \mathbf{T}(^{t}\mathbf{x}_a + ^{t+\Delta t}\mathbf{u}_a - ^{t}\mathbf{x}_{\mathrm{C0}} - ^{t+\Delta t}\mathbf{u}_{\mathrm{C}}) - ^{t}\mathbf{x}_{\mathrm{C^0A}}, \tag{85}$$

$$^{t+\Delta t}\overline{\mathbf{R}}_{\mathrm{d}a} = \mathbf{T}^{t+\Delta t}\mathbf{R}_a\mathbf{T}_0^{\mathrm{T}}, \tag{86}$$

where $^{t}\mathbf{x}_{\mathrm{C0}}$ denotes the coordinate vector of the element centroid C^0:

$$^{t}\mathbf{x}_{\mathrm{C0}} = \frac{1}{n}\sum_{i=1}^{n}{}^{t}\mathbf{x}_a, \quad ^{t}\mathbf{x}_{\mathrm{C^0A}} = {}^{t}\mathbf{x}_a - {}^{t}\mathbf{x}_{\mathrm{C0}}. \tag{87}$$

From rotation $^{t+\Delta t}\overline{\mathbf{R}}_{\mathrm{d}a}$, the corresponding rotation vector ${}_{\mathrm{d}a}\overline{\boldsymbol{\theta}}_{t+\Delta t}$ can also be obtained (see Appendix A).

Thus, similar to $\mathbf{K}^e_{\mathrm{local}}$ in Equation (76), the element stiffness matrix $^{t+\Delta t}\overline{\mathbf{K}}^e$ at time $t+\Delta t$ can be formulated in local coordinates. And the increment displacements can be written as

$$^{t+\Delta t}\overline{\mathbf{q}}^e = \left\{ {}^{t+\Delta t}\overline{\mathbf{u}}_{\mathrm{d1}}^{\mathrm{T}} \quad {}^{t+\Delta t}\overline{\boldsymbol{\theta}}_{\mathrm{d1}}^{\mathrm{T}} \quad {}^{t+\Delta t}\overline{\mathbf{u}}_{\mathrm{d2}}^{\mathrm{T}} \quad {}^{t+\Delta t}\overline{\boldsymbol{\theta}}_{\mathrm{d2}}^{\mathrm{T}} \quad \cdots \quad \cdots \quad {}^{t+\Delta t}\overline{\mathbf{u}}_{\mathrm{d}n}^{\mathrm{T}} \quad {}^{t+\Delta t}\overline{\boldsymbol{\theta}}_{\mathrm{d}n}^{\mathrm{T}} \right\}^{\mathrm{T}}. \tag{88}$$

Then, the inner force vector $^{t+\Delta t}\overline{\mathbf{f}}^e$ can be obtained:

$$^{t+\Delta t}\overline{\mathbf{f}}^e = {}^{t+\Delta t}\overline{\mathbf{K}}^e\,{}^{t+\Delta t}\overline{\mathbf{q}}^e. \tag{89}$$

It should be noted that the construction of $^{t+\Delta t}\overline{\mathbf{K}}^e$ is based on local coordinates in current configuration. Therefore, for element HSDF-PSH, the analytical trial functions should be updated in each step according to the current element configuration. This operation will be introduced in Section 4.3.

The element inner force vector in global coordinate system is

$$^{t+\Delta t}\mathbf{f}^e = \mathbf{T}_{\mathrm{E}}^{\mathrm{T}}\overline{\mathbf{P}}^{\mathrm{T}}\overline{\mathbf{H}}^{\mathrm{T}}\,{}^{t+\Delta t}\overline{\mathbf{f}}^e, \tag{90}$$

where

$$\mathbf{T}_{\mathrm{E}} = \mathrm{diag}\underbrace{\left[\mathbf{T} \quad \mathbf{T} \quad \cdots \quad \mathbf{T}\right]}_{n}, \tag{91}$$

$$\overline{\mathbf{H}} = \mathrm{diag}\left(\mathbf{I}_3 \quad \overline{\mathbf{H}}_1 \quad \mathbf{I}_3 \quad \overline{\mathbf{H}}_2 \quad \cdots \quad \cdots \quad \mathbf{I}_3 \quad \overline{\mathbf{H}}_n\right), \tag{92}$$

$$\overline{\mathbf{P}} = \overline{\mathbf{P}}_u - \overline{\mathbf{P}}_\omega = \overline{\mathbf{P}}_u - \overline{\mathbf{S}}\overline{\mathbf{G}}, \tag{93}$$

$$\overline{\mathbf{G}} = \left[\overline{\mathbf{G}}_1 \quad \mathbf{0}_3 \quad \overline{\mathbf{G}}_2 \quad \mathbf{0}_3 \quad \cdots \quad \cdots \quad \overline{\mathbf{G}}_n \quad \mathbf{0}_3\right], \tag{94}$$

in which $\mathbf{I}_3$ denotes the 3×3 identity matrix; $\overline{\mathbf{G}}_a (i = 1, 2, \cdots, n)$ are related to the choice of local frame and its expressions, and will be given in Section 4.2; $\overline{\mathbf{H}}_a (i = 1, 2, \cdots, n)$, $\overline{\mathbf{P}}_u$, and $\overline{\mathbf{S}}$ will be given in Appendix B.

The element tangent stiffness matrix in global coordinate system is

$$^{t+\Delta t}\mathbf{K}^e = \mathbf{K}_{\mathrm{GR}} + \mathbf{K}_{\mathrm{GP}} + \mathbf{K}_{\mathrm{GM}} + \mathbf{K}_{\mathrm{M}}, \tag{95}$$

$$\begin{aligned} \mathbf{K}_{\mathrm{GR}} &= -\mathbf{T}_{\mathrm{E}}^{\mathrm{T}}\overline{\mathbf{F}}_{\mathrm{nm}}\overline{\mathbf{G}}\mathbf{T}_{\mathrm{E}}, \mathbf{K}_{\mathrm{GP}} = -\mathbf{T}_{\mathrm{E}}^{\mathrm{T}}\overline{\mathbf{G}}^{\mathrm{T}}\overline{\mathbf{F}}_{\mathrm{n}}^{\mathrm{T}}\overline{\mathbf{P}}\mathbf{T}_{\mathrm{E}} \\ \mathbf{K}_{\mathrm{GM}} &= \mathbf{T}_{\mathrm{E}}^{\mathrm{T}}\overline{\mathbf{P}}^{\mathrm{T}}\overline{\mathbf{L}}\overline{\mathbf{P}}\mathbf{T}_{\mathrm{E}}, \mathbf{K}_{\mathrm{M}} = \mathbf{T}_{\mathrm{E}}^{\mathrm{T}}\overline{\mathbf{P}}^{\mathrm{T}}\overline{\mathbf{H}}^{\mathrm{T}}\overline{\mathbf{K}}\overline{\mathbf{H}}\overline{\mathbf{P}}\mathbf{T}_{\mathrm{E}}, \end{aligned} \tag{96}$$

where

$$\overline{\mathbf{F}}_{\mathrm{nm}} = \left[\mathrm{spin}(\overline{\mathbf{n}}_1)^{\mathrm{T}} \quad \mathrm{spin}(\overline{\mathbf{m}}_1)^{\mathrm{T}} \quad \cdots \quad \cdots \quad \mathrm{spin}(\overline{\mathbf{n}}_n)^{\mathrm{T}} \quad \mathrm{spin}(\overline{\mathbf{m}}_n)^{\mathrm{T}}\right]^{\mathrm{T}}, \tag{97}$$

$$\overline{\mathbf{F}}_{\mathrm{n}} = \left[\mathrm{spin}(\overline{\mathbf{n}}_1)^{\mathrm{T}} \quad \mathbf{0}_3 \quad \cdots \quad \cdots \quad \mathrm{spin}(\overline{\mathbf{n}}_n)^{\mathrm{T}} \quad \mathbf{0}_3\right]^{\mathrm{T}}, \tag{98}$$

$$\overline{\mathbf{L}} = \mathrm{diag}\underbrace{\left[\mathbf{0}_3 \quad \overline{\mathbf{L}}_1 \quad \cdots \quad \cdots \quad \mathbf{0}_3 \quad \overline{\mathbf{L}}_n\right]}_{n}, \tag{99}$$

in which $\overline{\mathbf{n}}_i$ and $\overline{\mathbf{m}}_i (i = 1, 2, \cdots, n)$ represent the inner force and inner moment in the local frame after projection:

$$\mathbf{f}_{\mathrm{P}} = \overline{\mathbf{P}}^{\mathrm{T}} \overline{\mathbf{H}}^{\mathrm{T}^{t+\Delta t}} \overline{\mathbf{f}} = \left\{\overline{\mathbf{n}}_1^{\mathrm{T}} \quad \overline{\mathbf{m}}_1^{\mathrm{T}} \quad \overline{\mathbf{n}}_2^{\mathrm{T}} \quad \overline{\mathbf{m}}_2^{\mathrm{T}} \quad \cdots \quad \cdots \quad \overline{\mathbf{n}}_n^{\mathrm{T}} \quad \overline{\mathbf{m}}_n^{\mathrm{T}}\right\}^{\mathrm{T}}, \tag{100}$$

and

$$\mathrm{spin}(\overline{\mathbf{n}}_a) = \begin{bmatrix} 0 & -\overline{n}_{a3} & \overline{n}_{a2} \\ \overline{n}_{a3} & 0 & -\overline{n}_{a1} \\ -\overline{n}_{a2} & \overline{n}_{a1} & 0 \end{bmatrix}, \mathrm{spin}(\overline{\mathbf{m}}_a) = \begin{bmatrix} 0 & -\overline{m}_{a3} & \overline{m}_{a2} \\ \overline{m}_{a3} & 0 & -\overline{m}_{a1} \\ -\overline{m}_{a2} & \overline{m}_{a1} & 0 \end{bmatrix}, \tag{101}$$

$$\overline{\mathbf{n}}_a = \left[\overline{n}_{a1} \quad \overline{n}_{a2} \quad \overline{n}_{a3}\right]^{\mathrm{T}}, \overline{\mathbf{m}}_a = \left[\overline{m}_{a1} \quad \overline{m}_{a2} \quad \overline{m}_{a3}\right]^{\mathrm{T}}. \tag{102}$$

The expressions of $\overline{\mathbf{L}}_a (a = 1, 2, \cdots, n)$ can also be found in Appendix B.

In this article, the nonlinear solver of Abaqus/Standard is adopted by the user-defined subroutine.[64] The major procedures are shown in Figure 8.

4.2 | The selection scheme of the best-fit CR frame

Considering an arbitrary polygonal flat shell element without warping. Obviously, one coordinate plane of the best-fit CR frame should be the element plane. Thus, two steps are needed to determine the best-fit frame: first, establish an initial mid-frame, in which one coordinate plane is the element plane; second, determine the final best-fit CR frame by appending an in-plane rotation to the mid-frame.

In order to satisfy the small-deformation assumption in the local CR coordinate system, the selection of the best-fit CR frame must insure that the nodal displacements are small enough. Generally, the small-deformation condition can be set by minimizing the sum of element nodal displacements in the best-fit coordinate system.[65] There are two different reference configurations for the nodal displacements: one is the initial configuration, in which the total displacements will be employed during the whole analytical step; the other is the current configuration, in which the incremental displacements will be adopted in the current increment step. Although the best-fit selection based on the current configuration is more precise, but for small-strain problems, the element nodal displacements in the local coordinate system is small enough, so that the results based on both configurations are almost identical. Because the procedures based on the initial configuration are more convenient, most proposed best-fit frame selection schemes prefer to the initial configuration. Of course, for finite-strain geometrically nonlinear analyses, the procedures based on the current configuration are still necessary. In this article, only small-strain condition is considered, that is, the best-fit CR frame for element HSDF-PSH is based on the initial configuration.

First, define a coordinate plane and a coordinate axis perpendicular to the coordinate plane formed by Nodes 1, 2, and n. Thus, the mid-frame can be obtained, with its three base vectors:

$$\mathbf{e}_1^{\mathrm{M}} = \frac{\mathbf{x}_{21}^0}{\|\mathbf{x}_{21}^0\|}, \mathbf{e}_3^{\mathrm{M}} = \frac{\mathbf{x}_{21}^0 \times \mathbf{x}_{n1}^0}{\|\mathbf{x}_{21}^0 \times \mathbf{x}_{n1}^0\|}, \mathbf{e}_2^{\mathrm{M}} = \mathbf{e}_3^0 \times \mathbf{e}_1^0, \tag{103}$$

in which subscript "M" denotes mid-frame. The transformation matrix between this mid-frame and global frame can be written as

$$\mathbf{R}_{\mathrm{M}} = \left[\mathbf{e}_1^{\mathrm{M}} \quad \mathbf{e}_2^{\mathrm{M}} \quad \mathbf{e}_3^{\mathrm{M}}\right]. \tag{104}$$

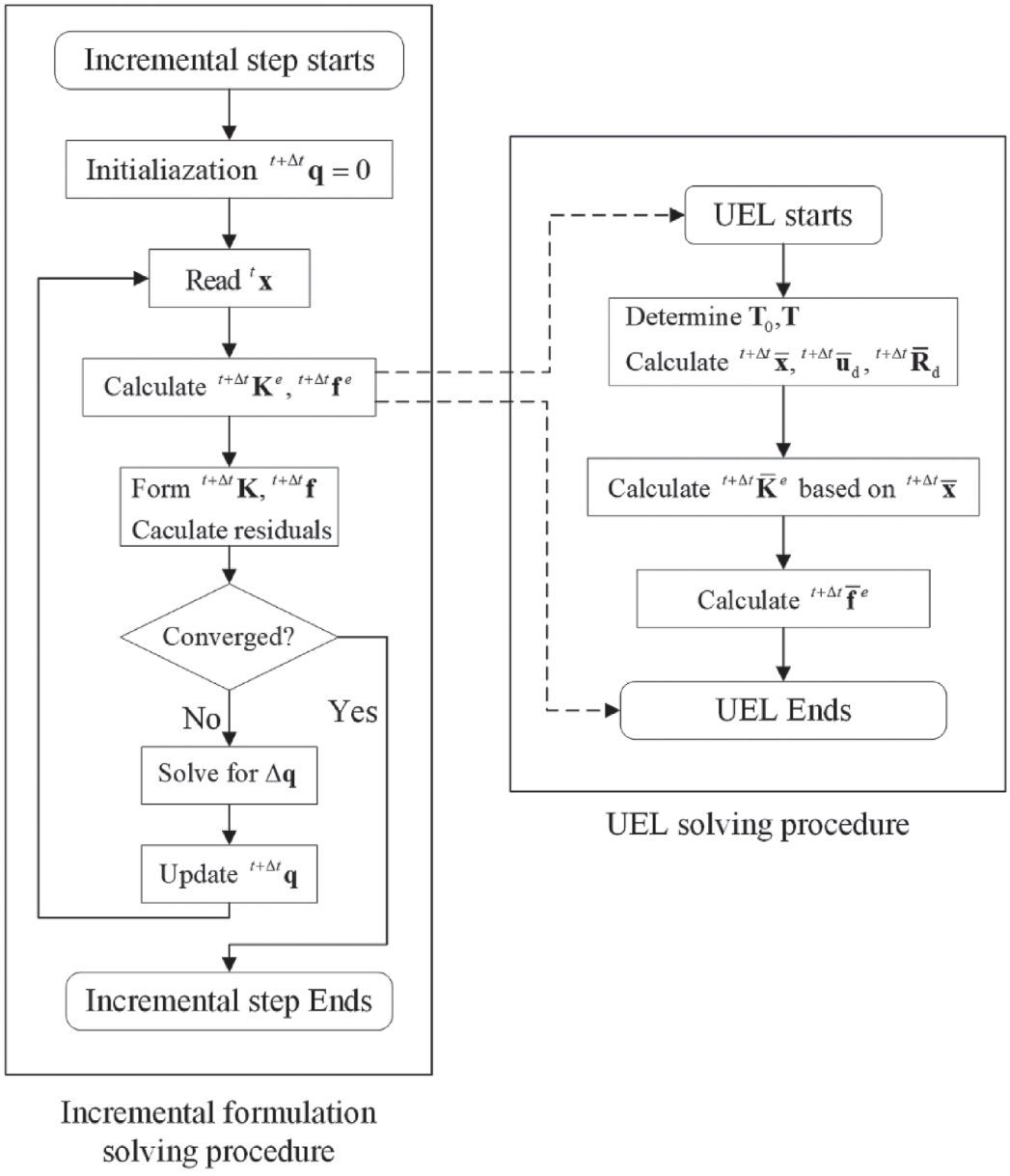

FIGURE 8 Geometrically nonlinear incremental formulation solving procedure

Let $\boldsymbol{\omega}_{\mathrm{M}}$ be the pseudo-vector corresponding to rotation $\mathbf{R}_{\mathrm{M}}$. Then, the infinitesimal variation of $\mathbf{R}_{\mathrm{M}}$ is

$$\delta\mathbf{R}_{\mathrm{M}} = \mathbf{R}_{\mathrm{M}}\delta\boldsymbol{\omega}_{\mathrm{M}}, \tag{105}$$

consequently,

$$\delta\boldsymbol{\omega}_{\mathrm{M}} = \begin{bmatrix} \delta\omega_{\mathrm{M1}} \\ \delta\omega_{\mathrm{M2}} \\ \delta\omega_{\mathrm{M3}} \end{bmatrix} = \begin{bmatrix} -\mathbf{e}_2^{\mathrm{MT}}\delta\mathbf{e}_3^{\mathrm{M}} \\ \mathbf{e}_1^{\mathrm{MT}}\delta\mathbf{e}_3^{\mathrm{M}} \\ \mathbf{e}_2^{\mathrm{MT}}\delta\mathbf{e}_1^{\mathrm{M}} \end{bmatrix}. \tag{106}$$

In local coordinate system, the variation of $\mathbf{e}_3^{\mathrm{M}}$ is (see Reference 65):

$$\delta\mathbf{e}_3^{\mathrm{M}} = \frac{1}{\|\mathbf{x}_{21}\times\mathbf{x}_{n1}\|}\left(\begin{bmatrix}\delta\overline{u}_2-\delta\overline{u}_1\\ \delta\overline{v}_2-\delta\overline{v}_1\\ \delta\overline{w}_2-\delta\overline{w}_1\end{bmatrix}\times\begin{bmatrix}\overline{x}_n-\overline{x}_1\\ \overline{y}_n-\overline{y}_1\\ 0\end{bmatrix}+\begin{bmatrix}\overline{x}_2-\overline{x}_1\\ \overline{y}_2-\overline{y}_1\\ 0\end{bmatrix}\times\begin{bmatrix}\delta\overline{u}_n-\delta\overline{u}_1\\ \delta\overline{v}_n-\delta\overline{v}_1\\ \delta\overline{w}_n-\delta\overline{w}_1\end{bmatrix}\right) + \delta\left(\frac{1}{\|\mathbf{x}_{21}\times\mathbf{x}_{n1}\|}\right)\mathbf{x}_{21}\times\mathbf{x}_{n1}, \tag{107}$$

where $\overline{x}_a, \overline{y}_a, \overline{z}_a (a = 1, 2, \cdots, n)$ are element nodal local coordinates after deformation at the moment $t + \Delta t$. Here, the subscript "$t + \Delta t$" is omitted for convenience). And the corresponding infinitesimal variations of displacements are $\delta\overline{u}_a, \delta\overline{v}_a, \delta\overline{w}_a (a = 1, 2, \cdots, n)$.

Substitution of Equation (107) into Equation (106) yields

$$\begin{aligned}\delta\omega_{\mathrm{M1}} &= \frac{1}{\|\mathbf{x}_{21}\times\mathbf{x}_{n1}\|}[(\overline{x}_n-\overline{x}_2)\delta\overline{w}_1+(\overline{x}_1-\overline{x}_n)\delta\overline{w}_2+(\overline{x}_2-\overline{x}_1)\delta\overline{w}_n],\\ \delta\omega_{\mathrm{M2}} &= \frac{1}{\|\mathbf{x}_{21}\times\mathbf{x}_{n1}\|}[(\overline{y}_n-\overline{y}_2)\delta\overline{w}_1+(\overline{y}_1-\overline{y}_n)\delta\overline{w}_2+(\overline{y}_2-\overline{y}_1)\delta\overline{w}_n].\end{aligned} \tag{108}$$

Second, let the element rotate around the axis $\mathbf{e}_3^{\mathrm{M}}$ with an angle ω, a new frame will be obtained, in which the coordinates of element node a can be expressed by

$$\overline{x}_{an} = \overline{x}_a\cos\omega + \overline{y}_a\sin\omega, \overline{y}_{an} = -\overline{x}_a\sin\omega + \overline{y}_a\cos\omega. \tag{109}$$

The small-strain condition is set by minimizing the sum of square of all the element nodal displacements, that is,

$$\min\left\{\sum_{a=1}^{n}[(\overline{x}_a\cos\omega+\overline{y}_a\sin\omega-\overline{X}_a^{\mathrm{M}})^2+(-\overline{x}_a\sin\omega+\overline{y}_a\cos\omega-\overline{Y}_a^{\mathrm{M}})^2]\right\}, \tag{110}$$

where $(\overline{X}_a^{\mathrm{M}}, \overline{Y}_a^{\mathrm{M}})$ are the local coordinates of Node a in mid-frame before deformation. From the condition given by Equation (110), the tangent of angle ω can be obtained:

$$\tan\omega = \frac{\sum_{a=1}^{n}(y_aX_a - x_aY_a)}{\sum_{a=1}^{n}(x_aX_a + y_aY_a)}. \tag{111}$$

After rotate ω, Equation (108) remains unchanged, that is, $\delta\omega_1 = \delta\omega_{\mathrm{M1}}$, $\delta\omega_2 = \delta\omega_{\mathrm{M2}}$ and

$$\frac{\partial\omega_3}{\partial u_a} = \frac{-Y_a}{\sum_{a=1}^{n}(x_{an}X_a + y_{an}Y_a)}, \frac{\partial\omega_3}{\partial v_a} = \frac{X_a}{\sum_{a=1}^{n}(x_{an}X_a + y_{an}Y_a)}, \tag{112}$$

where $\boldsymbol{\omega} = \begin{Bmatrix}\omega_1 & \omega_2 & \omega_3\end{Bmatrix}^{\mathrm{T}}$ is the pseudo-vector corresponding to finial rotation $\mathbf{T}$ in Equation (80). According to Equations (108) and (112), the expression of $\overline{\mathbf{G}}_a$ in Equation (94) can be expressed by:

$$\overline{\mathbf{G}}_a = \begin{bmatrix}0 & 0 & g_{ua}\\ 0 & 0 & g_{va}\\ g_{wa1} & g_{wa2} & 0\end{bmatrix}, \tag{113}$$

with

$$g_{ua} = \frac{-\overline{Y}_a}{\sum_{a=1}^{n}(\overline{x}_{an}\overline{X}_a^{\mathrm{M}} + y_{an}\overline{Y}_a^{\mathrm{M}})}, \tag{114}$$

$$g_{va} = \frac{\overline{X}_a}{\sum_{a=1}^{n}(\overline{x}_{an}\overline{X}_a^{\mathrm{M}} + \overline{y}_{an}\overline{Y}_a^{\mathrm{M}})}, \tag{115}$$

$$g_{wa1} = \begin{cases} \frac{\bar{x}_n - \bar{x}_2}{\|\mathbf{x}_{21} \times \mathbf{x}_{n1}\|}, a = 1 \\ \frac{\bar{x}_1 - \bar{x}_n}{\|\mathbf{x}_{21} \times \mathbf{x}_{n1}\|}, a = 2 \\ \frac{\bar{x}_2 - \bar{x}_1}{\|\mathbf{x}_{21} \times \mathbf{x}_{n1}\|}, a = n \\ 0, a \neq 1, 2, n \end{cases}, \tag{116}$$

$$g_{wa2} = \begin{cases} \frac{\bar{y}_n - \bar{y}_2}{\|\mathbf{x}_{21} \times \mathbf{x}_{n1}\|}, a = 1 \\ \frac{\bar{y}_1 - \bar{y}_n}{\|\mathbf{x}_{21} \times \mathbf{x}_{n1}\|}, a = 2 \\ \frac{\bar{y}_2 - \bar{y}_1}{\|\mathbf{x}_{21} \times \mathbf{x}_{n1}\|}, a = n \\ 0, a \neq 1, 2, n \end{cases}. \tag{117}$$

The transformation matrix in second step is

$$\mathbf{R}_\omega = \begin{bmatrix} \cos\omega & \sin\omega & 0 \\ -\sin\omega & \cos\omega & 0 \\ 0 & 0 & 1 \end{bmatrix}, \tag{118}$$

and the transformation matrix between the best-fit CR frame and global frame can be expressed by

$$\mathbf{T} = \mathbf{R}_\omega \mathbf{R}_{\mathrm{M}}. \tag{119}$$

Thus, $\mathbf{T}$ in Equation (80) can be obtained by Equation (119) and the best-fit frame is determined.

4.3 | Updating analytical trial functions in CR formulation

In most geometric nonlinear analyses, the incremental finite element equations should be solved. For conventional FEM, the element stiffness matrix is usually expressed only in terms of local coordinates, which means it does not depend on the element configuration, so that TL and UL formulations are equivalent. However, for the HSF and HDF elements, things become quite different. As mentioned in Section 2, the formulations of the proposed element HSDF-PSH employed the analytical trial functions expressed in terms of Cartesian coordinates, which implies that its formulations have close relationship with element configuration. Therefore, for element HSDF-PSH, only UL formulation can be adopted, which means the analytical trial functions must be updated in each increment step during geometrically nonlinear analyses.

Let the initial time be 0, the beginning time of current increment step be t, the end time of current increment step be $t + \Delta t$. Thus, the corresponding element nodal coordinate vectors are denoted by ${}^0\mathbf{x}$, ${}^t\mathbf{x}$, ${}^{t+\Delta t}\mathbf{x}$, respectively. At time $t + \Delta t$, by using transformation relationship Equation (84), the local coordinate vector ${}^{t+\Delta t}\mathbf{x}$ can be obtained from ${}^t\mathbf{x}$. And according to the local coordinate system selection scheme of flat shell elements, the element nodal coordinate vector can be written as ${}^{t+\Delta t}\overline{\mathbf{x}}_a = [{}^{t+\Delta t}\overline{x}_a, {}^{t+\Delta t}\overline{y}_a, 0]^{\mathrm{T}}$.

Substitution of ${}^{t+\Delta t}\overline{x}_a$ and ${}^{t+\Delta t}\overline{y}_a$ into the expressions of Airy stress function ϕ and displacement function F yields the Airy stress function ${}^{t+\Delta t}\overline{\phi}$ and displacement function ${}^{t+\Delta t}\overline{F}$ in local coordinate system, which are expressed in terms of the analytical trial functions in local coordinates:

$${}^{t+\Delta t}\overline{\phi} = \sum_{i=1}^{n_\phi} \overline{\phi}_i \left({}^{t+\Delta t}\overline{x}_a, {}^{t+\Delta t}\overline{y}_a \right) \beta_{\mathrm{mi}}, \tag{120}$$

$${}^{t+\Delta t}\overline{F} = \sum_{i=1}^{m_F} {}^{t+\Delta t}\overline{F}_i^0 \left({}^{t+\Delta t}\overline{x}_a, {}^{t+\Delta t}\overline{y}_a \right) \beta_{\mathrm{bi}} + {}^{t+\Delta t}\overline{F}^* \left({}^{t+\Delta t}\overline{x}_a, {}^{t+\Delta t}\overline{y}_a \right). \tag{121}$$

Then, in local coordinate system, the stress matrix ${}^{t+\Delta t}\overline{\mathbf{S}}_{\mathrm{m}}$ of the HSF element, the resultant matrix ${}^{t+\Delta t}\overline{\mathbf{S}}_{\mathrm{b}}$, and the resultant particular solution vector ${}^{t+\Delta t}\overline{\mathbf{R}}_{\mathrm{b}}^{*}$ of the HDF element, can be written as:

$$ {}^{t+\Delta t}\overline{\mathbf{S}}_{\mathrm{m}} = \left[{}^{t+\Delta t}\overline{\boldsymbol{\sigma}}_1 \quad {}^{t+\Delta t}\overline{\boldsymbol{\sigma}}_2 \quad \cdots \quad {}^{t+\Delta t}\overline{\boldsymbol{\sigma}}_{n_\phi} \right], \tag{122} $$

$$ {}^{t+\Delta t}\overline{\mathbf{S}}_{\mathrm{b}} = \left[{}^{t+\Delta t}\overline{\mathbf{R}}_1^0 \quad {}^{t+\Delta t}\overline{\mathbf{R}}_2^0 \quad \cdots \quad {}^{t+\Delta t}\overline{\mathbf{R}}_{n_F}^0 \right], \tag{123} $$

$$ {}^{t+\Delta t}\overline{\mathbf{R}}_{\mathrm{b}}^{*} = \begin{Bmatrix} \overline{M}_x^* \left({}^{t+\Delta t}\overline{x}_a, {}^{t+\Delta t}\overline{y}_a \right) \\ \overline{M}_y^* \left({}^{t+\Delta t}\overline{x}_a, {}^{t+\Delta t}\overline{y}_a \right) \\ \overline{M}_{xy}^* \left({}^{t+\Delta t}\overline{x}_a, {}^{t+\Delta t}\overline{y}_a \right) \\ \overline{T}_x^* \left({}^{t+\Delta t}\overline{x}_a, {}^{t+\Delta t}\overline{y}_a \right) \\ \overline{T}_y^* \left({}^{t+\Delta t}\overline{x}_a, {}^{t+\Delta t}\overline{y}_a \right) \end{Bmatrix}, \tag{124} $$

with

$$ {}^{t+\Delta t}\overline{\boldsymbol{\sigma}}_i = \begin{Bmatrix} \overline{\sigma}_{xi} \left({}^{t+\Delta t}\overline{x}_a, {}^{t+\Delta t}\overline{y}_a \right) \\ \overline{\sigma}_{yi} \left({}^{t+\Delta t}\overline{x}_a, {}^{t+\Delta t}\overline{y}_a \right) \\ \overline{\tau}_{xyi} \left({}^{t+\Delta t}\overline{x}_a, {}^{t+\Delta t}\overline{y}_a \right) \end{Bmatrix}, \quad {}^{t+\Delta t}\overline{\mathbf{R}}_1^0 = \begin{Bmatrix} \overline{M}_{xi}^0 \left({}^{t+\Delta t}\overline{x}_a, {}^{t+\Delta t}\overline{y}_a \right) \\ \overline{M}_{yi}^0 \left({}^{t+\Delta t}\overline{x}_a, {}^{t+\Delta t}\overline{y}_a \right) \\ \overline{M}_{xyi}^0 \left({}^{t+\Delta t}\overline{x}_a, {}^{t+\Delta t}\overline{y}_a \right) \\ \overline{T}_{xi}^0 \left({}^{t+\Delta t}\overline{x}_a, {}^{t+\Delta t}\overline{y}_a \right) \\ \overline{T}_{yi}^0 \left({}^{t+\Delta t}\overline{x}_a, {}^{t+\Delta t}\overline{y}_a \right) \end{Bmatrix}. \tag{125} $$

Through above updating scheme, substituting the resultant field in local coordinate system into HSDF method procedures, the stiffness matrix ${}^{t+\Delta t}\overline{\mathbf{K}}^e$ of element HSDF-PSH in local coordinate system can be obtained.

5 | NUMERICAL EXAMPLES

The plate bending and the membrane parts of the new flat shell element HSDF-PSH can pass corresponding constant resultant/stress patch tests. In this section, other nine numerical examples are employed to assess the performance of element HSDF-PSH, including five linear and four geometrically nonlinear tests.

5.1 | Linear examples for shell structures

5.1.1 | Test for plate bending part: Square plate subjected to uniformly distributed load

A square plate subjected to uniformly distributed load $q = 1.0$ is shown in Figure 9(A). This is a classical examination for testing plate bending elements. Here, the new arbitrary polygonal flat shell element HSDF-PSH proposed in this article is used to evaluate its performance of the plate bending part. Due to the biaxial symmetry, only a quarter of the plate is analyzed. And the geometry and material parameters are also given in Figure 9(A). Two BC cases for all boundaries are considered: (i) the hard simply supported (SS2) BC ($w = \psi_s = 0$) and (ii) the clamped BC ($w = \psi_n = \psi_s = 0$). And three thickness-span ratio cases $h/L = 0.001, 0.01, 0.1$ are calculated. First, four regular 2×2, 4×4, 8×8, 16×16 square meshes shown in Figure 9(B), denoted by A1, A2, A3, and A4, respectively, are employed to investigate element convergence. As a special case of arbitrary polygonal element, element HSDF-PSH with four edges, HSDF-PSH4 (4-node quadrilateral element), is used in these meshes, and its results are compared with those obtained by the 4-node quadrilateral shell elements S4 and S4R in Abaqus.[64] Second, four polygonal meshes, as shown in Figure 9(C), are also adopted. These polygonal meshes are denoted by Mesh B1, B2, B3, and B4, respectively.

The normalized results of the deflections at the central point c of the plate are presented in Tables 6 and 7. The results obtained by other polygonal elements, including DKMT-ngon[20] and PRMn-PL,[4] are also given in Table 7 for comparison. And their meshes are denoted by C1–C4 (for DKMT-ngon), and D1–D4 (for PRMn-PL), respectively. It can be seen that, for quadrilateral elements, the precision of HSDF-PSH4 is better than S4 and S4R; and for polygonal elements, HSDF-PSH also performs much better than the other two polygonal plate elements. The results show that HSDF-PSH possessed high accuracy and good convergence, it can obtain quite good results even in very coarse meshes, while the other two polygonal elements cannot do.

5.1.2 | Test for membrane part: Pure bending test

A simply supported beam under pure bending state is shown in Figure 10(A), and the geometries and material parameters are also given. Exact solutions can be obtained from the beam theory for the vertical displacement, the lateral displacement, and the end rotation. This example is usually used to test plane quadrilateral elements. Here, the meshes for the new polygonal element HSDF-PSH, denoted by A1, A2, A3, and A4, respectively, are given in Figure 10(B). For comparisons, those results obtained by Abaqus elements with Meshes A1 (for S4 and S4R,[64] respectively) and B1 (for S3[64] and S4, simultaneously) are also calculated, in which Mesh B1 is a refined version of Mesh A4. In order to show the convergence of element HSDF-PSH, the results using a new mesh B2 for HSDF-PSH are also considered, which is extended from Mesh B1.

The results are listed in Table 8. It can be seen that, the Abaqus shell elements S3 and S4 exhibit locking problem, while S4R without hourglass control suffers from hourglass phenomenon. And the results obtained by S4R with hourglass control (denoted by S4R[enhanced]) still stay away from the reference solutions. However, element HSDF-PSH can produce much better results, no matter which mesh is used.

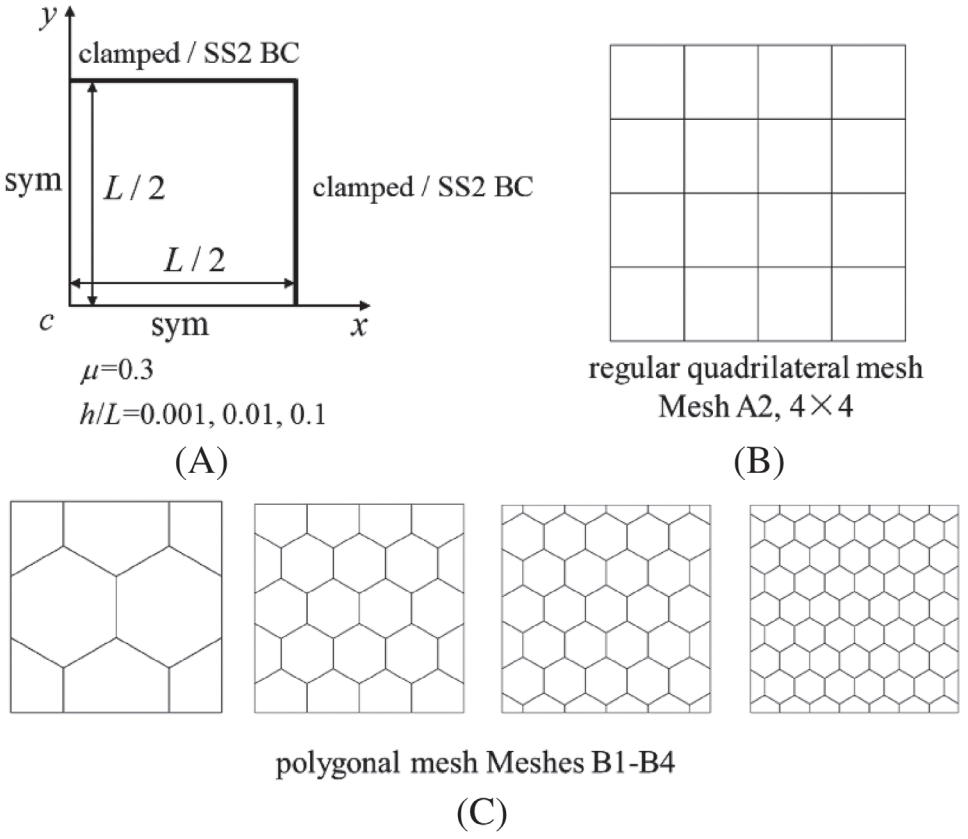

FIGURE 9 Square plate subjected to uniformly distributed load, geometry, and meshes

TABLE 6 Normalized results of square plate with regular square meshes

Mesh type	A1	A2	A3	A4	Reference [$w_c/(qL^4/100D)$]
SS2, $h/L = 0.001$					
S4	0.9771	0.9948	0.9988	0.9998	1.0000 (0.4062)
S4R	1.0123	1.0032	1.0007	1.0002	
HSDF-PSH4	0.9975	1.0000	1.0000	1.0000	
SS2, $h/L = 0.01$					
S4	0.9771	0.9951	0.9988	0.9998	1.0000 (0.4064)
S4R	1.0123	1.0032	1.0007	1.0002	
HSDF-PSH4	0.9975	1.0000	1.0000	1.0000	
SS2, $h/L = 0.1$					
S4	0.9822	0.9960	0.9991	0.9998	1.0000 (0.4273)
S4R	1.0157	1.0037	1.0009	1.0002	
HSDF-PSH4	0.9981	0.9984	0.9993	0.9998	
Clamped, $h/L = 0.001$					
S4	0.9573	0.9889	0.9976	0.9992	1.0000 (0.1265)
S4R	1.0237	1.0040	1.0016	1.0008	
HSDF-PSH4	0.9794	0.9960	1.0000	1.0000	
Clamped, $h/L = 0.01$					
S4	0.9582	0.9890	0.9976	1.0000	1.0000 (0.1267)
S4R	1.0245	1.0047	1.0016	1.0008	
HSDF-PSH4	0.9803	0.9968	1.0000	1.0008	
Clamped, $h/L = 0.1$					
S4	0.9620	0.9953	1.0020	1.0033	1.0000 (0.1499)
S4R	1.0133	1.0073	1.0047	1.0040	
HSDF-PSH4	1.0033	1.0053	1.0040	1.0040	

5.1.3 | Test for membrane part: Cook's skew beam

A skew cantilever beam subjected to a distributed shear load $P = 1.0$ at the free edge is shown in Figure 11. Four polygonal meshes shown in Figure 11, denoted by A1, A2, A3, and A4, are employed for element HSDF-PSH, in which those nodes connecting two collinear element edges are marked. It can be seen that the element shapes in each mesh is quite free, even severely distorted element exists. In order to compare the results with those obtained by triangular shell element S3 and quadrilateral shell element S4 in Abaqus, the elements in above meshes are subdivided into triangle or quadrilateral without changing the total number of element nodes. Furthermore, four regular quadrilateral meshes with 2×2, 4×4, 8×8, 12×12 elements, denoted by B1, B2, B3, and B4, are also used for HSDF-PSH4 and S4 elements.

The normalized results of vertical displacement v_A at the node A is listed in Table 9 and plotted in Figure 12. The results indicate that HSDF-PSH can produce good results with much free element shapes.

5.1.4 | Pinched cylinder

A pinched cylinder with end diaphragms is subjected to a pair of opposite concentrated forces in the mid-span, as shown in Figure 13. Only one-eighth structure is considered due to symmetry, and the geometry and

TABLE 7 Results of square plate with polygonal meshes

Element	Mesh type/Number of nodes Deflection				Reference $[w_c/(qL^4/100D)]$
SS2, $h/L = 0.001$					
DKMT-ngon[20]	C1/104	**C2/204**	**C3/404**	**C4/602**	1.0000 (0.4062)
	0.9879	0.9825	0.9956	0.9951	
PRMn-PL[4]	D1/80	**D2/190**	**D3/496**	**D4/1396**	
	1.0183	1.0066	1.0027	1.0009	
HSDF-PSH	B1/18	**B2/46**	**B3/80**	**B4/136**	
	0.9970	0.9988	0.9995	0.9998	
SS2, $h/L = 0.01$					
DKMT-ngon	C1/104	**C2/204**	**C3/404**	**C4/602**	1.0000 (0.4064)
	0.9875	0.9820	0.9951	0.9946	
HSDF-PSH	B1/18	**B2/46**	**B3/80**	**B4/136**	
	0.9970	0.9990	0.9998	1.0000	
SS2, $h/L = 0.1$					
DKMT-ngon	C1/104	**C2/204**	**C3/404**	**C4/602**	1.0000 (0.4273)
	0.9827	0.9806	0.9949	0.9946	
clamped, $h/L = 0.001$					
DKMT-ngon	C1/104	**C2/204**	**C3/404**	**C4/602**	1.0000 (0.1265)
	1.0427	1.0055	1.0087	1.0024	
HSDF-PSH	B1/18	**B2/46**	**B3/80**	**B4/136**	
	0.9968	0.9984	0.9992	1.0000	
clamped, $h/L = 0.01$					
DKMT-ngon	C1/104	**C2/204**	**C3/404**	**C4/602**	1.0000 (0.1267)
	1.0418	1.0047	1.0079	1.0024	
HSDF-PSH	B1/18	B2/46	B3/80	B4/136	
	0.9968	0.9992	1.0000	1.0000	
clamped, $h/L = 0.1$					
DKMT-ngon	C1/104	**C2/204**	**C3/404**	**C4/602**	1.0000 (0.1499)
	1.0227	0.9987	1.0080	1.0040	
HSDF-PSH	B1/18	**B2/46**	**B3/80**	**B4/136**	
	1.0067	1.0053	1.0040	1.0047	
PRMn-PL	D1/80	**D2/190**	**D3/496**	**D4/1396**	
	1.0072	1.0029	1.0009	1.0003	
HSDF-PSH	B1/18	**B2/46**	**B3/80**	**B4/136**	
	0.9991	0.9995	0.9998	1.0000	

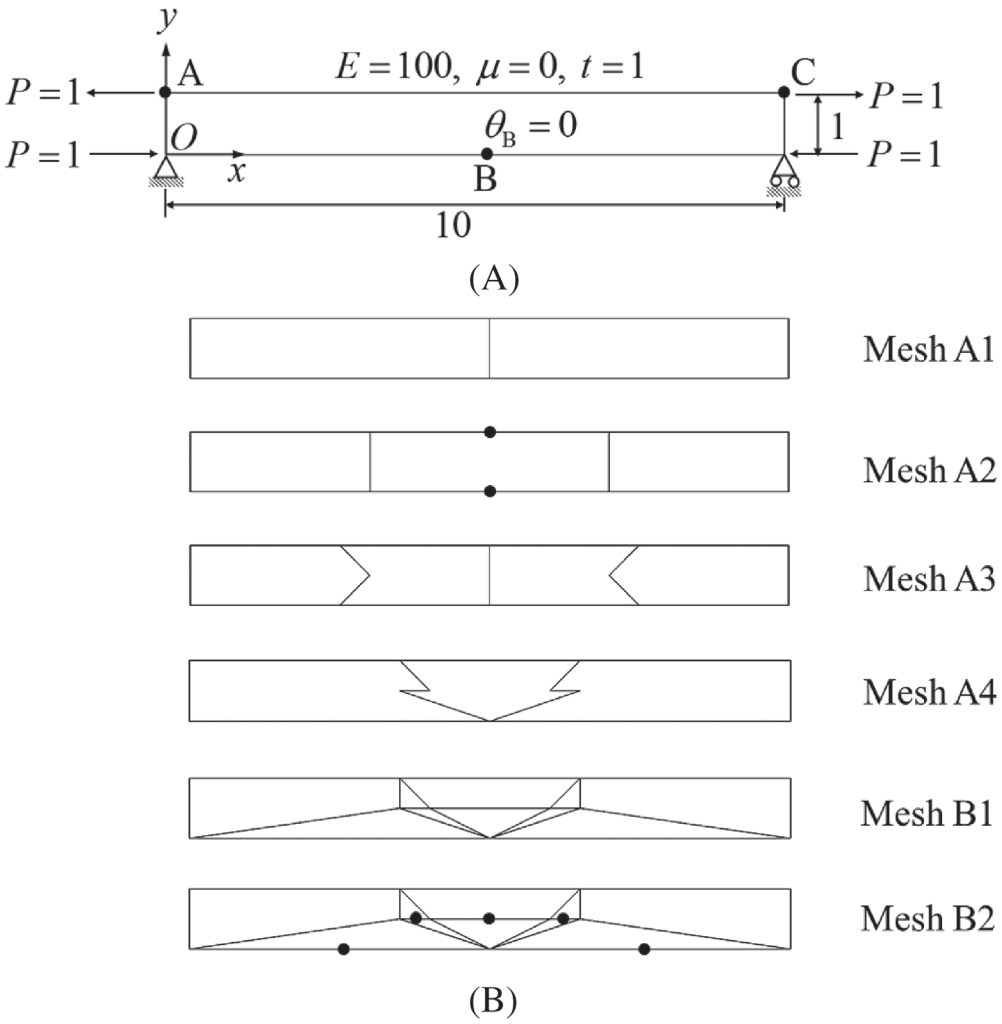

FIGURE 10 Pure bending test, geometry, and meshes

TABLE 8 Results of displacements and rotations for pure bending test

Element	Mesh	u_A	v_B	θ_C
S4	A1	−0.376	0.926	−0.280
S4R	A1	−1.067	2.630	−0.796
S4R (enhanced)	A1	−0.396	0.977	−0.296
S3 and S4	B1	−0.046	0.057	−0.031
HSDF-PSH	A1	−0.600	1.500	−0.600
	A2	−0.600	1.500	−0.600
	A3	−0.600	1.499	−0.602
	A4	−0.597	1.491	−0.598
	B1	−0.369	0.933	−0.378
	B2	−0.464	1.288	−0.492
Exact		−0.600	1.500	−0.600

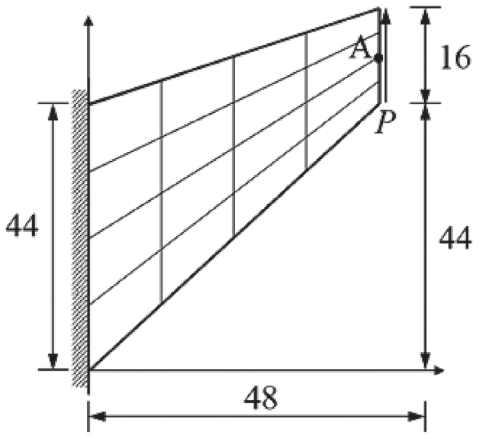

E=1.0
μ=1/3
t=1.0

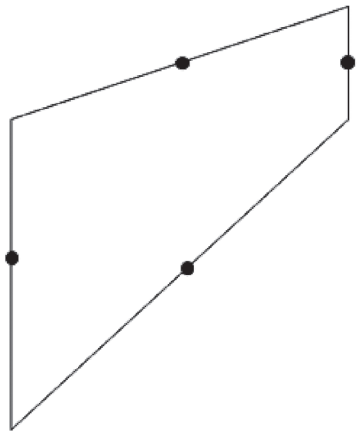

Mesh A1

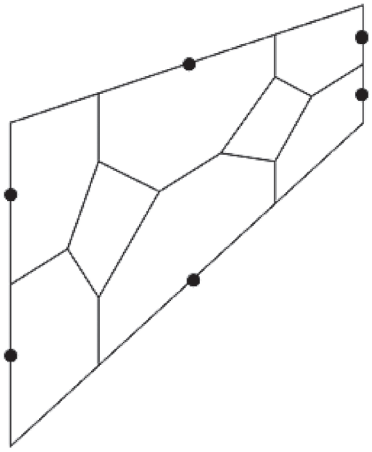

Mesh A2

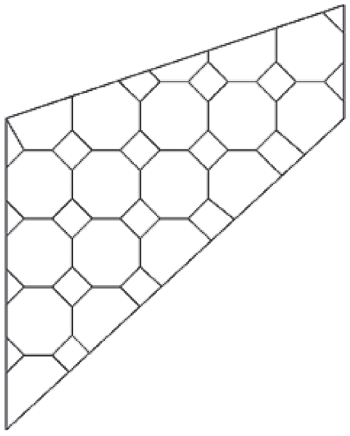

Mesh A3

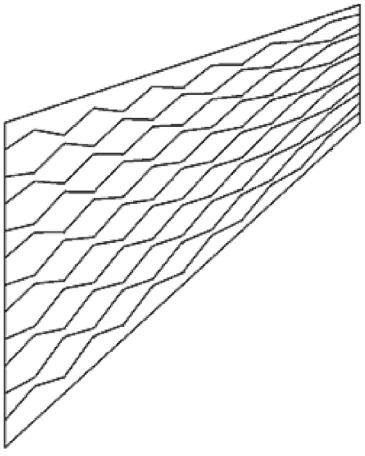

Mesh A4

FIGURE 11 Cook's skew beam, geometry, material, and mesh

TABLE 9 Results of Cook's skew beam

Mesh type	A1	A2	A3	A4
Total number of nodes	8	24	75	169
HSDF-PSH	0.977	0.981	0.987	0.996
S3 and S4	0.438	0.776	0.952	0.977
Mesh type	*B*1	*B*2	*B*3	*B*4
Total number of nodes	9	25	81	169
HSDF-PSH4	0.967	0.975	0.991	0.995
S4	0.864	0.959	0.987	0.993
FSSQ[66]	0.983	0.979	0.993	0.998
NMS-4F[67]	0.898	0.958	0.983	–
Reference	$v_A = 23.96$[68]			

FIGURE 12 Convergence result of Cook's skew beam

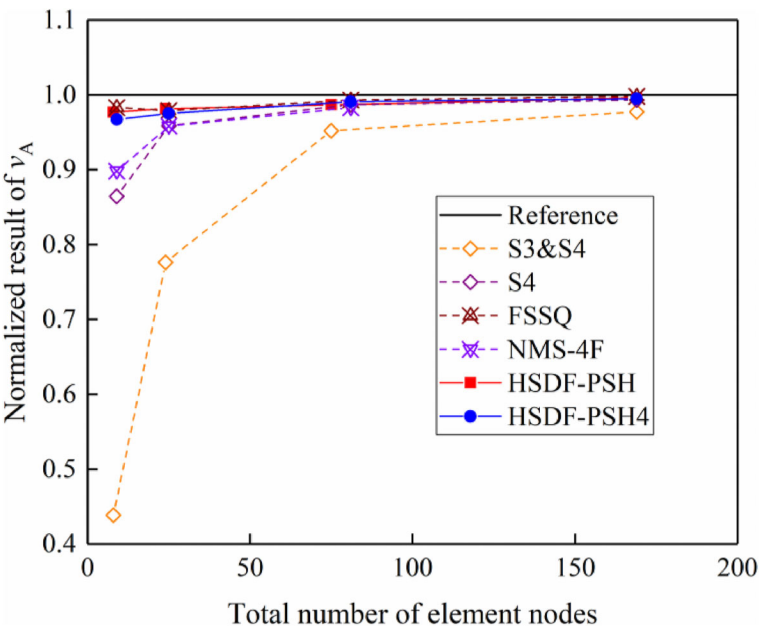

the material parameters are also given in Figure 13. First, different quadrilateral meshes are designed for HSDF-PSH, including 4-node quadrilateral and 6-node degenerated quadrilateral elements, as shown in Figure 14(A), denoted by A1, A2, A3, and A4. In the same mesh type, the total element node numbers of 4- and 6-node elements are the same, with two neighbored 4-node elements degenerating into a 6-node one. Second, four regular hexagon meshes shown in Figure 14(B) are considered, denoted by H1, H2, H3, and H4, respectively.

The vertical displacement of Node A, v_A, is calculated. The normalized results obtained by different quadrilateral elements (including the 6-node degenerated quadrilateral element) are listed in Table 10. And the corresponding convergence rates are plotted in Figure 15(A). For the hexagonal meshes, the hexagonal flat elements will be warped, which may influence the precision. The relative errors of v_A obtained by meshes H1, H2, H3, and H4 are plotted in Figure 15(B). Furthermore, the results obtained by shell element PSE-Poly[22] with similar meshes are also plotted for comparison. It can be seen that element HSDF-PSH can obtain very stable and precise results with various element sides. Compared with the other element listed here, HSDF-PSH shows obvious advantages. Even though the element is distorted or warped, the arbitrary element still keeps good performance.

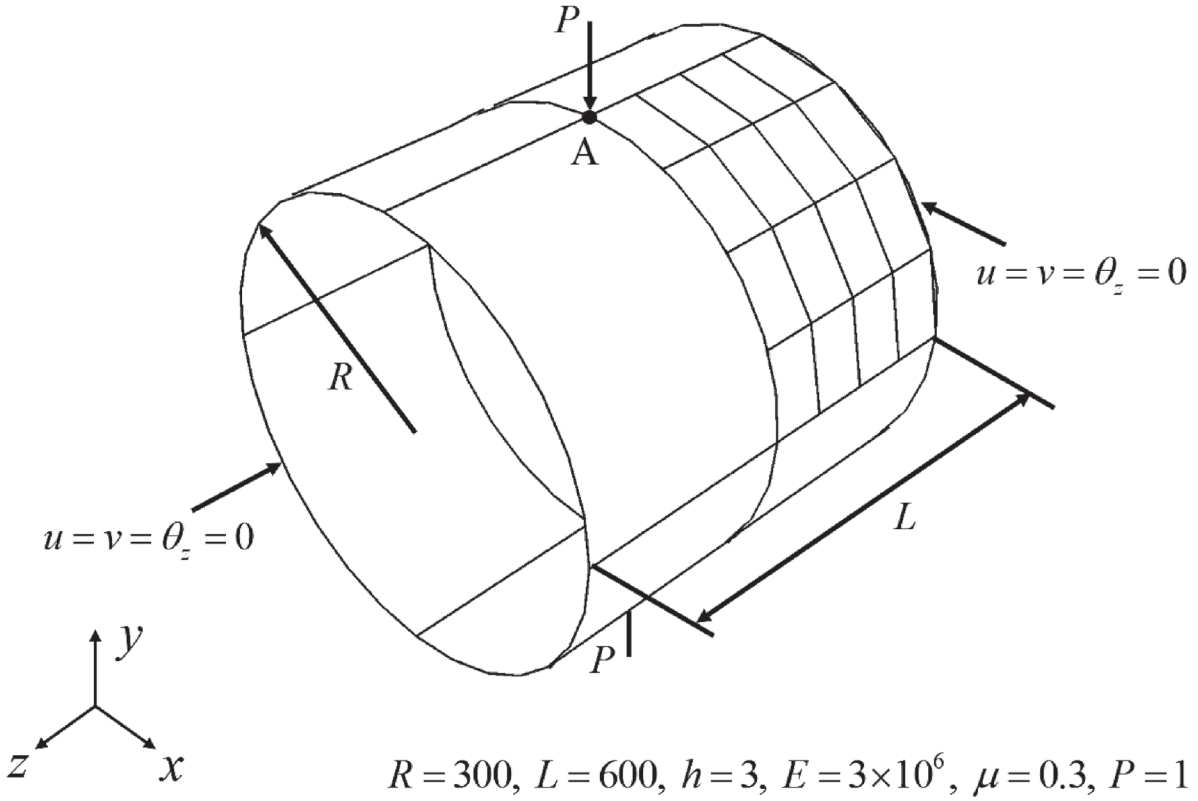

FIGURE 13 Pinched cylinder, geometry, material, and constraint

5.1.5 | Cylindrical structure subjected to discretely distributed load

This problem is a simplified model for practical engineering. Due to symmetry, only a quarter of the cylindrical structure is considered, as shown in Figure 16(A). The structure is subjected to discretely distributed vertical load q, and the loading regions are the shadow parts plotted in Figure 16(A). For this complex loading case, it is very convenient to mesh the structure with the arbitrary polygonal element HSDF-PSH. Figure 16(B,C) are two typical coarse mesh types. For comparison, the results obtained by Abaqus shell elements S3, S4, and S4R with Abaqus's automeshing technology are also given.

The results of the vertical displacement v_A at the node A are listed in Table 11, and the convergence curves are plotted in Figure 17. Here, the new polygonal element HSDF-PSH exhibits its flexibility and good performance. It can produce better results with coarse and irregular meshes.

5.2 | Geometric nonlinear problems for shell structures

5.2.1 | Angle frame

An angle frame with one end clamped is shown in Figure 18(A), and the other end of the frame is subjected to a shear load F. The membrane part of the flat shell will play the leading role in this test. Three meshes are given in Figure 18, in which mesh (b) contains seven rectangular elements, mesh (c) contains 19 hexagonal elements, and mesh (d) is a refined version of mesh (c) and contains 38 quadrilateral elements. Mesh (b) is designed for elements HSDF-PSH4, S4 and S4R, while mesh (c) for HSDF-PSH6, and mesh (d) for S4 and S4R. The results of 8-node quadrilateral element S8R with a fine mesh (304 elements) are taken as reference solutions. The load–displacement curves of the load F with the horizontal displacement u_A at the node A are shown in Figure 19. It can be seen that, the new element HSDF-PSH can present the best solutions in this problem. For the quadrilateral mesh given in Figure 18(B), HSDF-PSH4 is much more precise than

FIGURE 14 Pinched cylinder, mesh types

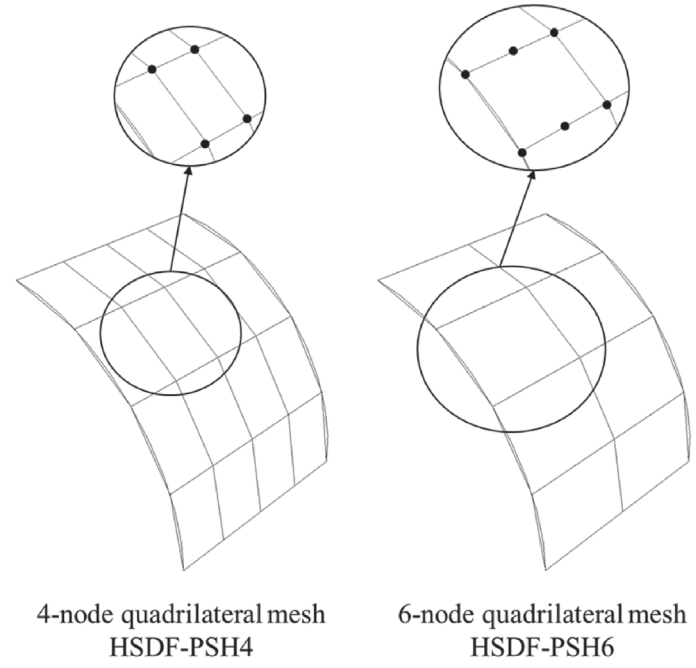

(A)

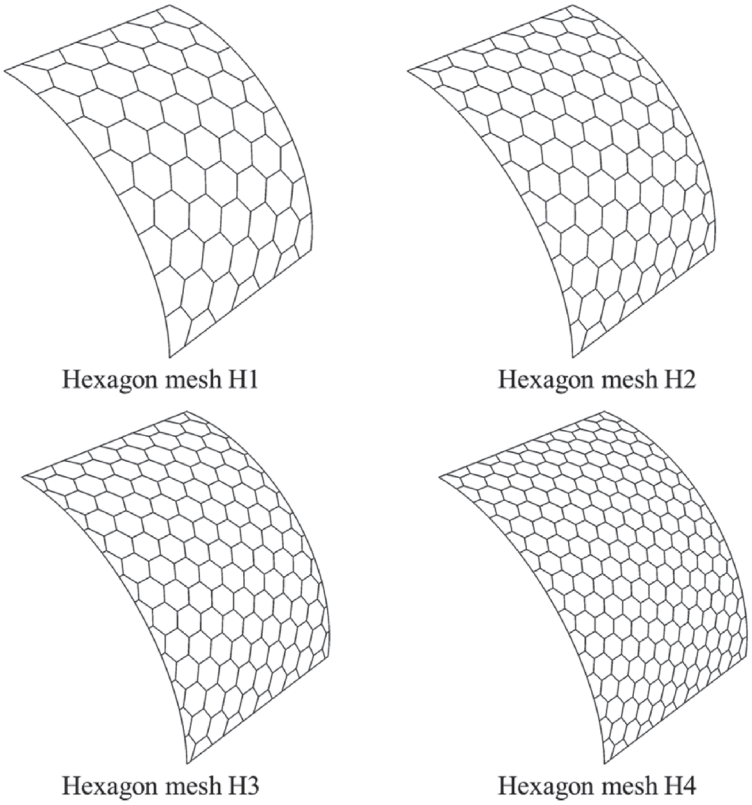

(B)

TABLE 10 Normalized results of pinched cylinder

Mesh type	Mesh A1	Mesh A2	Mesh A3	Mesh A4
Number of nodes	**25**	**81**	**289**	**625**
S4	0.3882	0.7543	0.9328	0.9743
S4R	0.4743	0.8049	0.9543	0.9860
QCS1	0.6090	0.9255	1.0131	
QFSUQ	0.6230	0.9180	0.9960	
MIST1	0.4705	0.8016	0.9482	0.9794
FSSQ	0.5651	0.9107	0.9973	
MISQ24	0.6416	0.9411	1.0018	
XSHELL41	0.6250	0.9180	0.9920	
MIN4T	0.5074	0.8405	0.9624	0.9958
HDF-PSH4	0.6286	0.9184	0.9916	1.0023
HDF-PSH6	0.6658	0.9544	1.0083	1.0117
	$v_A = 1.8248 \times 10^{-569}$			

FIGURE 15 Convergence plot of pinched cylinder

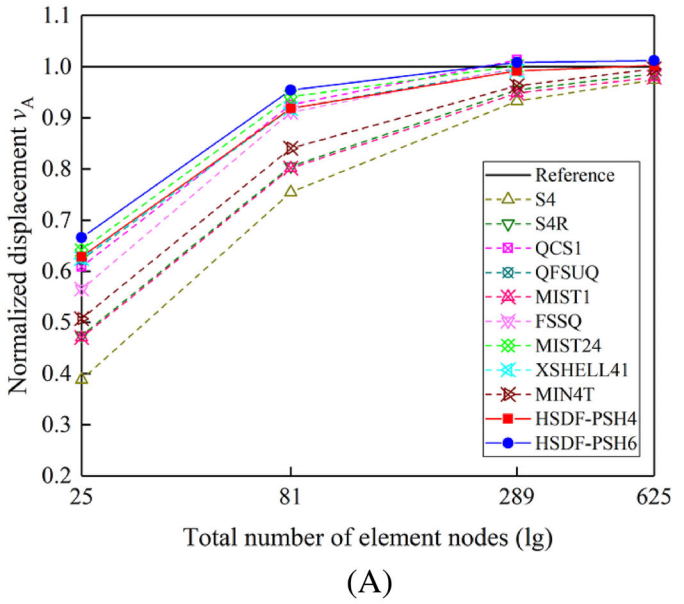

(A)

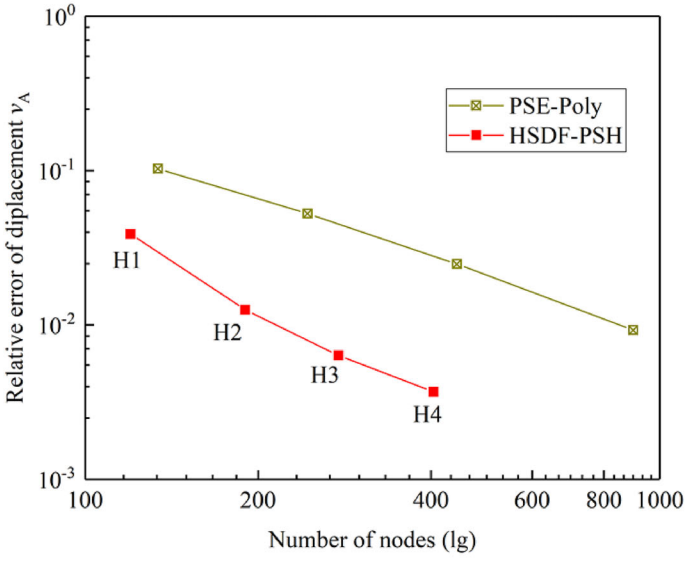

(B)

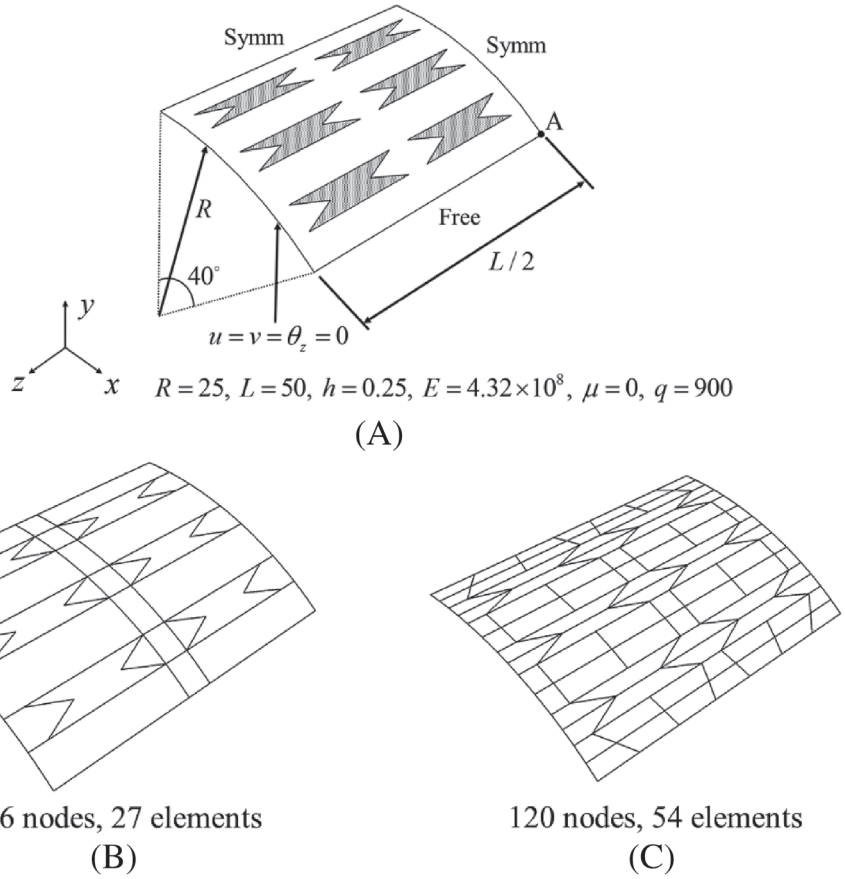

FIGURE 16 Cylindrical structure subjected to discretely distributed load, geometry, and mesh

TABLE 11 Results of cylindrical structure

Nodes	Elements	S3 and S4	Nodes	Elements	S4	S4R
76	89	−0.55409	92	82	−0.55351	−0.58413
198	207	−0.56943	144	126	−0.56068	−0.57649
541	518	−0.57106	666	623	−0.57088	−0.57321
1991	1947	−0.57072	2113	2027	−0.57074	−0.57158
5299	5238	−0.57088	5437	5295	−0.57090	−0.57116
Nodes	Elements	*S*3	Nodes	Elements	HSDF-PSH	
80	138	−0.42336	56	27	−0.55984	
183	320	−0.52658	120	54	−0.56782	
652	1208	−0.56143	666	623	−0.56986	
2734	5252	−0.56808	1991	1947	−0.57179	
4848	9412	−0.56912	5437	5295	−0.57075	

S4 and S4R. And for the hexagonal mesh given in Figure 18(C), the results of element HSDF-PSH6 also agree well with the reference solutions, while elements S4 and S4R cannot reach the equal precision even the refined mesh (d) is used.

5.2.2 | Cantilever beam subjected to end moment

As shown in Figure 20, a slender cantilever beam is subjected a moment at free end. This is a classical test of geometrically nonlinear analyses. Five different meshes are adopted and given in Figure 20(B), where Mesh A and Mesh B are made of regular and distorted quadrilateral elements with different nodes, respectively.

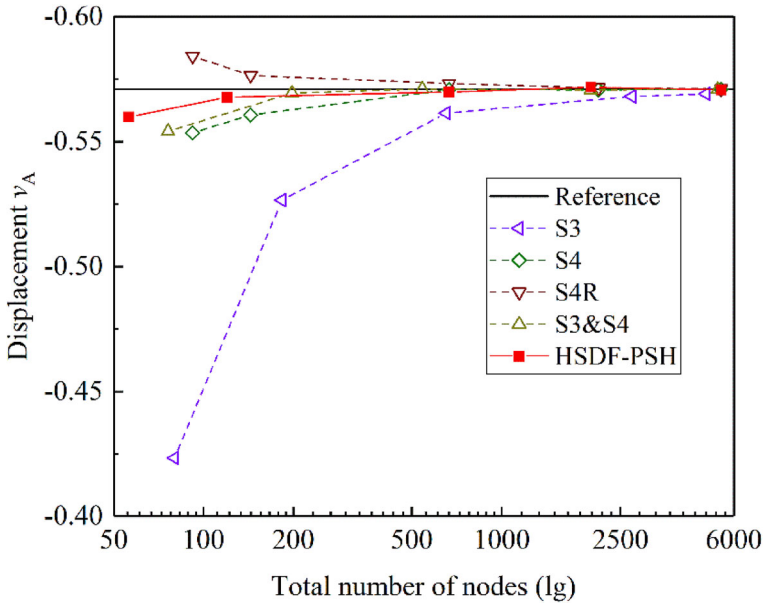

FIGURE 17 Convergence plot of cylindrical structure

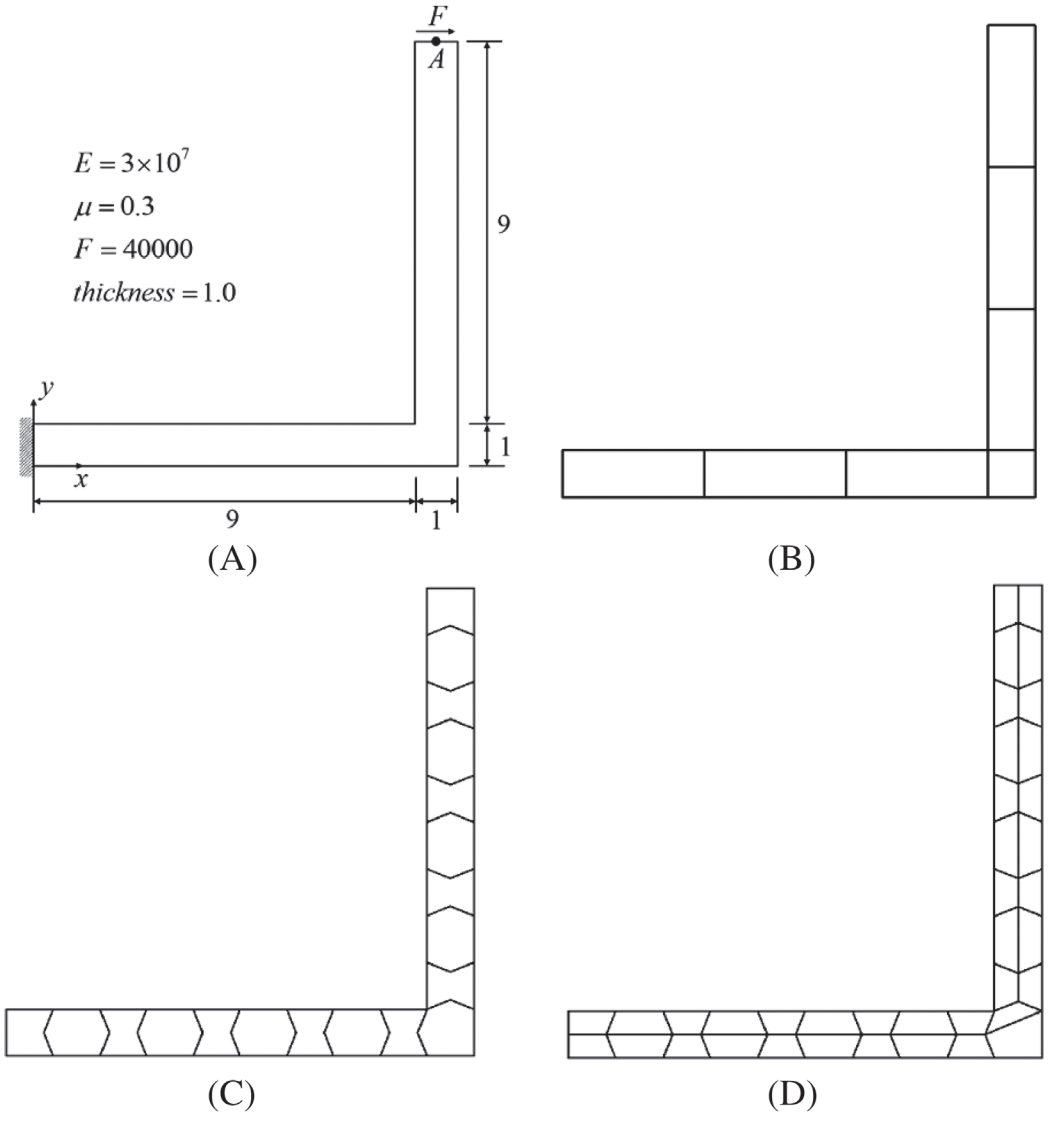

FIGURE 18 Angle frame, geometry, and mesh

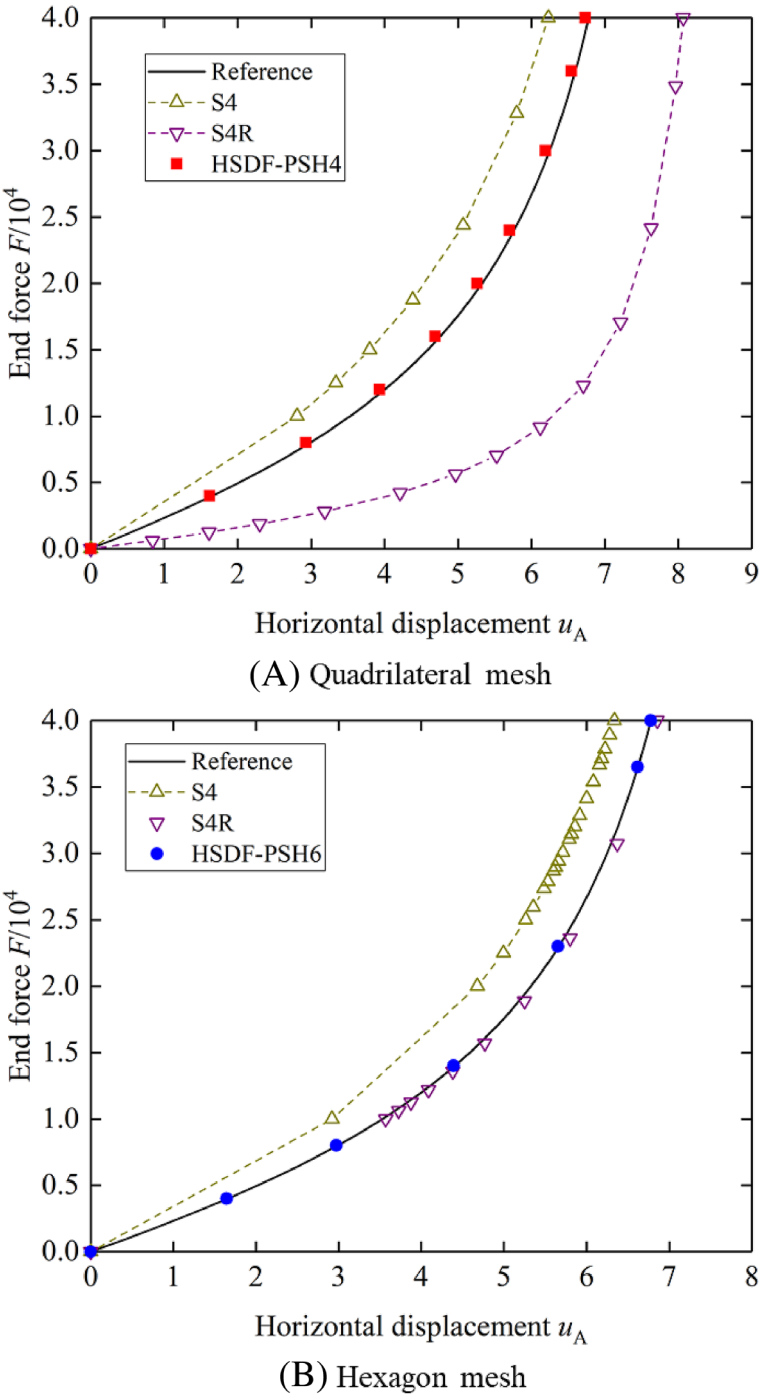

FIGURE 19 Load–displacement curves for angle frame

The results of tip displacements u_{tip} along x-axis and w_{tip} along z-axis are considered. For all element and mesh types, Abaqus nonlinear solver is utilized with initial, minimum and maximum increment sizes 0.1, 10^{-5}, and 1.0, respectively. In this condition, elements S4, S4R, and S8R cannot provide convergence results even using regular Mesh A. However, the polygonal element HSDF-PSH can completely finish the whole calculation, no matter which shape is used. The convergence results are listed in Table 12, in which NINC represents the total number of increment steps, NITER represents the total number of iteration steps and the total time is set to 1.0. Furthermore, Sze et al.[70] used S4R to calculate this problem as well, and their data are also given in Table 12 for comparison. The final deformation diagrams obtained by HSDF-PSH are given in Figure 21. And related load–displacement curves are plotted in Figure 22. It can be seen that the new shell element HSDF-PSH shows the best convergence and precision in this problem.

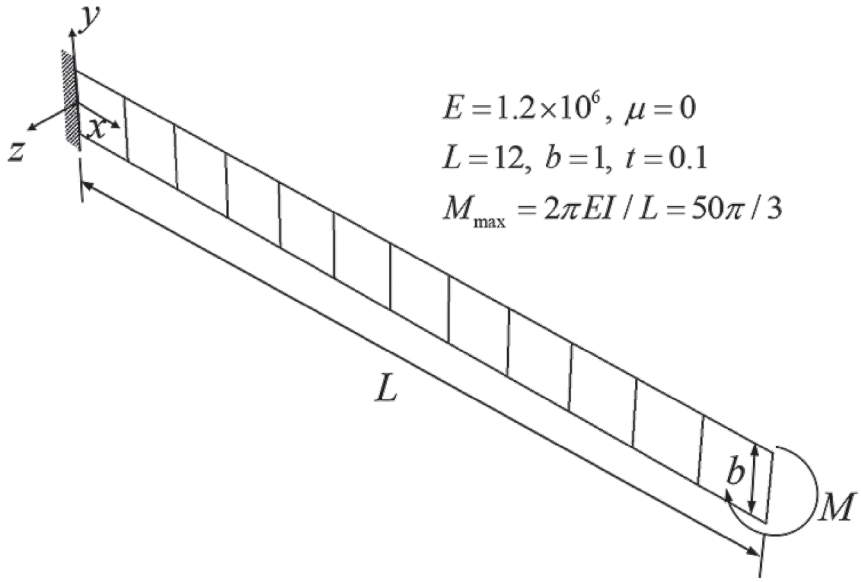

(A)

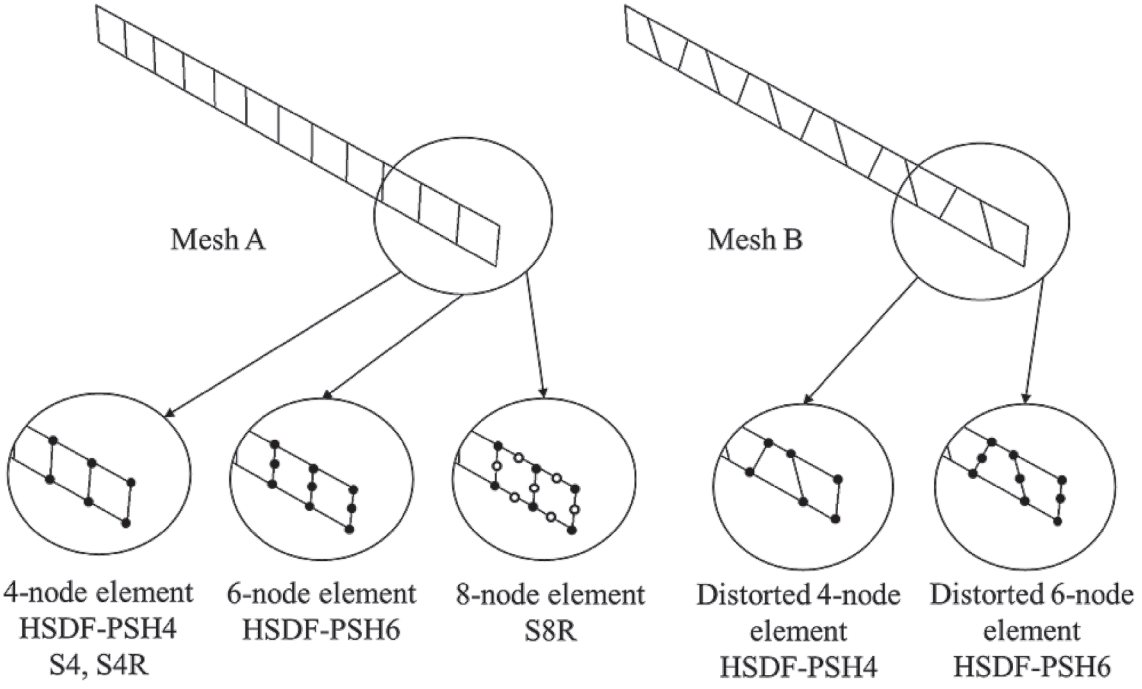

(B)

FIGURE 20 Cantilever beam subjected to end moment, geometry, mesh

5.2.3 | Pullout of an open-ended cylindrical shell

As shown in Figure 23, an open-ended cylindrical shell is subjected to a pair of opposite concentrated forces in the mid-span. Due to symmetry, only one-eighth of the shell is considered. In this problem, the structure deforms severely, and elements with too many edges are not suitable because of element warping. Therefore, the new element HSDF-PSH with triangular and quadrilateral shapes, HSDF-PSH3 and HSDF-PSH4 are utilized together with Abaqus element S3, S4, S4R. Figure 23(B,C) are the 4×6 and 8×12 meshes for calculation. For HSDF-PSH4, 8×12 distorted mesh given Figure 23(D) is also used.

TABLE 12 Convergence results of cantilever beam

Element	Mesh	NINC	NITER	Total time
HSDF-PSH4	12 × 1, regular	10	71	1.000
	12 × 1, distorted	32	162	1.000
HSDF-PSH6	12 × 1, regular	20	105	1.000
	12 × 1, distorted	29	172	1.000
S4	12 × 1, regular	78	567	0.827
S4R	12 × 1, regular	30	206	0.340
S8R	12 × 1, regular	116	916	0.994
S4R(Sze)[69]	8 × 1, regular	125	715	1.000
	16 × 1, regular	125	714	1.000

FIGURE 21 Deformation diagram of cantilever beam

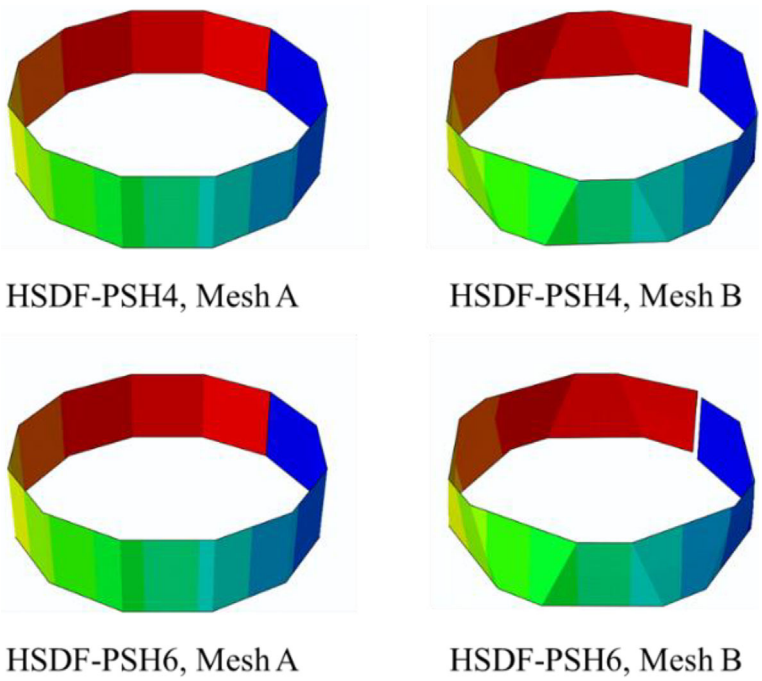

FIGURE 22 Load–displacement curve of cantilever beam subjected to end moment

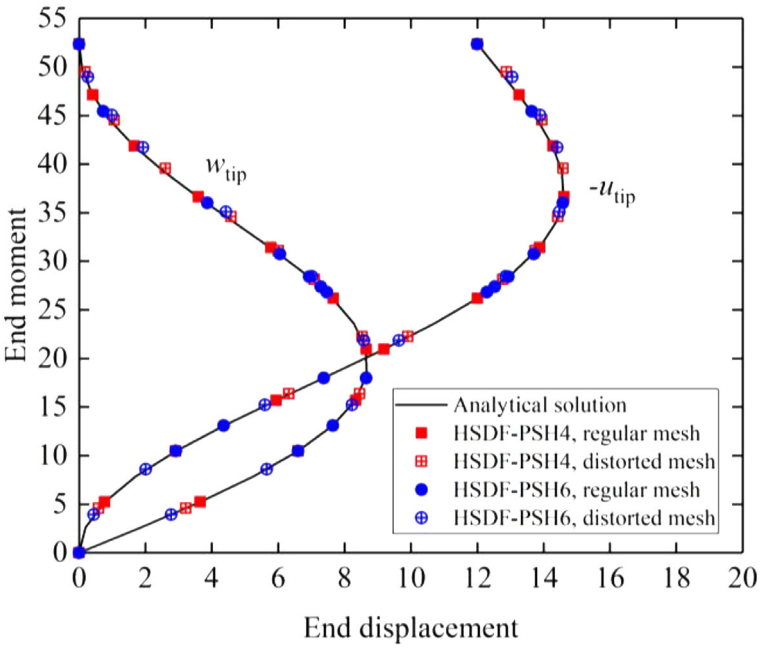

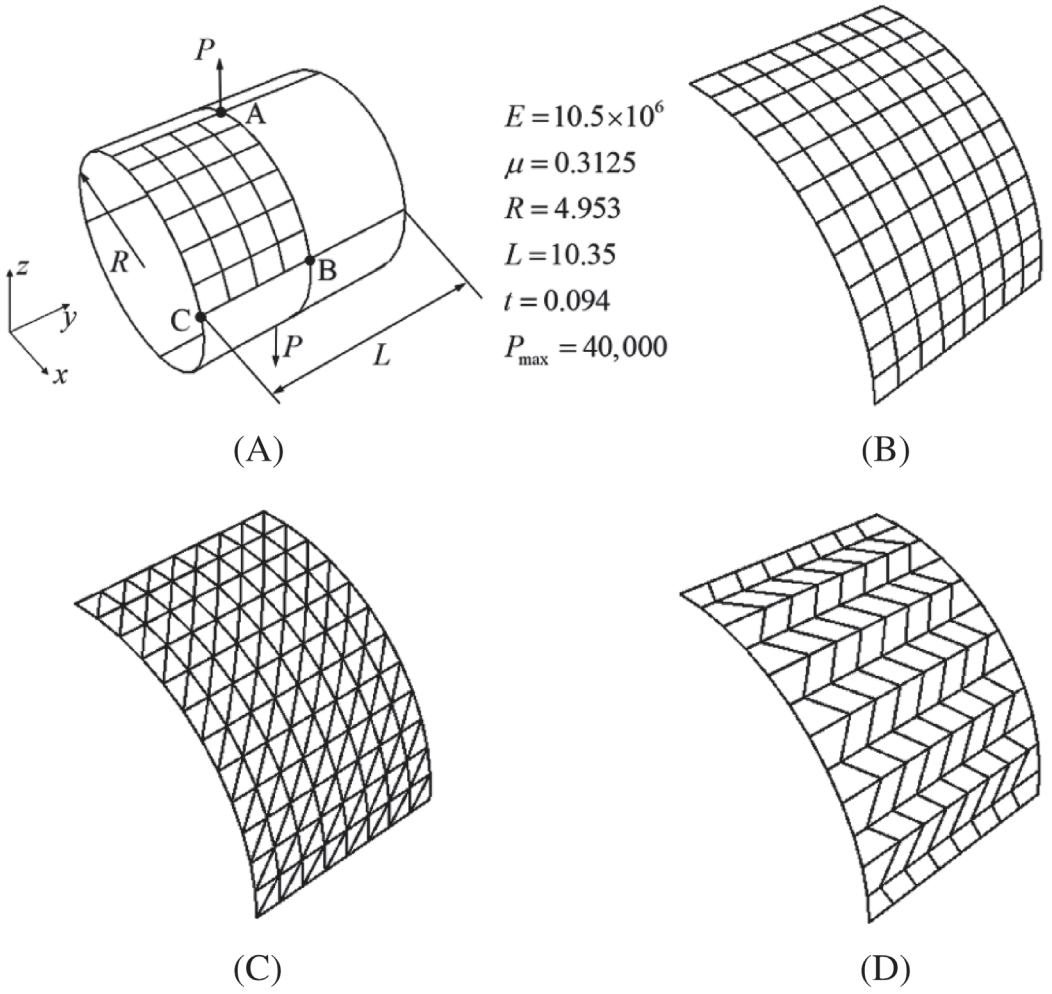

FIGURE 23 Pullout of an open-ended cylindrical shell, geometry, and mesh

TABLE 13 Relative errors of open-ended cylindrical shell

	Relative error		
Element	w_A	u_B	u_C
4 × 6 mesh			
HSDF-PSH3	−4.21%	−4.02%	8.99%
HSDF-PSH4	0.75%	0.29%	1.72%
S3	−9.41%	−8.37%	15.48%
S4	−6.67%	−5.13%	9.28%
S4R	Aborted		
8 × 12 mesh			
HSDF-PSH3	−2.17%	−0.77%	1.61%
HSDF-PSH4	0.01%	0.15%	0.28%
HSDF-PSH4 (distorted)	1.02%	1.18%	0.74%
S3	−4.79%	−2.55%	5.94%
S4	−2.80%	−1.04%	1.16%
S4R	−0.71%	−0.28%	−3.16%
Reference	$w_A = 2.768$, $u_B = -4.551$, $u_C = -3.269$		

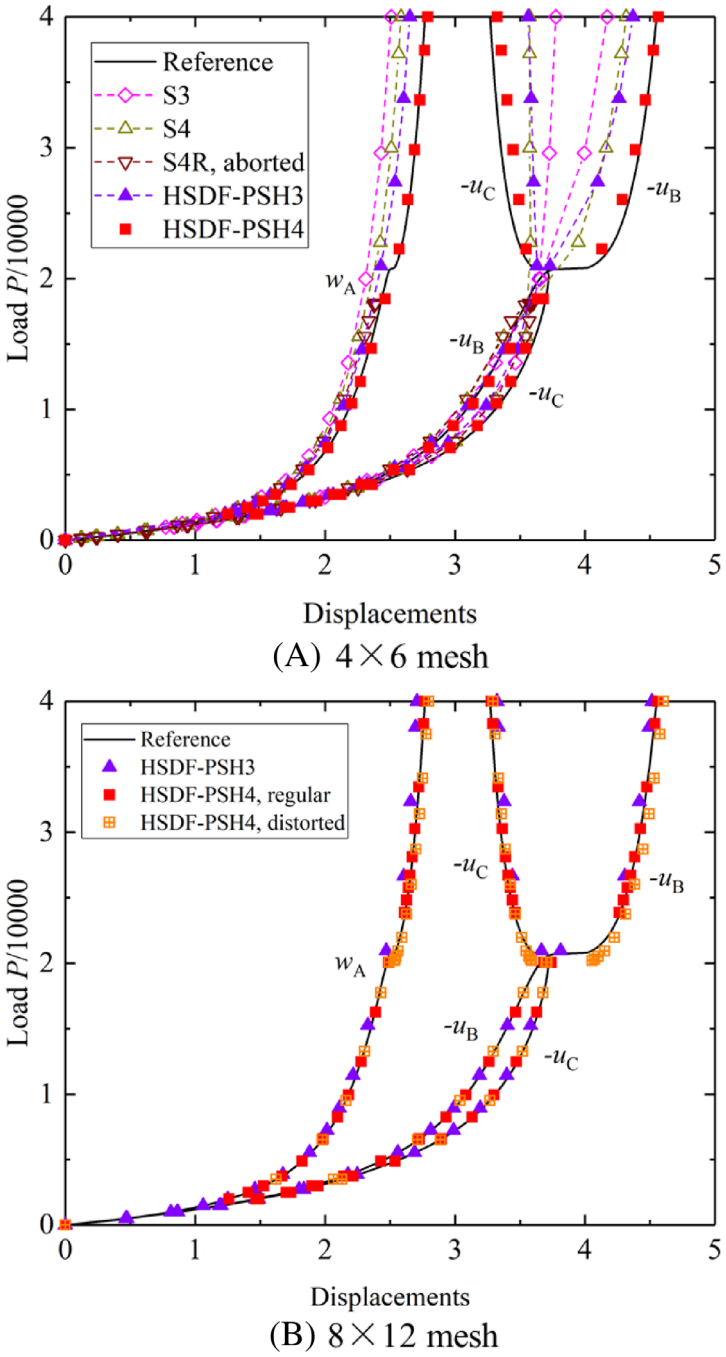

FIGURE 24 Load–displacement curves of open-ended cylindrical shell

Results of element S4R with 24 × 36 regular mesh are taken as the reference solutions. The relative errors of the displacements at node A, B, and C under the max load P_{max} are listed in Table 13. It should be noted that the 4 × 6 mesh is a very coarse mesh for this problem, so that elements S3 and S4 present obvious errors, and S4R even aborts without final results. However, the new element HSDF-PSH4 can still provide good results in this rigorous condition. Although the precision of HSDF-PSH3 is not as good as HSDF-PSH4, it is still better than S3 and S4. This feature can also be seen in Figure 24. When the refined 8 × 12 mesh is used, both HSDF-PSH3 and HSDF-PSH4 exhibit good precision. Furthermore, HSDF-PSH4 even keeps good precision in distorted mesh (d).

5.2.4 | Hinged cylindrical shell under concentrated load

A cylindrical shell under concentrated load P is shown in Figure 25(A). A pair of opposite sides is hinged and the other pair is free. Due to symmetry, a quarter of the shell is considered. For this example, References 71, 72

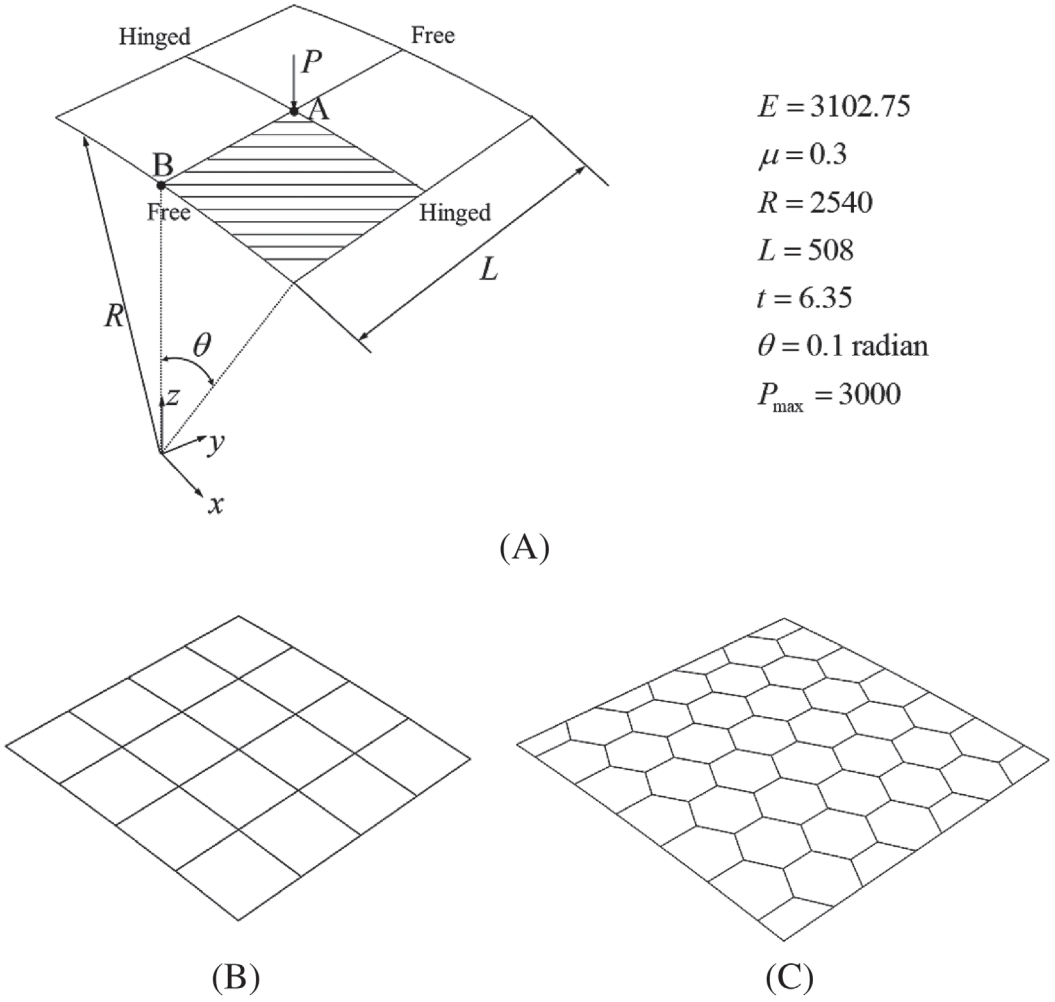

FIGURE 25 Hinged cylindrical shell under concentrated load, geometry, and mesh

proposed two cases with different thickness. Here, only the thin shell case is analyzed because it is a more challenging one with obvious postbucking behavior. The Risks method[73] is employed for the postbucking geometrically nonlinear analysis. The initial increment size is set to 0.05; the maximum arc length increment is 0.1; and the maximum valve of the load proportionality factor is 1. Regular quadrilateral mesh shown in Figure 25(B) is adopted for HSDF-PSH4, S4 and S4R, while polygonal mesh given in Figure 25(C) is for HSDF-PSH. Take the results of S4 with 64×64 regular quadrilateral mesh as reference solutions. The deflections at points A and B are calculated, denoted by w_A and w_B. The corresponding load–displacement curves are plotted in Figure 26. For the quadrilateral mesh, although the mesh is coarse, the result of HSDF-PSH4 are still agree well with the reference solution. For the polygonal mesh, it can be seen that the polygonal element HSDF-PSH possessed high precision and can capture the postbucking behavior.

6 | CONCLUSIONS

In this article, an arbitrary polygonal HSDF flat shell finite element method for analyses of linear and geometrically nonlinear shell structures is proposed. For linear formulations, two recent advanced FEMs with analytical trail functions are employed to formulated the new element, in which the bending part of the element is constructed by the HDF element method for Mindlin–Reissner plate,[32-38] and the membrane part with drilling DOF is formulated by the HSF element method.[32,39-44] Through a best-fit analytical trial functions selection scheme for different number of element edges, the final linear element formulations can be obtained. Then, the linear flat shell element is generalized to

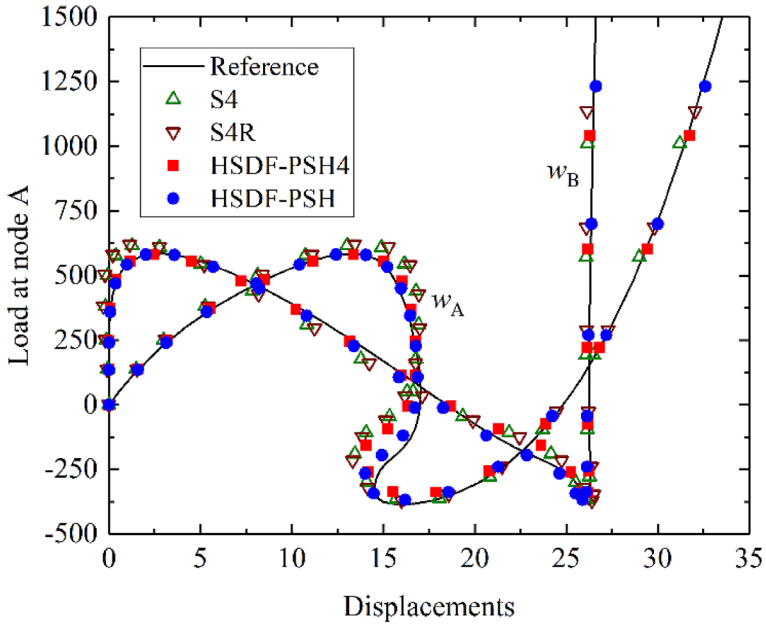

FIGURE 26 Load–displacement curves of hinged cylindrical shell

geometrically nonlinear applications by employing the CR method, in which a best-fit corotated frame for polygonal elements is defined to achieve the best accuracy. By updating the analytical trial functions in each increment step, the whole element formulations are fit in the nonlinear procedure.

Numerical examples show that the proposed elements exhibit excellent performance and possess high precision no matter in linear or geometrically nonlinear problems. It inherits the high-performance and shape-free features of HSDF elements, and show flexibility for the cases with complex geometry. That is to say, even if very coarse or severely distorted meshes are used, the new elements can still work well and stably. It should also be noted that it is the first successful model for HSDF elements for geometrically nonlinear analyses.

The proposed polygonal plate elements possesses advantages from both analytical and discrete methods, and can be easily integrated into the standard framework of finite element programs. An interesting further work is to develop new shape-free polygonal shell element models to solve material nonlinear problems. These works will be reported in near future.

ACKNOWLEDGMENT

The authors would like to thank for the financial supports from the National Natural Science Foundation of China (11872229).

DATA AVAILABILITY STATEMENT

Data openly available in a public repository that issues datasets with DOIs.

ORCID

Cheng-jin Wu https://orcid.org/0000-0002-1210-956X
Song Cen https://orcid.org/0000-0002-8674-4005

REFERENCES

1. Zienkiewicz OC, Taylor RL, Taylor RL, Taylor RL. *The Finite Element Method: Solid Mechanics*. 5th ed. Oxford, UK: Butterworth-Heinemann; 2000.
2. Long YQ, Cen S, Long ZF. *Advanced Finite Element Method in Structural Engineering*. Berlin, Heidelberg; Beijing: Springer-Verlag GmbH, Tsinghua University Press; 2009.
3. Haas C, Friedrich A, Li Z, et al. Regional variability of sea ice properties and thickness in the northwestern weddell sea obtained by in-situ and satellite measurements // PeterLemke. the expedition of the research vessel "Polarstern" to the antarctic in 2006 (ANT-XXIII/7). *Rep Polar Marine Res*. 2009;586:36-74.
4. Nguyen-Xuan H. A polygonal finite element method for plate analysis. *Comput Struct*. 2017;188:45–62.
5. Wachspress EL. A rational basis for function approximation. *IMA J Appl Math*. 1971;8(1):223-252.

6. Dikshit HP, Ojha A. Dimensions of spaces of wachspress type C-1-rational finite-elements. *Comput Math Appl*. 1991;22(3):23-26.
7. Dahmen W, Dikshit HP, Ojha A. On wachspress quadrilateral patches. *Comput Aided Geom Des*. 2000;17(9):879-890.
8. Dikshit HP, Ojha A. On C-1-continuity of wachspress quadrilateral patches. *Comput Aided Geom Des*. 2002;19(3):207-222.
9. Dasgupta G. Interpolants within convex polygons: wachspress' shape functions. *J Aerosp Eng*. 2003;16(1):1-8.
10. Ghosh S, Mukhopadhyay SN. A material based finite-element analysis of heterogeneous media involving Dirichlet tessellations. *Comput Methods Appl Mech Eng*. 1993;104(2):211-247.
11. Ghosh S, Moorthy S. Elastic-plastic analysis of arbitrary heterogeneous materials with the Voronoi-cell finite-element method. *Comput Methods Appl Mech Eng*. 1995;121(1–4):373-409.
12. Zhang J, Katsube N. A polygonal element approach to random heterogeneous media with rigid ellipses or elliptical voids. *Comput Methods Appl Mech Eng*. 1997;148(3–4):225-234.
13. Meyer M, Barr A, Lee H, Desbrun M. Generalized barycentric coordinates on irregular polygons. *J Graph Tools*. 2002;7(1):13-22.
14. Sukumar N, Tabarraei A. Conforming polygonal finite elements. *Int J Numer Methods Eng*. 2004;61(12):2045-2066.
15. Dai KY, Liu GR, Nguyen TT. An *n*-sided polygonal smoothed finite element method (nSFEM) for solid mechanics. *Finite Elem Anal Des*. 2007;43(11–12):847-860.
16. Nguyen-Thoi T, Liu G, Nguyen-Xuan H. An *n*-sided polygonal edge-based smoothed finite element method (nES-FEM) for solid mechanics. *Int J Numer Methods Biomed Eng*. 2011;27(9):1446-1472.
17. Song C, Wolf JP. The scaled boundary finite-element method-alias consistent infinitesimal finite-element cell method - for elastodynamics. *Comput Methods Appl Mech Eng*. 1997;147(3–4):329-355.
18. Peng Y, Zhang L, Pu J, Guo Q. A two-dimensional base force element method using concave polygonal mesh. *Eng Anal Bound Elem*. 2014;42:45–50.
19. Nguyen-Xuan H, Chau KN, Chau KN. Polytopal composite finite elements. *Comput Methods Appl Mech Eng*. 2019;355:405-437.
20. Videla J, Natarajan S, Bordas SPA. A new locking-free polygonal plate element for thin and thick plates based on Reissner-Mindlin plate theory and assumed shear strain fields. *Comput Struct*. 2019;220:32–42.
21. Katili I, Maknun IJ, Katili AM, Bordas SPA, Natarajan S. A unified polygonal locking-free thin/thick smoothed plate element. *Compos Struct*. 2019;219:147–157.
22. Ho-Nguyen-Tan T, Kim HG. Polygonal shell elements with assumed transverse shear and membrane strains. *Comput Methods Appl Mech Eng*. 2019;349:595–627.
23. Aurojyoti P, Raghu P, Rajagopal A, Reddy JN. An *n*-sided polygonal finite element for nonlocal nonlinear analysis of plates and laminates. *Int J Numer Methods Eng*. 2019;120(9):1071-1107.
24. Dong L, Atluri SN. T-Trefftz Voronoi cell finite elements with elastic/rigid inclusions or voids for micromechanical analysis of composite and porous materials. *Comput Model Eng Sci*. 2012;83(2):183-219.
25. Dong L, Atluri SN. SGBEM Voronoi cells (SVCs), with embedded arbitrary-shaped inclusions, voids, and/or cracks, for micromechanical modeling of heterogeneous materials. *Comput Mater Contin*. 2013;33(2):111-154.
26. de Freitas JAT, Moldovan ID, Cismasiu C. Hybrid-Trefftz displacement element for poroelastic media. *Comput Mech*. 2011;48(6):659-673.
27. de Freitas JAT, Tiago C. Hybrid-Trefftz stress elements for plate bending. *Int J Numer Methods Eng*. 2020;121(9):1946-1976.
28. Qin QH. Hybrid-Trefftz finite-element method for Reissner plates on an elastic-foundation. *Comput Methods Appl Mech Eng*. 1995;122(3–4):379-392.
29. Qin QH. Formulation of hybrid Trefftz finite element method for elastoplasticity. *App Math Model*. 2005;29(3):235-252.
30. Sze KY, Liu GH. Hybrid-Trefftz finite element models for plane Helmholtz problems. *Proceedings of Lsame.08: Leuven Symposium on Applied Mechanics in Engineering, Pts 1 and 2*; Louvain, BELGIUM: Katholieke Univ Leuven, Dept Mech Engn; 2008:385-399.
31. Sze KY, Liu GH. Hybrid-Trefftz Finite Elements for Helmholtz Problem. *ISCM II and EPMESC XII, Pts 1 and 2*. NY, USA: Amer Inst Physics. AIP Conference Proceedings;2010:1233:389-394.
32. She Z, Wang KY, Li PC. Hybrid Trefftz polygonal elements for heat conduction problems with inclusions/voids. *Comput Math Appl*. 2019;78(6):1978-1992.
33. Cen S, Wu CJ, Li Z, Shang Y, Li CF. Some advances in high-performance finite element methods. *Eng Comput*. 2019;36(8):2811-2834.
34. Cen S, Fu XR, Zhou MJ. 8- and 12-node plane hybrid stress-function elements immune to severely distorted mesh containing elements with concave shapes. *Comput Methods Appl Mech Eng*. 2011;200(29–32):2321-2336.
35. Cen S, Zhou MJ, Fu XR. A 4-node hybrid stress-function (HS-F) plane element with drilling degrees of freedom less sensitive to severe mesh distortions. *Comput Struct*. 2011;89(5–6):517-528.
36. Cen S, Fu XR, Zhou GH, Zhou MJ, Li CF. Shape-free finite element method: the plane hybrid stress-function (HS-F) element method for anisotropic materials. *Sci China-Phys Mech Astronomy*. 2011;54(4):653-665.
37. Zhou MJ, Cen S, Bao Y, Li CF. A quasi-static crack propagation simulation based on shape-free hybrid stress-function finite elements with simple remeshing. *Comput Methods Appl Mech Eng*. 2014;275:159–188.
38. Cen S, Bao Y, Li CF. Quasi-static crack propagation modeling using shape-free hybrid stress-function elements with drilling degrees of freedom. *Int J Comput Methods*. 2016;13(3):no.1650014
39. Zhou PL, Cen S. A novel shape-free plane quadratic polygonal hybrid stress-function element. *Math Probl Eng*. 2015;2015:no. 491325
40. Cen S, Shang Y, Li CF, Li HG. Hybrid displacement function element method: a simple hybrid-Trefftz stress element method for analysis of Mindlin-Reissner plate. *Int J Numer Methods Eng*. 2014;98(3):203-234.
41. Shang Y, Cen S, Li CF, Huang JB. An effective hybrid displacement function element method for solving the edge effect of Mindlin-Reissner plate. *Int J Numer Methods Eng*. 2015;102(8):1449-1487.

42. Bao Y, Cen S, Li CF. Distortion-resistant and locking-free eight-node elements effectively capturing the edge effects of Mindlin-Reissner plates. *Eng Comput*. 2017;34(2):548-586.
43. Huang JB, Cen S, Shang Y, Li CF. A new triangular hybrid displacement function element for static and free vibration analyses of Mindlin-Reissner plate. *Latin Am J Solids Struct*. 2017;14(5):765-804.
44. Shang Y, Cen S, Li CF. A 4-node quadrilateral flat shell element formulated by the shape-free HDF plate and HSF membrane elements. *Eng Comput*. 2016;33(3):713-741.
45. Wu CJ, Cen S, Shang Y. Shape-free polygonal hybrid displacement-function element method for analyses of Mindlin–Reissner plates. *Eng Comput*. 2020;1-24. https://doi.org/10.1007/s00366-019-00922-x.
46. Pian THH. Derivation of element stiffness matrices by assumed stress distributions. *AIAA J*. 1964;2(7):1333-1336.
47. Wempner G. Finite elements, finite rotations and small strains of flexible shells. *Int J Solids Struct*. 1969;5(2):117-153.
48. Belytschko T, Schwer L, Klein MJ. Large displacement, transient analysis of space frames. *Int J Numer Methods Eng*. 1977;11(1):65-84.
49. Rankin CC, Brogan FA. An element independent Corotational procedure for the treatment of large rotations. *J Press Vessel Technol Trans Asme*. 1986;108(2):165-174.
50. Rankin CC, Nouromid B. The use of projectors to improve finite-element performance. *Comput Struct*. 1988;30(1–2):257-267.
51. Nouromid B, Rankin CC. Finite rotation analysis and consistent linearization using projectors. *Comput Methods Appl Mech Eng*. 1991;93(3):353-384.
52. Crisfield MA, Moita GF. A unified co-rotational framework for solids, shells and beams. *Int J Solids Struct*. 1996;33(20–22):2969-2992.
53. Felippa CA, Haugen B. A unified formulation of small-strain corotational finite elements: I. theory. *Comput Methods Appl Mech Eng*. 2005;194(21–24):2285-2335.
54. Pacoste C. Co-rotational flat facet triangular elements for shell instability analyses. *Comput Methods Appl Mech Eng*. 1998;156(1–4):75-110.
55. Battini JM. A modified corotational framework for triangular shell elements. *Comput Methods Appl Mech Eng*. 2007;196(13–16):1905-1914.
56. Levy R, Gal E. Geometrically nonlinear three-noded flat triangular shell elements. *Comput Struct*. 2001;79(26–28):2349-2355.
57. Zhou Y, Li YQ, Shen ZY, Zhang YY. Corotational formulation for geometric nonlinear analysis of Shell structures by ANDES elements. *Int J Struct Stab Dyn*. 2016;16(3):no.1450103.
58. Yang JS, Xia PQ. Finite element corotational formulation for geometric nonlinear analysis of thin shells with large rotation and small strain. *Sci China-Technol Sci*. 2012;55(11):3142-3152.
59. Li ZX, Liu YF, Izzuddin BA, Vu-Quoc L. A stabilized co-rotational curved quadrilateral composite shell element. *Int J Numer Methods Eng*. 2011;86(8):975-999.
60. Mostafa M, Sivaselvan MV. On best-fit corotated frames for 3D continuum finite elements. *Int J Numer Methods Eng*. 2014;98(2):105-130.
61. Hu H. *Variational Principles of Theory of Elasticity with Applications*. Boca Raton, FL: CRC Press; 1984.
62. Allman DJ. A compatible triangular element including vertex rotations for plane elasticity analysis. *Comput Struct*. 1984;19(1–2):1-8.
63. Taylor RL. *Finite Element Analysis of Linear Shell Problems*. New York, NY: Academic Press; 1987.
64. Abaqus. *Documentation*. Vol 2016. Providence, RI: Dassault Systèmes Simulia Corp; 2017.
65. Battini JM, Pacoste C. On the choice of local element frame for corotational triangular shell elements. *Commun Numer Methods Eng*. 2004;20(10):819-825.
66. Rezaiee-Pajand M, Yaghoobi M. An efficient flat shell element. *Meccanica*. 2018;53(4–5):1015-1035.
67. Choi CK, Lee PS, Park YM. Defect-free 4-node flat shell element: NMS-4F element. *Struct Eng Mech*. 1999;8(2):207-231.
68. Long YQ, Xu Y. Generalized conforming triangular membrane element with vertex rigid rotational freedoms. *Finite Elements Anal Des*. 1994;17(4):259-271.
69. Belytschko T, Leviathan I. Physical stabilization of the 4-node Shell element with one-point quadrature. *Comput Methods Appl Mech Eng*. 1994;113(3–4):321-350.
70. Sze KY, Liu XH, Lo SH. Popular benchmark problems for geometric nonlinear analysis of shells. *Finite Elem Anal Des*. 2004;40(11):1551-1569.
71. de Sousa RJA, Cardoso RPR, Valente RAF, Yoon JW, Gracio JJ, Jorge RMN. A new one-point quadrature enhanced assumed strain (EAS) solid-shell element with multiple integration points along thickness-Part II: nonlinear applications. *Int J Numer Methods Eng*. 2006;67(2):160-188.
72. Cardoso RPR, Yoon JW, Mahardika M, Choudhry S, de Sousa RJA, Valente RAF. Enhanced assumed strain (EAS) and assumed natural strain (ANS) methods for one-point quadrature solid-shell elements. *Int J Numer Methods Eng*. 2008;75(2):156-187.
73. De Borst R, Crisfield MA, Remmers JJ, Verhoosel CV. *Nonlinear Finite Element Analysis of Solids and Structures*. Hoboken, NJ: John Wiley & Sons; 2012.

How to cite this article: Wu C, Cen S, Ma R, Li C. Shape-free arbitrary polygonal hybrid stress/displacement-function flat shell element for linear and geometrically nonlinear analyses. *Int J Numer Methods Eng*. 2021;1–47. https://doi.org/10.1002/nme.6699

APPENDIX A. THE TRANSFORMATION RELATIONSHIPS BETWEEN ROTATION VECTOR θ AND MATRIX R

The transformation relationships between ${}^{t+\Delta t}\boldsymbol{\theta}_a$ and ${}^{t+\Delta t}\mathbf{R}_a$, ${}^{t+\Delta t}\overline{\boldsymbol{\theta}}_{\mathrm{d}a}$ and ${}^{t+\Delta t}\overline{\mathbf{R}}_{\mathrm{d}a}$, are needed in Section 4.1. The relationships are expressed as follow.

Let $\boldsymbol{\theta}$ represents ${}^{t+\Delta t}\boldsymbol{\theta}_a$ or ${}^{t+\Delta t}\overline{\boldsymbol{\theta}}_{\mathrm{d}a}$ with $\boldsymbol{\theta}=\theta\mathbf{n}=\{\theta_1,\theta_2,\theta_3\}^{\mathrm{T}}$, $\mathbf{n}=\{n_1,n_2,n_3\}^{\mathrm{T}}$, and $\mathbf{R}$ for ${}^{t+\Delta t}\mathbf{R}_a$ or ${}^{t+\Delta t}\overline{\mathbf{R}}_{\mathrm{d}a}$, then,

$$\mathbf{R}=\mathbf{I}+\frac{\sin\theta}{\theta}\boldsymbol{\Theta}+\frac{2\sin^2\frac{1}{2}\theta}{\theta^2}\boldsymbol{\Theta}^2=\mathbf{I}+\sin\theta\mathbf{N}+(1-\cos\theta)\mathbf{N}^2, \tag{A1}$$

in which

$$\boldsymbol{\Theta}=\mathrm{spin}(\boldsymbol{\theta})=\begin{bmatrix}0&-\theta_3&\theta_2\\ \theta_3&0&-\theta_1\\ -\theta_2&\theta_1&0\end{bmatrix},\mathbf{N}=\mathrm{spin}(\mathbf{n})=\begin{bmatrix}0&-n_3&n_2\\ n_3&0&-n_1\\ -n_2&n_1&0\end{bmatrix}, \tag{A2}$$

and $\mathbf{I}$ is unit tensor, obviously, $\mathbf{R}=\mathbf{I}$ if $\theta=0$. And

$$\cos\theta=\frac{1}{2}(\mathrm{trace}(\mathbf{R})-1),\mathbf{N}=\frac{\mathbf{R}-\mathbf{R}^{\mathrm{T}}}{2\sin\theta},\mathbf{n}=\begin{bmatrix}n_1\\ n_2\\ n_3\end{bmatrix}=\mathrm{axial}(\mathbf{N}), \tag{A3}$$

in which trace($\mathbf{R}$) denotes the trace of $\mathbf{R}$, specially, when $\mathbf{R}=\mathbf{I}$, $\boldsymbol{\theta}=\mathbf{n}=\mathbf{0}$.

APPENDIX B. THE EXPRESSIONS OF EQUATION CHAPTER 1 SECTION 1 $\overline{\mathbf{H}}_a$, $\overline{\mathbf{L}}_a$, $\overline{\mathbf{P}}_u$, AND $\overline{\mathbf{S}}$

For Node A with the node number a,

$$\overline{\mathbf{H}}_a=\overline{\mathbf{H}}(\overline{\boldsymbol{\theta}}_{\mathrm{d}a})=\mathbf{I}_3-\frac{1}{2}\mathrm{spin}(\overline{\boldsymbol{\theta}}_{\mathrm{d}a})+\eta\mathrm{spin}(\overline{\boldsymbol{\theta}}_{\mathrm{d}a})^2, \tag{B1}$$

with

$$\begin{aligned}\eta&=\frac{1-\frac{1}{2}\overline{\theta}_{\mathrm{d}i}\cot\left(\frac{1}{2}\overline{\theta}_{\mathrm{d}i}\right)}{\frac{1}{2}\overline{\theta}_{\mathrm{d}i}^2}\\ &=\frac{1}{12}+\frac{1}{720}\overline{\theta}_{\mathrm{d}i}^2+\frac{1}{30240}\overline{\theta}_{\mathrm{d}i}^4+\frac{1}{1209600}\overline{\theta}_{\mathrm{d}i}^6+\cdots.\end{aligned} \tag{B2}$$

Generally, η is computed by equation in the first line, but if $\overline{\theta}_{\mathrm{d}a}$ turns to be very small ($\overline{\theta}_{\mathrm{d}a}\le 3°$), the second line should be adopted to avoid numerical unstable.

$$\begin{aligned}\overline{\mathbf{L}}_a=\{&\eta[(\overline{\boldsymbol{\theta}}_{\mathrm{d}a}^{\mathrm{T}}\overline{\mathbf{m}}_a)\mathbf{I}_3+\overline{\boldsymbol{\theta}}_{\mathrm{d}a}\overline{\mathbf{m}}_a^{\mathrm{T}}-2\overline{\mathbf{m}}_a\overline{\boldsymbol{\theta}}_{\mathrm{d}a}^{\mathrm{T}}]\\ &+\mu\mathrm{spin}(\overline{\boldsymbol{\theta}}_{\mathrm{d}a})^2\overline{\mathbf{m}}_a\overline{\boldsymbol{\theta}}_{\mathrm{d}a}^{\mathrm{T}}-\frac{1}{2}\mathrm{spin}(\overline{\mathbf{m}}_a)\Big\}\overline{\mathbf{H}}(\overline{\boldsymbol{\theta}}_{\mathrm{d}a}),\end{aligned} \tag{B3}$$

in which

$$\mu=\frac{\overline{\theta}_{\mathrm{d}a}^2+4\cos\overline{\theta}_{\mathrm{d}a}-\overline{\theta}_{\mathrm{d}a}\sin\overline{\theta}_{\mathrm{d}a}-4}{4\overline{\theta}_{\mathrm{d}a}^4\sin\left(\frac{1}{2}\overline{\theta}_{\mathrm{d}a}\right)}$$

$$= \frac{1}{360} + \frac{1}{7560}\overline{\theta}_{da}^{2} + \frac{1}{201600}\overline{\theta}_{da}^{4} + \frac{1}{5987520}\overline{\theta}_{da}^{6} + \cdots. \tag{B4}$$

Generally, μ is computed by equation in the first line, but if $\overline{\theta}_{da}$ turns to be very small ($\overline{\theta}_{da} \leq 3°$), the second line should be adopted to avoid numerical unstable.

$$\overline{\mathbf{P}}_u = \begin{bmatrix} \overline{\mathbf{P}}_{u11} & \overline{\mathbf{P}}_{u12} & \overline{\mathbf{P}}_{u13} \\ \overline{\mathbf{P}}_{u21} & \overline{\mathbf{P}}_{u22} & \overline{\mathbf{P}}_{u23} \\ \overline{\mathbf{P}}_{u31} & \overline{\mathbf{P}}_{u32} & \overline{\mathbf{P}}_{u33} \end{bmatrix}, \tag{B5}$$

with $\overline{\mathbf{P}}_{uij}(i, j = 1, 2, 3)$ is a submatrix of $\overline{\mathbf{P}}_u$, and

$$\overline{\mathbf{P}}_{uij} = \begin{bmatrix} \mathbf{U}_{ij} & \mathbf{0}_3 \\ \mathbf{0}_3 & \mathbf{I}_3 \end{bmatrix}, \tag{B6}$$

$$\mathbf{U}_{ij} = \left(\delta_{ij} - \frac{1}{n}\right)\mathbf{I}_3, \tag{B7}$$

where $\delta_{ij}$is the Kronecker delta, n is the edge number of the element.

$$\overline{\mathbf{S}} = \begin{bmatrix} -\overline{\mathbf{S}}_1^{\mathrm{T}} & \mathbf{I}_3 & -\overline{\mathbf{S}}_2^{\mathrm{T}} & \mathbf{I}_3 & \cdots & \cdots & -\overline{\mathbf{S}}_n^{\mathrm{T}} & \mathbf{I}_3 \end{bmatrix}^{\mathrm{T}}, \tag{B8}$$

$$\overline{\mathbf{S}}_a = \mathrm{spin}\left({}^{t+\Delta t}\overline{\mathbf{x}}_a\right) = \begin{bmatrix} 0 & -{}^{t+\Delta t}\overline{z}_a & {}^{t+\Delta t}\overline{y}_a \\ {}^{t+\Delta t}\overline{z}_a & 0 & -{}^{t+\Delta t}\overline{x}_a \\ -{}^{t+\Delta t}\overline{y}_a & {}^{t+\Delta t}\overline{x}_a & 0 \end{bmatrix}, (a = 1, 2, \cdots, n), \tag{B9}$$

with $\overline{\mathbf{x}}_a = \begin{bmatrix} \overline{x}_a & \overline{y}_a & \overline{z}_a \end{bmatrix}^{\mathrm{T}}$ denotes the local coordinate vector of node A.